The Dissertation Committee for Ingmar Michael Schoegl
certifies that this is the approved version of the following dissertation:

Superadiabatic Combustion in Counter-Flow Heat Exchangers

Committee:

Janet L Ellzey, Supervisor

Ofodike A Ezekoye

John R Howell

Philip S Schmidt

Oscar Gonzalez

Superadiabatic Combustion in Counter-Flow Heat Exchangers

by

Ingmar Michael Schoegl, Dipl.-Ing.

Dissertation

Presented to the Faculty of the Graduate School of

The University of Texas at Austin

in Partial Fulfillment

of the Requirements

for the Degree of

Doctor of Philosophy

The University of Texas at Austin

May 2009

To my family.

Acknowledgments

There are many people who have been tremendously helpful and inspiring to me throughout the years. First and foremost, however, I want to thank my wife, Emily Blosser, for continuing support and encouragement. Also, I want to acknowledge my children – Conrad, Sebastian and Leo – who have been an inspiration and, while sometimes not being exactly helpful regarding the progress of my work, still greatly contributed by keeping my life in balance. I am deeply indebted to my parents, Kurt Schögl and Eva Neuwirth, as well as my entire family, who instilled me with a deep interest in discovery and learning.

This work would certainly not have been possible without the skillful guidance of my dissertation supervisor, Dr. Janet L. Ellzey, who has been an invaluable mentor. Throughout the pursuit of my PhD degree, she has granted me the trust and freedom to investigate new ideas, thus teaching me lessons that are invaluable for conducting successful research. I also want to thank my dissertation committee members – Dr. Ofodike A. Ezekoye, Dr. Philip R. Schmidt, Dr. John S. Howell and Dr. Oscar Gonzalez – for many valuable discussions and insights. Furthermore, Dr. Kovar has given me the opportunity to extend my knowledge beyond combustion science by engaging me in work on ceramics processing.

I want to thank all of my former and present colleagues in the laboratory for company and friendship throughout my time at UT; Ravi Dhamrat, Brian Vogel, Dan Vennetti, Matt Fay, Simone Marras, Mike Dixon, Brad Hull, Doyle Motes, Dan Leahey, Ryan Newcomb, Colin Smith and Jim Mikulak all have made life in the laboratory interesting and enjoyable by engaging me in countless discussions.

During my time in Austin, I met a great number of people whose company I truly enjoyed and many of whom I now count among my best friends. While I am unable to name them all, I want to especially thank Mirko Gamba, with whom I have spent endless coffee breaks and evenings discussing research and many other aspects of life. Also, I want to thank Georg Stadler, who is one of the few people with whom I was able to share my thoughts on the unique perspective of Austrians living in the United States.

Last, but no least, I want to acknowledge the many sources of funding that have made this endeavor possible: the Department of Mechanical Engineering for giving me the opportunity to work as a Teaching Assistant and Assistant Instructor; the Cockrell School of Engineering, John and Mary Booker as well as C. W. W. Cook for their invaluable financial support; and The University of Texas at Austin for awarding me the Continuing Fellowship that has allowed me to fully focus on my research during the final stage of my PhD work. Also, this material is based on work supported by the National Science Foundation under Grant No. 0522640.

Ingmar Michael Schoegl

The University of Texas at Austin
May 2009

Superadiabatic Combustion in Counter-Flow Heat Exchangers

Publication No. ____________________

Ingmar Michael Schoegl, Ph.D.
The University of Texas at Austin, 2009

Supervisor: Janet L Ellzey

Syngas, a combustible gaseous mixture of hydrogen, carbon monoxide, and other species, is a promising fuel for efficient energy conversion technologies. Syngas is produced by breaking down a primary fuel into a hydrogen-rich mixture in a process called fuel reforming. The motivation for the utilization of syngas rather than the primary fuel is that syngas can be used in energy conversion technologies that offer higher conversion efficiencies, e.g. gas turbines and fuel cells. One approach for syngas production is partial oxidation, which is an oxygen starved combustion process that does not require a catalyst. Efficient conversion to syngas occurs at high levels of oxygen depletion, resulting in mixtures that are not flammable in conventional combustion applications. In non-catalytic partial oxidation, internal heat recirculation is used to increase the local reaction temperatures by transferring heat from the product stream to pre-heat the fuel/air mixture before reactions occur, thus increasing reaction rates and allowing for combustion outside the conventional flammability limits. As peak temperatures lie above the adiabatic equilibrium temperature predicted by thermodynamic calculations, the combustion regime used for non-catalytic fuel reforming is referred to as ’superadiabatic’.

Counter-flow heat exchange is an effective way to to transfer heat between adjacent channels and is used for a novel, heat-recirculating fuel reformer design. An analytical study predicts that combustion zone locations inside adjacent flow channels adjust to operating conditions, thus stabilizing the process for independent variations of flow velocities and mixture compositions. In experiments, a reactor prototype with four channels with alternating flow directions is developed and investigated. Tests with methane/air and propane/air mixtures validate the operating principle, and measurements of the resulting syngas compositions verify the feasibility of the concept for practical fuel-reformer applications. Results from a two-dimensional numerical study with detailed reaction chemistry are consistent with experimental observations. Details of the reaction zone reveal that reactions are initiated in the vicinity of the channel walls, resulting in “tulip”-shaped reaction layers. Overall, results confirm the viability of the non-catalytic reactor design for fuel reforming applications.

Contents

List of Tables

List of Figures

Nomenclature

Symbols (dimensional)

α'	Thermal diffusivity [m^2/s]
$\mathcal{D}'$	Species diffusivity [m^2/s]
ρ'	Density [kg/m^3]
σ'_B	*Stefan-Boltzmann* constant $\equiv 5.670 \times 10^{-8}$ [J/K^{4}m^{2}s]
a'	Channel width [m]
b'	Wall thickness [m]
c'	Specific heat capacity [J/kg K]
E'_a	Activation energy [J/mol]
h'	Heat transfer coefficient [W/m^2 K]
k'	Conductivity [W/m K]
L'	Channel length [m]
Q'	Heat of reaction [J/kg]
R'	Universal gas constant $\equiv 8.3144$ [J/mol/K]
T'	Temperature [K]

u'	Flow velocity [m/s]
w'	Chemical reaction rate [kg/m^3 s]
x'	Axial position [m]
y'	Concentration [mol/mol]
Z'	Reaction frequency factor
$\dot{N}$	Molar flow rate.
$\dot{V}$	Volumetric flow rate.
A	Reactor cross-section area.
LHV	Lower heating value.

Symbols (non-dimensional)

β	Mod. *Zeldovich* number $\equiv \mathrm{Ze}/\gamma$
γ	Factor $\equiv \Delta T'_{\mathrm{ad}}/T'_{\mathrm{ref}}$
Λ	Eigenvalue
ϕ'	Equivalence ratio [$-$]
ψ	Heat flux $\equiv dT/dx$
σ	Radiation factor $\equiv \varepsilon\sigma'_B \, {T'_{\mathrm{ref}}}^3 \, L'/2k'_w$
ε	Emissivity [$-$]
ϑ	“Adiabaticity” $\equiv (T - T_0)/\gamma$
a	Channel width $\equiv 2a'/L'$
b	Wall thickness $\equiv 2b'/L'$

T	Temperature $\equiv T'/T'_{\mathrm{ref}}$
u	Velocity ratio $\equiv u'/u'_{\mathrm{ref}}$
w	Reaction rate
x	Axial position $\equiv 2x'/L'$
y	Concentration $\equiv y'/y'_0$
Le	*Lewis* number $\equiv \mathcal{D}'_g/\alpha'_g$
Nu	*Nusselt* number $\equiv h'a'/k'_g$
Pe	*Peclet* number $\equiv a'u'_{\mathrm{ref}}/\alpha'_g$
Ze	*Zeldovich* number $\equiv E'_a\Delta T'_{\mathrm{ad}}/R'\,{T'_{\mathrm{ad}}}^2$
k	Relative conductivity $\equiv k'_g/k'_w$
χ	Heat loss factor $\equiv \mathrm{Nu}_\infty/2\mathrm{Nu}$
ϵ	Geometry factor $\equiv a/\mathrm{Pe}$
κ	Conductivity factor $\equiv b/2ak$
μ	Heat transfer factor $\equiv \mathrm{Nu}/\mathrm{Pe}^2$
η	Efficiency.
$\varkappa$	Exponent; or number of product moles per mole of fuel.
m	Number of H_2 moles per mole of chemical species.
n	Number of C moles per mole of chemical species.
o	Number of O_2 moles per mole of chemical species.
r	Number of moles of air to react a mole of fuel at $\phi = 1$.

Subscripts

$_0$	Initial
$_1$	Channel 1
$_2$	Channel 2
$_{\mathrm{ad}}$	Adiabatic
$_{\mathrm{cal}}$	Calibrated
$_\infty$	Environment
$_{\mathrm{ref}}$	Reference
$_c$	Combustion location
$_e$	Channel end-point
$_g$	Gas
$_u$	Unburned
$_w$	Wall
$_{\mathrm{fu}}$	Fuel
$_{\mathrm{ox}}$	Oxidizer
$_{\mathrm{prod}}$	Products
$_{\mathrm{reac}}$	Reactants
$_{Energy}$	Energy

Superscripts

$'$	Dimensional variable

$^{+}$	Right side
$^{-}$	Left side
$^{\pm}$	Middle

Chapter 1

Introduction

Environmental concerns as well as the necessity for the efficient usage of available energy resources have spurred research on a wide range of alternative energy concepts. Among the many technologies currently being investigated, heat recirculating combustors have shown potential benefits due to increased firing rates and decreased pollutant emissions, which are accomplished through an increase of the combustion temperatures. One remarkable advantage of heat recirculating combustors over conventional burners is their ability to operate beyond the conventional flammability limits under both extremely fuel-lean (ultra-lean) and fuel-rich (ultra-rich) conditions (Fig. 1.1).

Heat recirculating combustors have various important applications for combustion of ultra-lean and ultra-rich mixtures, which lie beyond the conventional lean and rich flammability limits, respectively. In the ultra-lean regime, heat recirculation establishes

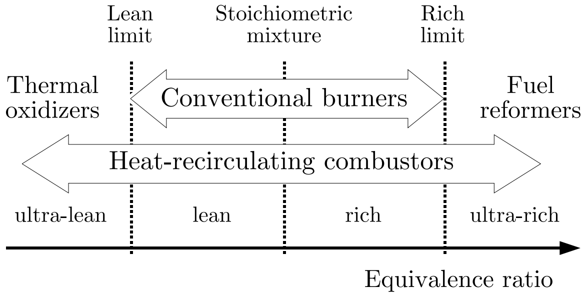

Figure 1.1: Operating regimes of conventional burners and heat-recirculating combustors.

high temperatures which facilitate the thermal oxidation of sparse amounts of fuel in extremely lean mixtures (Lloyd and Weinberg, 1974; Henneke and Ellzey, 1999). Thus it is possible to break down hazardous volatile organic compounds (vocs) into less polluting species. At the other extreme, ultra-rich fuel/air mixtures can be converted into hydrogen-rich syngas by partial oxidation of a hydrocarbon fuel (Kennedy et al., 2000; Dhamrat and Ellzey, 2006). The syngas produced by this process consists of hydrogen (H_2), carbon monoxide (CO), carbon dioxide (CO_2) and other species, whereas the process of converting a hydrocarbon fuel into hydrogen-rich gas is referred to as fuel reforming. In recent years, an increased interest in fuel cells has led to research on technologies that produce hydrogen-rich syngas. Fuel cells convert a fuel directly into electricity in an electrochemical process. This direct pathway is especially attractive as it is not limited by the thermodynamic limits dictated by the Carnot cycle and thus offers substantial efficiency gains (Carrette et al., 2001). Some of the unresolved issues of fuel cell technologies, however, arise in the context of transportation and storage of suitable fuel sources. Most fuel cell types operate with hydrogen as fuel, which has a high gravimetric energy density (>30kWh/kg). Direct storage at atmospheric conditions, however, is nontrivial due to the low density of hydrogen, resulting in a volumetric energy density below 3Wh/L. Thus, direct storage of hydrogen is challenging as it requires either large pressures, low temperatures or heavy metal-hydride reservoirs (Dunn-Rankin et al., 2005). In an alternative approach, a hydrogen-rich syngas feed stream can be generated by reforming a liquid hydrocarbon in a decentralized and “on demand” basis. Here, a hydrocarbon fuel acts as an easily storable hydrogen source, where liquid fuels with typical volumetric energy densities beyond 8 kWh/l are suitable candidates (Fernandez-Pello, 2002; Dunn-Rankin et al., 2005).

Depending on the fuel cell type, syngas can be either used directly in high-temperature solid oxide fuel cells (SOFC) (Kee et al., 2005) or may be further processed by a combination of water-gas shift reactions and membrane separation (Wheeler et al., 2004; Lin et al., 2006; Iyoha et al., 2007) to obtain pure hydrogen fuel for proton-exchange membrane (PEM) fuel cells. Conventional reforming techniques use catalysts to promote the conversion of hydrocarbons to a syngas (Naidja et al., 2003), where typical techniques involve steam reforming or catalytic partial oxidation (Krebs, 2003). Catalytic processes, however, require tightly controlled operating conditions and fuel quality to prevent degradation due to excessive temperatures and catalyst poisoning by sulfur compounds (Moon et al., 2004).

1.1 Non-Catalytic Fuel Reforming

Non-catalytic fuel reformers do not rely on catalytically active surfaces and thus are not susceptible to poisoning and temperature-related deterioration. Instead, non-catalytic fuel reforming is performed in heat-recirculating combustors, where a fuel-rich hydrocarbon/air mixture is converted to syngas in a gas phase reaction. As non-catalytic fuel reformers are able to operate over a wide range of mixture qualities and are insensitive to elevated temperatures, they represent an attractive alternative to conventional catalytic reforming techniques.

Thermodynamic equlibrium calculations are a valuable tool to obtain some insights into the potential of non-catalytic reforming. Equilibrium calculations use an idealized thermodynamic state with maximum entropy to predict the composition of the reacted mixture. This state, however, requires infinite residence time for all chemical reactions to complete, which restricts equilibrium calculations to qualitative predictions. Nevertheless, equilibrium calculations yield information that is useful for the assessment of a combustion process. Figure 1.2 shows thermodynamic equilibrium predictions for combustion products of methane (CH_4) fuel over a wide range of equivalence ratios, obtained from the numerical chemistry code Cantera (Goodwin, 2003). Results at stoichiometric conditions ($\phi = 1.0$) illustrate that the major constituents of the product gas are N_2, H_2O and CO_2. Combustion at richer conditions produces substantial amounts

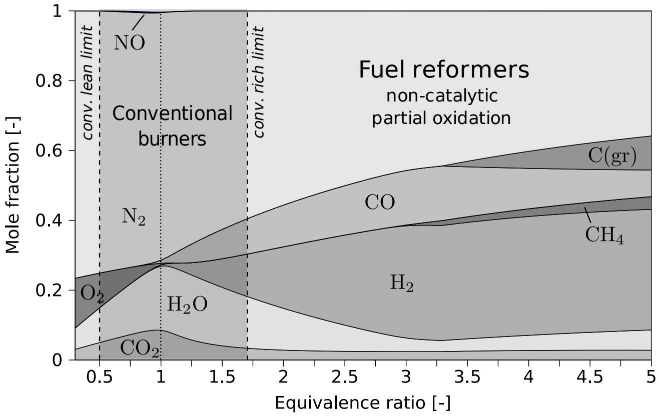

Figure 1.2: Equilibrium predictions for the composition of syngas obtained from CH_4 combustion (T_0=300K, p=1atm).

of H_2 and CO, which increase significantly up to $\phi \approx 3.0$. At equivalence ratios beyond 3.0, thermodynamic equilibrium calculations predict unreacted CH_4 as well as carbon, indicating that at extremely rich conditions unwanted byproducts are generated.

The efficiency of the fuel reforming process, in terms of hydrogen production, can be assessed by comparing the rate of H_2 moles generated to the number of moles of H_2 bound in the inlet fuel. Thus, the molar efficiency for hydrogen production is given by

$$\eta_{\mathrm{H}_2} = \frac{\dot{N}_{\mathrm{H}_2,prod}}{\dot{N}_{\mathrm{H}_2,max}} = \frac{\dot{N}_{\mathrm{H}_2,prod}}{2\dot{N}_{\mathrm{CH}_4,reac}} \tag{1.1}$$

where the $\dot{N}_i$ denote molar fluxes in product and reactant streams. Figure 1.3 illustrates the theoretical molar hydrogen conversion efficiency as predicted by equilibrium calculations as well as a similarly defined conversion efficiency of CH_4 to CO. The highest molar conversion efficiencies are predicted for an equivalence ratio $\phi \approx 3$, with $\eta_{\mathrm{H}_2} \approx 88\%$ and $\eta_{\mathrm{CO}} \approx 86\%$. In addition, Fig. 1.3 shows the adiabatic equilibrium temperature, T_{ad}, which is the theoretical maximum temperature for combustion processes without heat recirculation. Results show that T_{ad} is a strong function of the equivalence ratio. For rich mixtures ($\phi > 1$), temperatures decrease rapidly as ϕ increases, dropping below 1000K for $\phi > 3.1$.

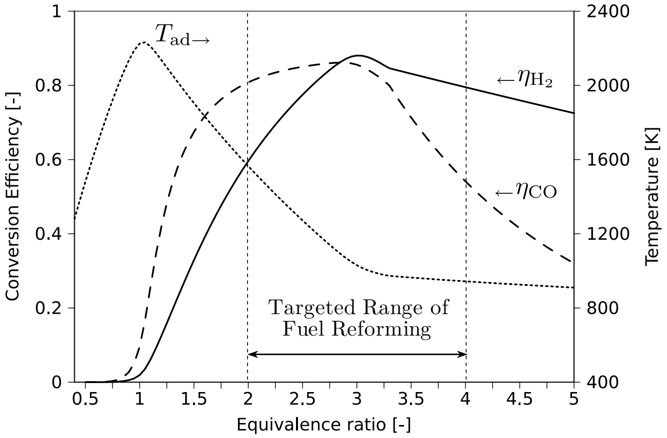

Figure 1.3: Theoretical molar efficiencies for conversion of CH_4 to H_2/CO and adiabatic equilibrium temperatures.

Considering fundamental characteristics of methane combustion, equilibrium calculations predict the most efficient regime for fuel reforming beyond the conventional rich flammability limit at $\phi = 1.7$ (Glassman, 1996). Without heat recirculation, the energy content of the reactants and external heat losses limit the temperature of the combustion zone. Beyond the conventional flammability limits, reaction rates are sluggish and the rate of heat released by chemical reactions is not sufficient to overcome external heat losses, resulting in flame quenching (Spalding, 1957; Buckmaster, 1976). Due to the limitation to operate within the conventional flammability limits, conventional burners are not suited for fuel reforming.

Heat recirculating reactors recirculate heat from the hot combustion products to preheat the unreacted air/fuel mixture, which raises the peak temperatures above the adiabatic limit, resulting in *superadiabatic* temperatures. The increased combustion temperatures enhance the reaction rates, and thus it is possible to overcome external heat losses and enable a self-sustained combustion process beyond the conventional flammability limits (Lloyd and Weinberg, 1975).

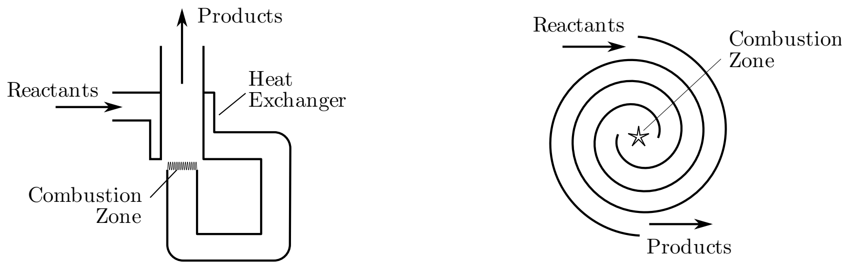

(a) Heat exchanger. **(b)** Swiss-roll geometry.

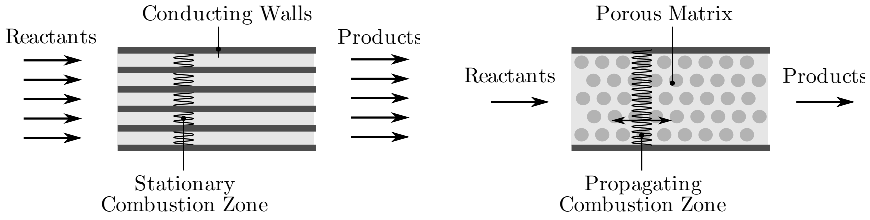

(c) Conducting tubes. **(d)** Propagating combustion wave.

Figure 1.4: Different heat transfer concepts used in heat recirculating combustors.

1.2 Review of Superadiabatic Combustion

Ideas fundamental to superadiabatic combustion were first introduced by Egerton, et al. (1963) and Weinberg (1971). Local combustion temperatures are increased by transferring enthalpy from the hot combustion products to preheat the unburned air/fuel mixture, which has led to the term *excess enthalpy* combustion. While the overall system is governed by first law principles, local peak temperatures can exceed the adiabatic flame temperature by a significant amount (Aldushin, 1993; Babkin, 1993), resulting in combustion at *superadiabatic* temperatures.

1.2.1 Heat Recirculation Mechanisms

In a conceptual discussion, Weinberg (1971) proposed various combustor designs using non-mixing single-stage and/or counter-flow heat exchangers to accomplish heat transfer from combustion products to the reactant stream (e.g. Fig. 1.4a). The initial experimental verification of the excess enthalpy concept was obtained for a double-spiral

(*Swiss-Roll*) combustor design (Fig. 1.4b), where heat is transferred in counter-flow heat exchange between inflowing reactants and outflowing products (Lloyd and Weinberg, 1974; Hardesty and Weinberg, 1974). A subsequent review of different heat recirculating combustor types compared experimental data with predictions of a global analytical model (Jones et al., 1978). Results showed that, compared to conventional designs, heat-recirculating combustors bring about a substantial increase of the burning rate as well as an extension of the flammability limits.

Takeno and Sato (1979) as well as Kotani and Takeno (1982) demonstrated that combustion with superadiabatic peak temperatures can also be realized by inserting a porous solid into the flame (Fig. 1.4c). Stationary porous burners are characterized by a reaction zone that is stabilized within a porous matrix. In order to preheat the incoming fuel/air mixture, heat from the downstream regions is transferred by conduction and radiation to upstream regions within the porous solid. This heat recirculation results in increased firing rates (Howell et al., 1996) and, by consequence, extended flammability limits. Experimental results as well as numerical simulations of combustion in porous media show that material properties and pore geometry have a significant impact on the combustion process (Min and Shin, 1991; Howell et al., 1996; Fu et al., 1998; Viskanta and Gore, 2000; Bubnovich et al., 2007). These differences can be utilized to enhance the stability of the combustion zone in a two-layer design, where the flame is held close to the interface between a small-pore upstream section and a large pore downstream section (Hsu et al., 1993). A variation of stationary porous burners uses a widening porous channel with uniform porosity, where the reaction zone is anchored at the location where the flow velocity matches the speed of the local flame speed (Trimis et al., 1997).

In an alternative design, superadiabatic temperatures are achieved in a transient combustion regime (Fig. 1.4d), where a combustible air/fuel mixture streams through an inert packed bed or porous media and reacts in a *filtration wave* (Laevskii et al., 1984; Zhdanok et al., 1995). A closely related concept uses an oxidizer streaming through a porous bed of solid fuel (Wicke and Vortmeyer, 1959). In the case of reaction fronts propagating in the same direction as the gas feed stream, the front moves into a region which was previously preheated by the combustion products. Thus, combustion enthalpy is added at a higher temperature level, and local peak temperatures can exceed the adiabatic equilibrium temperature. Another variant of a superadiabatic reactor design was investigated by Weinberg, et al. (1988), where heat recirculation is established in a spouted bed reactor by recirculating particles to transfer heat from the hot exhaust to the cold reactants. A more detailed review of various burner concepts using superadiabatic combustion can be found in Babkin, et al. (2002).

Historically, various pathways to accomplish superadiabatic combustion have evolved. In terms of the underlying physics, however, all processes rely on a common idea in which heat is transferred from (hot) combustion products to (cold) incoming gas feed stream. Three different mechanisms, sometimes occurring in combination, can be distinguished: (1) heat recirculation by conductive or radiative heat transfer from regions downstream of the combustion zone to regions upstream of the combustion zone; (2) regenerative preheating of the reactants by heat transfer from an inert solid previously exposed to hot combustion products; and (3) heat recirculation by heat exchange across a wall dividing combustion products from cold reactants.

1.2.2 Non-Catalytic Fuel Reforming Techniques

The last decade has seen a significant amount of research on non-catalytic fuel reforming. Research efforts have largely focused on *filtration* combustion (Drayton et al., 1998; Dhamrat and Ellzey, 2006), which is characterized by a combustion zone propagating inside a porous medium (Fig. 1.5). Kennedy et al. (1999) give a thorough review of filtration combustion and discuss possible applications, including hydrogen production. A numerical approach for the investigation of filtration waves is discussed in Henneke and Ellzey (1999). The effects of different types of packed bed designs (Gavrilyuk et al., 2001; Bubnovich et al., 2007) as well as differences between packed

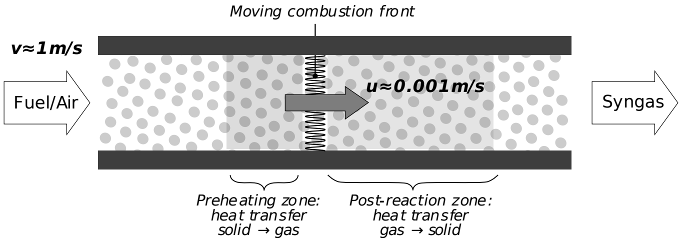

Figure 1.5: Filtration combustion.

beds and reticulated ceramics (Dhamrat and Ellzey, 2006; Fay et al., 2005) on the conversion of methane to hydrogen was investigated in both experiments and simulations. In addition, recent results for heptane (Dixon et al., 2008) verified the applicability of the concept for reforming of liquid hydrocarbon fuels.

The single most important disadvantage of fuel reforming in filtration waves is due to the propagating nature of the process. As superadiabatic temperatures are linked to co-flowing filtration waves, the reaction front will ultimately propagate out of a reactor of finite length. One technique to hold the combustion zone inside the reactor is to cyclically reverse the flow direction (Drayton et al., 1998), which, however, significantly complicates the reactor design.

Only a small number of studies have been conducted on alternative non-catalytic fuel reformer designs. Two-layer porous reactors with a stationary reaction zone have shown a limited capability of operation beyond the conventional rich flammability limits (Pedersen-Mjaanes et al., 2005). Results for reforming of methane/air mixtures in this reactor type show hydrogen concentrations around 12% at ϕ=1.8-1.85. Results from filtration combustion, however, yield H_2 concentrations beyond 15% at comparable conditions, where the differences are attributed to substantially higher combustion temperatures (Dixon et al., 2008). Peak temperatures in porous reactors remain close to the adiabatic equilibrium temperature (Barra and Ellzey, 2004), whereas in filtration waves, peak temperatures can exceed the adiabatic limit by a significant amount.

This work differs from previous research on non-catalytic fuel reforming, as it seeks to eliminate the need for moving combustion zones or flame holders. A recent

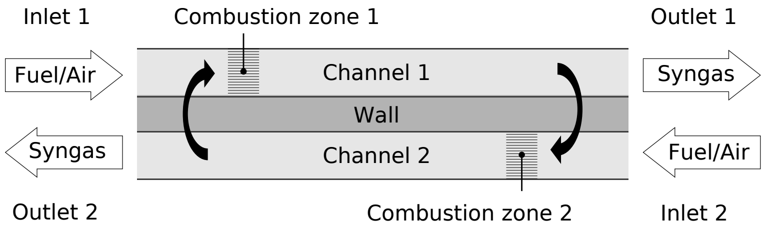

Figure 1.6: Fuel reformer based on counter-flow heat exchange between channels with opposing flow directions.

study on miniature swiss-roll combustors, while focusing on applications as radiant heaters, verified that swiss-roll designs can operate at moderately fuel-rich conditions (Kim et al., 2005). Based on a conceptually similar reactor design, the primary focus of this study is to investigate operation at ultra-rich equivalence ratios that are typical for non-catalytic fuel reforming.

1.3 Conceptual Approach

This work focuses on the investigation of a new fuel reformer concept with stationary combustion zones. Similar to Swiss Roll combustors (Lloyd and Weinberg, 1974; Vican et al., 2002; Kim et al., 2005; Ahn et al., 2005), heat is transferred from hot reaction products to cold reactants across a dividing wall, which enables combustion outside the conventional flammability limits (Jones et al., 1978). Swiss-roll combustors use a single channel with double-spiral geometry, forming a central chamber that, under normal operating conditions, contains the combustion process (Fig. 1.4b). Instead, the novel design uses separate adjacent channels without predefined combustion zone locations, where the use of straight channels simplifies the geometry significantly.

Figure 1.6 illustrates the heat exchange between two finite channels in counter-flow configuration, which are partitioned by a conducting wall. Combustion occurs in each of the two channels, which do not contain any internal flame holders. The unreacted fuel/air mixture in the top channel, with flow direction from left to right, is heated by counter-flow heat exchange from the hot combustion products in the bottom channel. The combustion zone stabilizes at a location where sufficient heat transfer promotes self-sustained reactions. Once reacted, the combustion products in the top channel flow towards the exit, and heat is transferred through the wall to preheat the incoming fuel/air mixture in the bottom channel. Since flow directions are opposite, gases in both channels undergo identical processes, where heat is added at the inlet and passed back to the adjacent channel at the exit. This continuous heat recirculation concentrates energy in the reactor center such that local temperatures can exceed the adiabatic flame temperature by a significant amount.

Thus far, only few studies were conducted on combustion concepts that use counter-flow heat exchange between parallel flow channels. Prior to this work, only the case of infinitely long channels had been investigated based on analytical models. Fursenko, et al. (2001) predicted superadiabatic temperatures for combustion with "counter filtration", and investigated stability in a follow-up study (Fursenko and Minaev, 2005). Ju and Choi (2003) followed a similar analytic approach, but neglected axial conduction along the channel walls.

Beyond the analytical studies mentioned above, no experimental or numerical studies have been conducted on combustion in straight channels with counter-flow heat exchange. In conceptual terms, however, many superadiabatic combustors that rely on heat exchange across dividing walls are variations of the same idea. Ju and Choi (2003) illustrated that combustion in two opposing channels is similar to two U-shaped reactors joined at the bottom of the "U", where the gases flow straight from one reactor into the other instead of being turned around at the channel bend. The annular concept studied by Marbach and Agrawal (2006) is a variant of the U-shaped combustor, where one side of the "U" is turned inside the other. Furthermore, U-shaped combustors can be seen as swiss-roll combustors with a single turn, e.g. (Ronney, 2003; Maruta et al., 2004). One important distinction between combustion in parallel channels and combustion in swiss-roll combustors, however, is that the latter concept has an internal cavity acting as a combustion chamber (Fig. 1.4b). Ahn, et al. (2005) compared the performance of swiss-roll reactors based on gas-phase and catalytic combustion, and showed that the use of catalysts broadened the rich operation limits considerably. Gas phase combustion at low flow rates occurred in a "flameless" mode near the reactor center, whereas for near-stoichiometric mixtures at high flow rates, visible flames stabilized close to the reactor inlets. Jones, et al. (1978) used a global approach to model the characteristics of a swiss roll burner. A more recent analytical solution for swiss-roll combustors was developed by Targett, et al. (1992).

Recent experiments by Maruta, et al. (2004) investigate the behavior of flames stabilized in small diameter quartz tubes with heated walls. Although an external heat source was used, the particular experimental setup was chosen to simulate conditions in a heat recirculating burner. While first results reported that the reaction zone widens considerably for mixtures far outside the conventional flammability limit (Maruta et al., 2004), a close inspection revealed that the wide shadowy regions observed in the initial study are caused by an oscillatory motion of *flames with repetitive extinction and ignition* (Maruta et al., 2005).

Reactors composed of channels with alternating flow directions do not contain any flame holders. Instead, combustion zone locations adjust freely and thus are expected to share some characteristics with free flames in narrow ducts. In a numerical study, Lee and T'ien (1982) showed that the presence of cold isothermal walls affects both flame quench and flame shape. Dunn-Rankin, et al. (1986) investigated flames propagating in a duct closed at one end and reported "tulip" shaped features, where flames appear to propagate faster in regions close to the wall (Rotman and Oppenheim, 1986). Numerical simulations of flames propagating in ducts (Lee and Tsai, 1994) showed two basic classes of flame shapes: "tulip" shaped flames are the preferred shape in the case of adiabatic walls, whereas "mushroom" shaped flames are the preferred shape for isothermal cold walls. Hackert, et al. (1998) reported numerical results illustrating that convectively and/or radiatively cooled walls alter both burning rate and flame shape significantly.

Kim and Maruta (2006) attributed the complex phenomena observed in combustion in ducts to the interaction of three mechanism: *thermal interaction* between flame and wall, *chemical interaction* between species in the flame and *momentum interaction* between flame and the flow field. While the first two interactions can be analyzed based on one-dimensional models, an investigation of the momentum interaction requires a more detailed approach. Due to flame stretch (Karlovitz et al., 1953), momentum interaction can significantly increase the burning rate. While most of the numerical research is based on single-step chemistry, Michaelis and Rogg (2004) presented results for detailed H_2-O_2 kinetics. The impact of the Lewis number on combustion in ducts was investigated by Chakraborty, et al. (2008). Transient effects and instabilities of combustion in microchannels are reported in Pizza, et al. (2008).

1.4 Objectives

The main focus of this work is to form a fundamental understanding of non-catalytic combustion processes that are stabilized by counter-flow heat exchange between adjacent flow channels. A simplified analytical model is developed to establish a theory of the physical mechanisms responsible for combustion zone stabilization. The feasibility of the concept is verified by experiments, where combustion of ultra-rich fuel/air mixtures typical for fuel reforming applications is investigated. Numerical work aims to deepen the understanding of the combustion process, where structure and two-dimensional effects are studied based on a detailed numerical model with multi-step reaction kinetics.

1.5 Methodology

As outlined in the objectives, superadiabatic combustion with counter-flow heat exchange is investigated, in chronological order, by analytical, experimental and numerical means. This work summarizes the efforts and is structured accordingly: Chapter 2 covers the analytical model, Chapter 3 details experimental work, and Chapter 4 is dedicated to detailed numerical simulations. Results pertaining to the individual chapters are summarized at the end of each chapter. Overall results are summarized in Chapter 5, which also covers conclusions and recommendations obtained from this study.

Analytical Model: The conceptual framework for the understanding of the novel reactor design is built on a simplified analytical model, which is described in Chapter 2 and was published in Schoegl and Ellzey (2007a). Using large activation energy asymptotics, an analytical solution of the mixed combustion/heat-transfer problem is found that is subsequently used to study the reactor behavior for varying inlet velocities and equivalence ratios. Two different configurations of combustion in adjacent channels, co-flow and counter-flow, are investigated. The co-flow configuration is equivalent to combustion in conducting tubes, and thus allows for a comparison of model predictions to observations available from experimental studies. Predictions for the counter-flow configuration are the actual objective of the study, and aim at basic information on the underlying physical processes and scaling laws for a practical design. Characteristics of superadiabatic combustion of a fuel-rich premixed fuel/air mixture are studied in terms of wall conductivity, heat transfer, and geometry of the combustor.

Experimental Work: The experimental work, summarized in Chapter 3, involves construction and testing of a series of reactor prototypes. The feasibility of the reactor design is verified in initial results from a prototype with two flow channels (Schoegl and Ellzey, 2007b). More comprehensive results are obtained for a redesigned reactor with four flow channels, where operating range and reforming efficiency are studied for rich methane/air mixtures (Schoegl and Ellzey, 2009). Additional results for rich propane/air mixtures illustrate differences between different hydrocarbon fuels, where the formation of soot precursors is studied (Schoegl et al., 2009).

Numerical Model: The purpose of the numerical model (Chapter 4) is to investigate the physical processes inside the reactor in detail. In particular, the structure of the reaction zone is studied based on a detailed two-dimensional model with detailed reaction kinetics for methane/air combustion (GRI 2.11). The numerical model is built on the computational fluid dynamics (CFD) package FLUENT (Fluent Inc., 2006), which has the capability of solving full Navier-Stokes equations as well as reaction kinetics in a transient formulation. Once steady state is approached, the computational grid is refined for a final solution, which is then analyzed in order to investigate the structure of the combustion zone.

Chapter 2

Analytical Model

This chapter covers the development of an analytical model for steady-state combustion in two finite parallel channels divided by a conducting wall, where both co-flow and counter-flow configurations are considered. The one-dimensional model is based on simplifying assumptions, where thermophysical properties are assumed to be constant, the combustion process is approximated using activation energy asymptotics and radiative heat losses are only considered in the boundary condition for the wall temperature solution. One complicating factor is that the locations of the combustion zones within the channels are not known *a priori*, but instead are determined by heat transfer processes. The model aims to predict combustion zone locations and peak temperatures based on velocity, temperature and composition of the gases upstream of the channel inlets. The development of the simplified analytical model as well as results for co-flow and counter-flow configuration, detailed below in Sections 2.2, 2.3 and 2.4, were published in Schoegl and Ellzey (2007a). Additional details on the development of the analytical model are discussed in Appendices A and B.

Compared to classical analytical solutions in combustion theory, combustion in heat exchangers shows additional length-scales. Next to length scales following from thermal diffusion and species diffusion in the gas phase, the inclusion of a solid wall introduces length scales due to solid conduction along the walls as well as the channel length itself. The solution process is based on the observation that the coupling of gas temperature and species concentration appears only in a source term representing the combustion process. This source term, however, vanishes outside of the immediate surroundings of the combustion zone, and the remaining terms represent a regular heat transfer problem. Thus, the overall problem is split in two parts: on the *microscopic* level, flow rates are related to peak temperatures by means of a simplified representation of combustion kinetics, whereas on the *macroscopic* level, heat exchange between two adjacent flow channels across a conducting wall is investigated.

Analytical solutions for combustion in channels with opposing gas flows have been previously presented by Fursenko, et al. (2001) as well as Ju and Choi (2003). Both groups investigate the characteristics of combustion in infinite parallel channels, which differ significantly from the behaviour of combustion in finite channels. Exit temperatures in infinite channels have to match the inlet temperatures, whereas in the case of a finite reactor, hot combustion products can exit at the outlet. In a model developed for a finite reactor length, parts of the solution are forced to vanish as the channel length tends to infinity, making external heat losses the only form of heat dissipation. Due to this difference, the present analytical model reveals additional behaviors not described in earlier studies.

2.1 Related Work

In combustion theory, analytical approaches using asymptotic solutions were first studied by the Russian school around researchers like Semenov, Zel'dovich, and Frank-Kamenetskii, and reached Western research circles only after a significant delay (Buckmaster et al., 2005). Singular perturbation methods using activation energy asymptotics were formally introduced by Bush and Fendell (1970), and initially applied to problems of free premixed flames. By matching of solutions for outer and inner length-scales of the combustion problem, they obtained an analytical solution to the laminar flame speed of an adiabatic flame. Buckmaster (1976) studied a similar problem for a flame subject to heat losses. In the following years, similar approaches were used for a stability analysis of non-adiabatic flames (Joulin and Clavin, 1979) as well as a radiation model for gas flows seeded with inert, solid particles (Joulin, 1987).

Takeno and Sato (1979) first proposed the insertion of a porous matrix for a superadiabatic burner in a theoretical analysis, where they studied the combustion of a premixed flame in a porous solid based on the assumption that the solid temperature is equal to the adiabatic flame temperature. In two following papers, the same problem was solved using asymptotic expansions on a semi-infinite domain (Deshaies and Joulin, 1980), and using an implicitly defined intermediate solid temperature on a bounded domain (Buckmaster and Takeno, 1981). More recently, simultaneous analytical solutions for gas and porous media were developed for cases where the flame is stabilized close to the exit face of the burner (McIntosh and Prothero, 1991; Golombok et al., 1991). Full asymptotic solutions of gas temperature, gas concentration and solid temperature for filtration waves in a packed bed are described in Gort and Brouwers (2001), as well as for flames propagating in a narrow channel in Ju and Xu (2005).

In a paper on free premixed flames in generic flow fields, Matkowsky and Sivashinsky (1979) showed that the inner solution of the flame sheet can be approximated to first order by a delta function, where the strength was obtained from the solution of the simpler case of a rectilinearly propagating flame front. This result has been used by a series of studies, including the present one, to obtain analytical results in combustion problems. Zamashchikov and Minaev (2001) investigated the limits of flame propagation in a narrow channel. Maruta, et al. (2005) used asymptotics to study a flame stabilized in a narrow channel with a temperature gradient, where the wall temperature is imposed by a generic profile.

Due to the simplicity of the approach, solutions using activation energy asymptotics are incapable of resolving the flame structure. In order to account for characteristic chemical reactions describing different layers inside of the reaction zone, rate-ratio

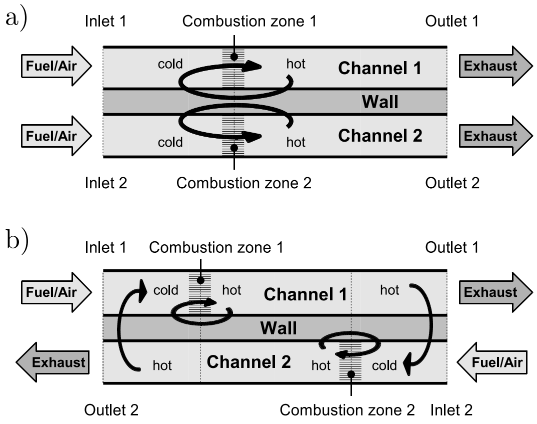

Figure 2.1: Concept of combustion in heat exchanger: heat recirculation in co-flow configuration (a) and counter-flow configuration (b).

asymptotics was developed (Buckmaster et al., 2005). In particular, a recent paper (Seshadri et al., 2001) investigated the asymptotic flame structure of a fuel rich flame ($\phi > 1.3$), which can be separated into an inert preheat zone, a thin reaction zone and a post-flame zone. Rate-ratio asymptotics, however, still fails to account for momentum interaction between combustion layer and flow field inside the channel. Thus, the approach chosen for the present study is to develop a basic understanding of the physical process based on a simplified analytical model, discussed below, whereas a more detailed understanding of the structure of the reaction zone is gathered from a detailed numerical model, developed in Chapter 4.

2.2 Mathematical Model

Figure 2.1 illustrates the heat exchange between two channels in co-flow and counter-flow configuration. In the co-flow case (Fig. 2.1a), heat is transferred by solid conduction from the hot combustion products to the preheating zone, which raises the temperature of the unburned fuel/air mixture, enabling superadiabatic conditions. In the counter-flow configuration (Fig. 2.1b) an additional feedback loop is formed, in which the hot combustion products in one channel preheat the cold fuel/air mixture in

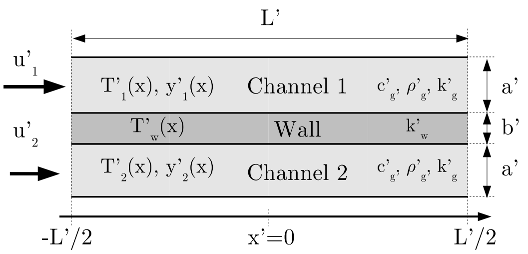

Figure 2.2: Channel setup (illustrated for co-flow configuration).

the adjacent channel. In both cases, the channels do not contain any internal flame holders and hence the combustion zones are not fixed at predefined axial positions. The following analysis shows that flame stabilization occurs at locations that follow indirectly from heat transfer between the channels and the wall.

The mathematical model presented in this paper takes mass flux and energy content of the specific fuel/air mixture as inputs to compute flame location and peak temperature at steady-state conditions. All physical/chemical processes are assumed to be one-dimensional in the axial direction, where convective heat transfer to and from the wall accounts for the lateral coupling between the channels. An additional convective term models external heat losses from the wall to the environment. Within the scope of the model, thermophysical properties of gas and solid wall are assumed to be constant. While radiative heat losses from the reactor faces are included in the boundary conditions, radiation inside the reactor is not modeled. Detailed numerical simulations of porous burners (Barra and Ellzey, 2004) show that at the lean flammability limit, conductive heat transfer is the primary source of heat recirculation up to a flame speed five times higher than the laminar flame speed, above which radiation outweighs conduction. Since radiation enhances the conductive heat transfer, the simplified model will under-predict the enhancement of the flame speed by heat recirculation.

2.2.1 Governing equations

The model comprises separate gas- and solid-phase equations for two adjacent flow channels divided by a conducting wall (Fig. 2.2). Initially, the flow velocities u'_i in the individual channels are assumed to be arbitrary, which allows for the simultaneous treatment of co-flow and counter-flow configurations. In each channel, the gas temperature is governed by mass transport, thermal diffusion, convective heat exchange with the wall, and heat generated by the chemical reactions. Similarly, the concentration of the species that limits the reaction process is determined by mass transport, molecular diffusion and species consumption. Using the mathematical symbols defined in the nomenclature, the steady-state governing equations for the gas temperature T'_i and the concentration of the limiting species y'_i are given by

$$\rho'_g c'_g u'_i \frac{dT'_i}{dx'} = k'_g \frac{d^2 T'_i}{dx'^2} - \frac{h'_w}{a'} \left(T'_i - T'_w\right) + Q' w' \left(T'_i, y'_i\right) \tag{2.1a}$$

$$\rho'_g u'_i \frac{dy'_i}{dx'} = \rho'_g \mathcal{D}'_g \frac{d^2 y'_i}{dx'^2} - w' \left(T'_i, y'_i\right) \tag{2.1b}$$

where $i = 1, 2$ identifies the channels and primes $'$ denote dimensional quantities. The exothermic chemical reactions are modeled by single-step, first order, irreversible Arrhenius kinetics so that the rate expression

$$w' \left(T'_i, y'_i\right) = Z' \rho'_g y'_i \exp\left(-\frac{E'_a}{R' T'_i}\right) \tag{2.2}$$

describes the coupling between gas temperature and species concentration within each channel.

The thermal interaction between the gas temperatures inside the individual channels is captured by the wall model, which includes axial conduction within the solid, convective heat exchange with the flowing gases and heat losses to the environment, i.e.

$$k'_w \frac{d^2 T'_w}{dx'^2} \quad = \quad \frac{h'_w}{b'}\left(2T'_w - T'_1 - T'_2\right) + \frac{h'_\infty}{b'}\left(T'_w - T'_\infty\right). \tag{2.3}$$

Upstream and downstream of the channels, the gases are assumed to be governed by an adiabatic transport process, which leads to Dirichlet boundary conditions at the channel inlets and outlets. Furthermore, the radiative heat loss terms

$$k'_w \frac{dT'_w}{dx'} \quad = \pm \quad \varepsilon \sigma'_B \left({T'_w}^4 - {T'_\infty}^4 \right)$$

describe the boundary conditions at both ends of the dividing wall, where the plus/minus signs pertain to left and right reactor faces, respectively.

2.2.2 Non-dimensional Equations

Starting with Equations 2.1a through 2.3, the axial coordinate of the channel x' is rescaled to the interval $[-1, 1]$, and the concentration y' is scaled to the initial concentration of the limiting species y'_0. Furthermore, the temperatures T'_i are normalized by a reference temperature T'_{ref} and the flow velocities are scaled by a reference velocity u'_{ref}. Thus the scaled variables of the process are given by

$$x = \frac{2x'}{L'}, \; y = \frac{y'}{y'_0}, \; T_i = \frac{T'_i}{T'_{\text{ref}}}, \; u_i = \frac{u'_i}{u'_{\text{ref}}}$$

where the reference values T'_{ref} and u'_{ref} are used to decouple the thermal properties of the reactor from characteristics of the combustion process.

In a first approximation, the reaction terms of the non-adiabatic process are treated as a perturbation of the classical solution of the adiabatic flame speed (Bush and Fendell, 1970). For any air/fuel mixture, the adiabatic flame speed is characterized by the eigenvalue

$$\Lambda \approx Z'\alpha'_g / {u'_{\mathrm{ad}}}^2 \exp\left(-E'_a/R'T'_{\mathrm{ad}}\right) \tag{2.4}$$

where u'_{ad} is the adiabatic flame speed associated with the adiabatic equilibrium temperature $T'_{\mathrm{ad}} = T'_u + \Delta T'_{\mathrm{ad}}$, which is determined by the temperature of the unburned fuel/air mixture T'_u and the adiabatic temperature rise $\Delta T'_{\mathrm{ad}} = y'_0 Q'/c'_g$ corresponding to the energy content of the mixture. Using a specific air/fuel mixture as a reference, the previously introduced values u'_{ref} and T'_{ref} can be assigned to flame speed and adiabatic equilibrium temperature of the reference case, respectively, and the non-dimensional reaction terms become

$$w_i \approx y_i \Lambda \exp\left(\frac{\beta\,(T_i - T_{\mathrm{ad}})}{T_i/T_{\mathrm{ad}}}\right) \tag{2.5}$$

where $\beta = \mathrm{Ze}/\gamma$ is a non-dimensional activation energy, $\mathrm{Ze} = E'_a \Delta T'_{\mathrm{ad}}/R'\,{T'_{\mathrm{ad}}}^2$ is the Zeldovich number and $\gamma = \Delta T'_{\mathrm{ad}}/T'_{\mathrm{ref}}$ follows from the temperature scaling. While the adiabatic flame speed of different fuel/air mixtures is traditionally evaluated at a common reference temperature, it is, in effect, a function of both the equivalence ratio ϕ and the temperature of the unburned fuel/air mixture T'_u. By requiring $u'_{\mathrm{ad}} = u'_{\mathrm{ref}}$ in the derivation of Equation 2.5, however, the flame speed is fixed a priori, and the temperature of the unburned gases must be adjusted to yield the desired velocity. As a consequence, T_{ad} is referenced to an initial temperature that depends on the equivalence ratio, and the non-dimensional parameters T_{ad} and β become functions of ϕ.

Introducing the non-dimensional parameters ϵ, μ, κ and χ to quantify reactor length, gas-/solid heat transfer, axial conduction and external heat losses, respectively, as well as using the Lewis number Le, the steady-state equations for temperatures and concentration are rewritten in non-dimensional form as

$$\frac{d^2T_w}{dx^2} = \frac{\mu}{\kappa\epsilon^2}\left[(1+\chi)\,T_w - \frac{1}{2}(T_1+T_2) - \chi T_\infty\right] \tag{2.6a}$$

$$\frac{d^2T_1}{dx^2} = \frac{u_1}{\epsilon}\frac{dT_1}{dx} + \frac{\mu}{\epsilon^2}(T_1 - T_w) - \frac{\gamma}{\epsilon^2}w_1 \tag{2.6b}$$

$$\frac{d^2T_2}{dx^2} = \frac{u_2}{\epsilon}\frac{dT_2}{dx} + \frac{\mu}{\epsilon^2}(T_2 - T_w) - \frac{\gamma}{\epsilon^2}w_2 \tag{2.6c}$$

and

$$\frac{1}{\mathrm{Le}}\frac{d^2y_1}{dx^2} = \frac{u_1}{\epsilon}\frac{dy_1}{dx} + \frac{1}{\epsilon^2}w_1 \tag{2.7a}$$

$$\frac{1}{\mathrm{Le}}\frac{d^2y_2}{dx^2} = \frac{u_2}{\epsilon}\frac{dy_2}{dx} + \frac{1}{\epsilon^2}w_2 \tag{2.7b}$$

Since the problem is scaled to the length of the heat exchanger, the choice of normalized variables differs from the normalization typically used in asymptotic solutions of combustion problems (Fursenko et al., 2001; Matkowsky and Sivashinsky, 1979; Williams, 1985; Ju and Minaev, 2002), where the equations are based on the length scale of gas diffusion. However, by rescaling Equations 2.6 and 2.7 with the alternative axial coordinate $\xi = x/\epsilon$ the equations can be easily transformed to the traditional form.

2.2.3 Asymptotics

Assuming large activation energy, the exponential term in Equation 2.5 vanishes for $T_i \ll T_{\mathrm{ad}}$ and it can be assumed that the chemistry is frozen until the gas temperatures approach the vicinity of the peak temperature, where the reactions complete quickly due to the rapidly increasing reaction rate. As a consequence, the combustion zones are assumed to be thin compared to the length of the channels and thus can be replaced by localized sources. Assuming complete consumption of the limiting species, as well as truncating results from activation energy asymptotics (Matkowsky and Sivashinsky,

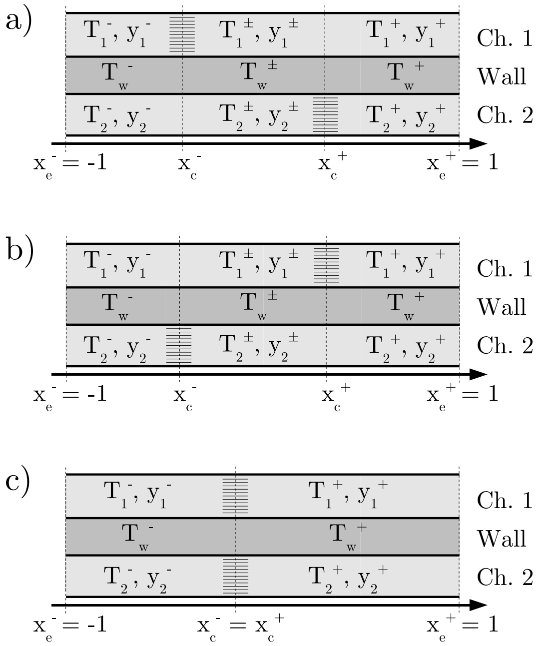

Figure 2.3: Solution domain is divided into segments between channel inlets/outlets and combustion zones (hatched areas): combustion zone in channel 1 left of combustion zone in channel 2 (a), combustion zone in channel 1 right of combustion zone in channel 2 (b), and combustion locations coincide and middle section collapses to zero length (c).

1979) after the second term, the reaction rate expressions are approximated by

$$w_i \quad \approx \quad \epsilon\delta\left(x - x_{c,i}\right)\exp\left(\frac{\beta\left(T_i - T_{\mathrm{ad}}\right)}{2T_i/T_{\mathrm{ad}}}\right) \tag{2.8}$$

where $\delta\left(x - x_{c,i}\right)$ are Dirac delta functions representing point sources.

In the general case of combustion in a heat exchanger, the velocities in the individual channels are arbitrary, and the locations of the combustion fronts are independent. Using the approximation of infinitesimally thin reaction zones, the overall domain of the reactor is subdivided into sections defined by the positions of the combustion zones (Fig. 2.3). Thus, the original non-linear governing equations become a set of three piecewise-linear differential equations linked by internal boundary conditions at the reaction front locations.

2.2.4 Boundary Conditions

Figure 2.3 illustrates that the problem is divided into subsections defined on the intervals $[x_e^-, x_c^-]$, $[x_c^-, x_c^+]$ and $[x_c^+, x_e^+]$, where $x_e^{-/+}$ denote left and right channel end-points and $x_c^{-/+}$ mark left and right combustion locations, respectively. The external and internal boundary conditions for the governing equation of the wall are given by radiative heat losses at the channel end points $x_e^{-/+}$

$$\frac{dT_w}{dx} = \pm\sigma\left({T_w}^4 - {T_\infty}^4\right) \tag{2.9}$$

as well as continuity at the internal boundary at the combustion locations $x_c^{-/+}$

$$[T_w]_-^+ = \left[\frac{dT_w}{dx}\right]_-^+ = 0 \tag{2.10}$$

where $[f]_-^+$ denotes the difference of function values to the left and right of an internal boundary.

The boundary conditions for the gas phase follow from the solution of an adiabatic transport process outside the channels as well as the requirement of complete consumption of the reactants. Depending on the flow direction of the individual channels, the boundary conditions at left and right reactor end-points $x_e^{-/+}$ are either given by

$$\frac{dT_i}{dx} = \frac{u_i}{\epsilon}\left(T_i - T_0\right) \tag{2.11a}$$

$$\frac{dy_i}{dx} = \frac{u_i \mathrm{Le}}{\epsilon}\left(y_i - y_0\right) \tag{2.11b}$$

for an inlet or

$$\frac{dT_i}{dx} = 0 \tag{2.12a}$$

$$y_i = \frac{dy_i}{dx} = 0 \tag{2.12b}$$

for an outlet, where initial temperature and concentration are given by T_0 and $y_0 = 1$, respectively.

Inside the channels, the gas temperature and species distributions are continuous at both combustion locations $x_c^{-/+}$, i.e.

$$[T_i]_-^+ = 0 \tag{2.13a}$$

$$[y_i]_-^+ = 0 \tag{2.13b}$$

Integrating Equations 2.6b and 2.6c as well as 2.7a and 2.7b across the reaction fronts yields jump conditions for the derivatives of temperature and species concentration. Depending on the locations of the combustion fronts, the remaining internal boundary conditions become

$$\left[\frac{dT_i}{dx}\right]_-^+ = \frac{\gamma}{\epsilon}\exp\frac{\beta\,(T_i - T_{\mathrm{ad}})}{2T_i/T_{\mathrm{ad}}} \tag{2.14a}$$

$$\left[\frac{dy_i}{dx}\right]_-^+ = -\frac{\mathrm{Le}}{\epsilon}\exp\frac{\beta\,(T_i - T_{\mathrm{ad}})}{2T_i/T_{\mathrm{ad}}} \tag{2.14b}$$

in case the combustion at x_c occurs in channel i or

$$\left[\frac{dT_i}{dx}\right]_-^+ = 0 \tag{2.15a}$$

$$\left[\frac{dy_i}{dx}\right]_-^+ = 0 \tag{2.15b}$$

when it takes place in the adjacent channel.

2.3 Analysis

By splitting the solution domain into segments describing the conditions upstream, in-between and downstream of the combustion zones (Fig. 2.3), the coupling between species concentration and temperature only appears in the internal boundary conditions. Using the boundary conditions at the reactor inlet and outlet (Eqs. 2.11b, 2.12b) and continuity (Eqs. 2.13b, 2.15b), the solution of the concentration of the limiting species y (Eq. 2.7) can be obtained independent of the jump condition at the reaction front as

$$y_i \quad = \quad \begin{cases} 0 & \text{, Downstream } x_{c,i} \\ 1 - \exp\left(-\mathrm{Le}\frac{u_i}{\epsilon}\left(x - x_{c,i}\right)\right) & \text{, Upstream } x_{c,i} \end{cases} \tag{2.16}$$

which gives the solution of the distribution of the species concentrations throughout the channels. Furthermore, substituting Equation 2.16 into the jump condition (Eq. 2.14b) yields expressions relating the flow velocities to the peak temperatures as

$$|u_i| \quad = \quad \exp\frac{\beta\left(T_{c,i} - T_{\mathrm{ad}}\right)}{2T_{c,i}/T_{\mathrm{ad}}} \tag{2.17}$$

which establishes the last expression required to solve for the unknown temperature distributions. Based on Equation 2.17, it is possible to relate the peak temperature of a combustion zones to the flow velocity without any knowledge of the reactor geometry. Equation 2.17 does not, however, reveal any information on existence or position of a combustion zone in a specific reactor at a predefined velocity, which can only be obtained from the solution to the heat transfer problem given by Equation 2.6.

In the following, the temperature distribution in a single segment defined on the interval $[x_n, x_p]$ is found in general terms, which is subsequently used to find the overall solution. Introducing the dimensionless heat fluxes $\psi_i = \frac{d}{dx}T_i$ as well as the vectors

$$\boldsymbol{T}^T = \begin{bmatrix} T_w & T_1 & T_2 \end{bmatrix}, \qquad \boldsymbol{\psi}^T = \begin{bmatrix} \psi_w & \psi_1 & \psi_2 \end{bmatrix},$$

the original second-order differential equations (Eqs. 2.6a, 2.6b, 2.6c) can be rewritten as a system of first-order differential equations

$$\frac{d}{dx}\begin{bmatrix} \boldsymbol{T} \\ \boldsymbol{\psi} \end{bmatrix} = \begin{bmatrix} \mathbf{0} & \mathbf{I} \\ \mathbf{C} & \mathbf{D} \end{bmatrix}\begin{bmatrix} \boldsymbol{T} \\ \boldsymbol{\psi} \end{bmatrix} - \begin{bmatrix} \mathbf{0} \\ \mathbf{E} \end{bmatrix}\begin{bmatrix} \boldsymbol{T}_\infty \end{bmatrix}, \tag{2.18}$$

where the sub-matrices **0** and **I** are zero and identity matrix, $\boldsymbol{T}_\infty^T = T_\infty[1\ 1\ 1]$, and **C**, **D** and **E** are given by

$$\begin{aligned} \mathbf{C} &= \frac{\mu}{\epsilon^2}\begin{bmatrix} \frac{1+\chi}{\kappa} & -\frac{1}{2\kappa} & -\frac{1}{2\kappa} \\ -1 & 1 & 0 \\ -1 & 0 & 1 \end{bmatrix}, \\ \mathbf{D} &= \frac{1}{\epsilon}\mathrm{diag}\left(0, u_1, u_2\right), \\ \mathbf{E} &= \frac{\mu}{\epsilon^2}\mathrm{diag}\left(\frac{\chi}{\kappa}, 0, 0\right) \end{aligned}$$

Using the substitution $\tilde{\boldsymbol{T}}(x) = \boldsymbol{T}(x) - \boldsymbol{T}_\infty$, Equation 2.18 can be solved directly based on the eigenvalues of the system, which are the solution of the characteristic polynomial

$$\sum_{i=0}^{6} d_i \lambda^i = 0 \tag{2.19}$$

with

$$
\begin{aligned}
d_6 &= 1 \\
d_5 &= -\frac{1}{\epsilon}\left(u_1 + u_2\right) \\
d_4 &= \frac{u_1 u_2}{\epsilon^2} - \frac{\mu}{\kappa\epsilon^2}\left(1 + 2\kappa + \chi\right) \\
d_3 &= \frac{\mu}{\kappa\epsilon^3}\left(u_1 + u_2\right)\left(1 + \kappa + \chi\right) \\
d_2 &= \frac{\mu^2}{\kappa\epsilon^4}\left(1 + \kappa + 2\chi\right) - \frac{u_1 u_2 \mu}{\kappa\epsilon^4}\left(1 + \chi\right) \\
d_1 &= -\frac{\mu^2}{2\kappa\epsilon^5}\left(u_1 + u_2\right)\left(1 + 2\chi\right) \\
d_0 &= -\frac{\chi\mu^3}{\kappa\epsilon^6}
\end{aligned}
$$

Assuming distinct, non-zero eigenvalues as well as introducing the matrix operator

$$\mathbf{\Lambda}\left(x\right) = \operatorname{diag}\left(\Lambda_1\left(x\right), \Lambda_2\left(x\right), \ldots \Lambda_6\left(x\right)\right)$$

with

$$\Lambda_i\left(x\right) = \begin{cases} \exp\left(\lambda_i\left(x - x_n\right)\right), & \lambda_i < 0 \\ \exp\left(\lambda_i\left(x - x_p\right)\right), & \lambda_i > 0 \end{cases}$$

the solution of temperature and heat flux distribution can be written as

$$\begin{bmatrix} \tilde{\boldsymbol{T}}\left(x\right) \\ \boldsymbol{\psi}\left(x\right) \end{bmatrix} = \begin{bmatrix} \mathbf{V}_T \\ \mathbf{V}_\psi \end{bmatrix} \begin{bmatrix} \mathbf{\Lambda}\left(x\right)\mathbf{c} \end{bmatrix} \tag{2.20}$$

where the $\mathbf{V}_j$ are formed from the eigenvectors and the constant vector $\mathbf{c}$ has to be determined from the boundary conditions.

Having found the solution for a single section, the individual segments of the problem will be labeled using the superscripts $^-$ for the segment defined on the interval $[x_e^-, x_c^-]$, $^\pm$ for the interval $[x_c^-, x_c^+]$, and $^+$ for the interval $[x_c^+, x_e^+]$. Thus, the solutions for the channel temperatures and heat fluxes can be written as

$$\boldsymbol{T}^{-}(x) = \boldsymbol{T}_{\infty} + \mathbf{V}_T \boldsymbol{\Lambda}^{-}(x)\,\mathbf{c}^{-} \tag{2.21a}$$

$$\boldsymbol{T}^{\pm}(x) = \boldsymbol{T}_{\infty} + \mathbf{V}_T \boldsymbol{\Lambda}^{\pm}(x)\,\mathbf{c}^{\pm} \tag{2.21b}$$

$$\boldsymbol{T}^{+}(x) = \boldsymbol{T}_{\infty} + \mathbf{V}_T \boldsymbol{\Lambda}^{+}(x)\,\mathbf{c}^{+} \tag{2.21c}$$

and

$$\boldsymbol{\psi}^{-}(x) = \mathbf{V}_{\psi} \boldsymbol{\Lambda}^{-}(x)\,\mathbf{c}^{-} \tag{2.22a}$$

$$\boldsymbol{\psi}^{\pm}(x) = \mathbf{V}_{\psi} \boldsymbol{\Lambda}^{\pm}(x)\,\mathbf{c}^{\pm} \tag{2.22b}$$

$$\boldsymbol{\psi}^{+}(x) = \mathbf{V}_{\psi} \boldsymbol{\Lambda}^{+}(x)\,\mathbf{c}^{+} \tag{2.22c}$$

where the three constant vectors $\mathbf{c}^{-}$, $\mathbf{c}^{\pm}$ and $\mathbf{c}^{+}$ still need to be determined from the external and internal boundary conditions. Rewriting the external boundary conditions at the channel inlets/outlets (Eqs. 2.9, 2.11a, 2.12a) in matrix notation yields

$$\boldsymbol{\psi}^{-}(x_e^{-}) - (\mathbf{K}^{-} + \mathbf{J}^{-})\,\boldsymbol{T}^{-}(x_e^{-}) = -\mathbf{K}^{-}\boldsymbol{T}_0 - \mathbf{J}^{-}\boldsymbol{T}_{\infty} \tag{2.23a}$$

$$\boldsymbol{\psi}^{+}(x_e^{+}) - (\mathbf{K}^{+} - \mathbf{J}^{+})\,\boldsymbol{T}^{+}(x_e^{+}) = -\mathbf{K}^{+}\boldsymbol{T}_0 + \mathbf{J}^{+}\boldsymbol{T}_{\infty} \tag{2.23b}$$

where $\boldsymbol{T}_0^T = T_0[1\;1\;1]$,

$$\mathbf{K}^{-/+} = \operatorname{diag}\left(0, k_1^{-/+}, k_2^{-/+}\right), \tag{2.24}$$

$$k_i^{-/+} = \begin{cases} u_i/\epsilon & \text{, Inlet} \\ 0 & \text{, Outlet} \end{cases}$$

characterizes the convective boundary condition of the gas phase and

$$\mathbf{J}^{-/+} = \operatorname{diag}\left(j^{-/+}, 0, 0\right), \tag{2.25}$$

$$j^{-/+} = \sigma\left(T_w^{-/+} + T_{\infty}\right)\left(T_w{}^2 + T_{\infty}^{-/+\,2}\right)$$

contains the partially linearized boundary condition for the radiative heat losses from the reactor faces.

Furthermore, the internal boundary conditions at the two reaction front locations (Eqs. 2.13a, 2.14a, 2.15a) can be expressed as

$$\begin{aligned} \boldsymbol{T}^{-}(x_c^-) - \boldsymbol{T}^{\pm}(x_c^-) &= \mathbf{0} && (2.26a) \\ \boldsymbol{T}^{\pm}(x_c^+) - \boldsymbol{T}^{+}(x_c^+) &= \mathbf{0} && (2.26b) \\ \boldsymbol{\psi}^{-}(x_c^-) - \boldsymbol{\psi}^{\pm}(x_c^-) &= \mathbf{s}^{-} && (2.26c) \\ \boldsymbol{\psi}^{\pm}(x_c^+) - \boldsymbol{\psi}^{+}(x_c^+) &= \mathbf{s}^{+} && (2.26d) \end{aligned}$$

where Equation 2.17 has been used to simplify the nonlinear source terms to

$$\begin{aligned} \mathbf{s}^{-/+} &= \begin{bmatrix} 0 & s_1^{-/+} & s_2^{-/+} \end{bmatrix}^T && (2.27) \\ s_i^{-/+} &= \begin{cases} |u_i|\,\gamma/\epsilon & \text{, Source} \\ 0 & \text{, No source} \end{cases} \end{aligned}$$

Formally, Equations 2.23 and 2.26 represent a non-linear equation system of six 3×1 vector equations for three unknown 6×1 vectors, which has to be solved iteratively.

2.4 Results and Discussion

At equivalence ratios outside the conventional rich or lean flammability limits, the concepts of flame speed and flame temperature need to be re-evaluated. In classical theory, both concepts are based on adiabatic conditions and thus can be defined even as the reactant concentration approaches zero (Law, 2006). In practice, however, a stable flame is not realizable outside the flammability limits and hence a flame speed, in a physical sense, becomes meaningless. The concept behind superadiabatic combustion is that an increase in the local temperature enhances the reaction rates, which also causes a broadening of the limits of flammability (Glassman, 1996). This has to be

ϕ	T'_u [K]	T'_{ad} [K]	u' [cm/s]	$\rho' u'$ [g/cm^2/s]	E'_a [J/mol]
1.4	136.0	1864	3.80	9.2962e-03	245573
1.6[a]	**298.0**	1834	8.38	9.2901e-03	243788
1.8	427.7	1801	12.11	9.2872e-03	241824
2.0	537.9	1771	15.36	9.3005e-03	240038
2.2	624.6	1742	17.95	9.2963e-03	238312
2.4	703.7	1712	20.37	9.3009e-03	236527
2.6	770.6	1686	22.44	9.2969e-03	234979
2.8	829.2	1660	24.25	9.2780e-03	233432
3.0	877.4	1639	25.90	9.3085e-03	232182
3.2	916.3	1619	27.12	9.2750e-03	230991
3.4	957.7	1605	28.56	9.2934e-03	230158
3.6	995.9	1593	29.95	9.3174e-03	229444

[a] Reference conditions.

Table 2.1: Simulation results for rich premixed methane/air combustion at constant mass flow rate $\rho' u'$.

contrasted to the commonly used conventional flammability limit, which refers to an empirical value determined in standardized configurations under standard atmospheric conditions (Glassman, 1996; Law, 2006).

As discussed in Section 2.2.2, a common reference speed is defined for varying air/fuel mixtures, which is achieved by raising the temperature of the unburned mixture to a level that ensures the reaction rate corresponding to the required flow velocity. As superadiabatic combustion in both rich and lean regimes is based on the same heat transfer mechanisms, the discussion will focus on operation under fuel-rich conditions. In the following, the reference speed is based on fuel-rich combustion of a methane/air mixture with ϕ=1.6 and T'_u= 298 [K], which is close to the conventional rich flammability limit at ϕ=1.7 (Glassman, 1996).

Table 2.1 gives an overview of numerical results from the combustion code PREMIX (Kee et al., 1985) based on the reaction mechanism GRI-MECH 3.0 (Smith et al., 1999), where the temperature of the unburned mixture was adjusted to yield a constant mass flux for equivalence ratios between ϕ = 1.4 and 3.6. In addition, Table 2.1 gives

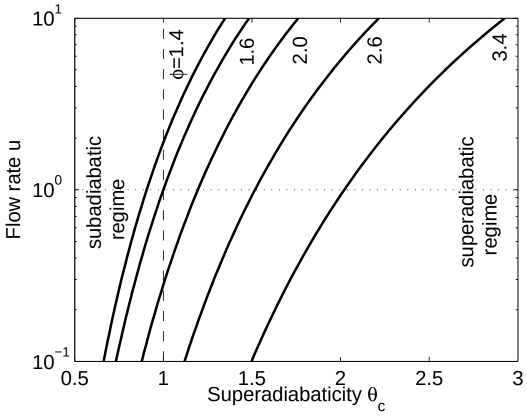

Figure 2.4: Relation between superadiabaticity and flow rate at different equivalence ratios.

mixture-dependent parameter fits for global activation energies E'_a used in the single-step Arrhenius-type kinetics model given by Equation 2.2. The parameter fits are based on combustion temperatures which result in the reference speed at any particular equivalence ratio. Thus, the single-step kinetics model is calibrated at the conditions given in Table 2.1 and acts as an approximation of the detailed reaction mechanism. A complete discussion of the procedure is given in Appendix B.

One of the main objectives of this study is to investigate superadiabatic combustion of mixtures close to and outside the conventional flammability limits. Superadiabatic combustion occurs whenever the peak temperature in the combustion zone exceeds the adiabatic value of the incoming fuel/air mixture, i.e. $T'_c > T'_0 + \Delta T'_{ad}$. Defining the "adiabaticity" of the combustion process as the non-dimensional temperature difference

$$\theta_c = \frac{T'_c - T'_0}{T'_{\text{ad}} - T'_u} = \frac{1}{\gamma}(T_c - T_0) \tag{2.28}$$

superadiabatic combustion is characterized by $\theta_c > 1$, and subadiabatic combustion occurs for $\theta_c < 1$. Figure 2.4 shows the dependence of the non-dimensional velocity on the combustion temperatures (Eq. 2.17) in terms of θ_c, where the individual curves represent different equivalence ratios of a methane/air mixture. Figure 2.4 illustrates that a small change in adiabaticity results in a large change in non-dimensional velocity.

As $u = 1$ corresponds to the adiabatic laminar flame speed close to the conventional rich flammability limit, it follows that external heat losses mandate $u > 1$ in most practical applications. Thus, mixtures with $\phi < 1.6$ can react in both sub- and superadiabatic regimes, whereas operation of a practical burner outside the conventional flammability limits ($\phi > 1.7$) requires heat addition generally resulting in superadiabatic conditions.

Under the assumption of a thin reaction zone and complete consumption of the reactants, the relation between velocity and peak combustion temperature does not depend on the parameters of the reactor, i.e. the relation between flow rate and peak temperature is driven by reaction kinetics whereas the temperature profiles are determined by heat transfer processes. This assumption is fundamentally different from models based on well-stirred reactors (Ronney, 2003), which depend on incomplete consumption of the reactants and thus operate at lower temperatures (Glassman, 1996). While the counter-flow design is conceptually similar to swiss-roll burners, the concepts differ at the extinction limits. At these limits, combustion in a swiss-roll burner occurs in the central chamber instead of a channel, which allows for enhanced mixing of reactants and products and thus may change the combustion characteristics.

In general, the assumption of a thin reaction zone can only be verified by numerical simulations with a detailed reaction mechanism. However, it is still possible to draw parallels between superadiabatic combustion in a heat recirculating burner and superadiabatic filtration waves for comparable fuel/air mixtures (Dhamrat and Ellzey, 2006). In the case of combustion of ultra-rich fuel/air mixtures, a filtration wave propagates toward the reactor exit, i.e. heat recirculation is accomplished by "convecting" a preheated solid through the reaction zone, whereas in the case of a counter-flow burner, excess energy is recirculated between adjacent channels. Although the macroscopic heat recirculation mechanisms differ, it can be expected that the local characteristics of the combustion zones are similar. In particular, numerical models of superadiabatic filtration combustion with detailed reaction chemistry show a broadened preheating zone with an ignition temperature that is significantly higher than in adiabatic premixed combustion (Dhamrat and Ellzey, 2006). Furthermore, the results show that the primary reaction zone is thin compared to the preheating zone, which supports the assumption of a thin reaction zone used in the development of the simplified model.

In the following, model predictions are compared to well-established analytical results for flame quenching (Section 2.4.1). Furthermore, results of the co-flow case (Section 2.4.2) show that the qualitative predictions of the model correspond to results from porous burners. Results for the counter-flow case (Section 2.4.3) are obtained from the same model as the co-flow case, with the only difference being a sign change in one of the flow velocities.

2.4.1 Quenching Behavior

The special case of flame quenching is studied to relate the modeling approach to classical results in combustion literature (Spalding, 1957; Buckmaster, 1976). Buckmaster (1976) used an asymptotic expansion approach to examine the impact of heat losses to a wall on the laminar flame speed of a premixed flame. His analysis shows that the flame speed u is determined by the expression

$$u^2 \ln u = 2\mathrm{Ze}\mu \tag{2.29}$$

where $\mathrm{Ze} = \beta/\gamma$ is the Zeldovich number. In particular, Equation 2.29 illustrates that no flame solution exists beyond a critical level of wall heat losses at the quenching point. For heat losses smaller than the critical value, there are “slow" and “fast” solution branches which coincide at the quenching point (Fig. 2.5).

In the classical flame quenching mechanism, no heat recirculation occurs and thus the combustion process is equivalent to a conventional flame subject to external heat losses. In the following, it will be shown that it is possible to reproduce the flame quenching behavior with the model developed in this study. Fixing the location of the combustion front at $x = 0$ (reactor center), as well as using the limits $\kappa \to 0$

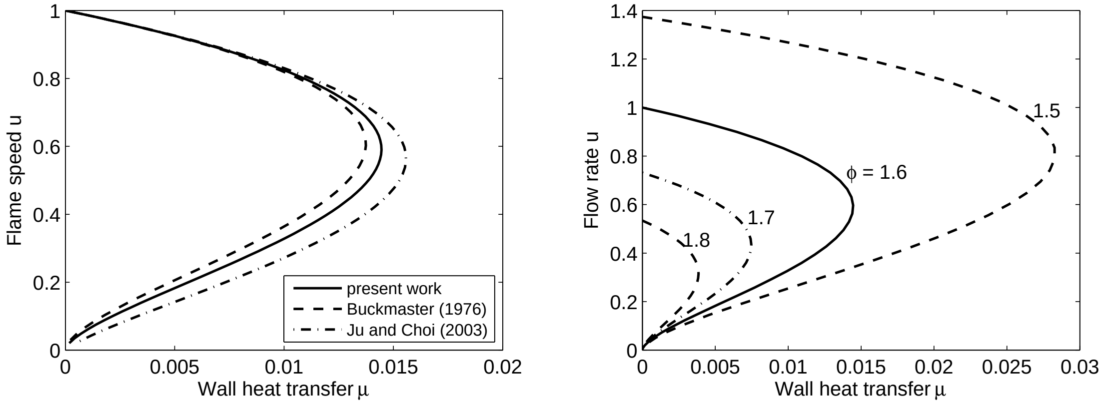

(a) **(b)**

Figure 2.5: Quenching behavior: (a) model comparison at ϕ = 1.6; (b) effect of change in equivalence ratio.

(no axial conduction) and $\epsilon \to \infty$ (long reactor) mimics the situation of combustion in infinite channels. Furthermore, by taking the limit $\chi \to \infty$ (large external heat losses), the wall temperature becomes identical to the temperature of the environment. By consequence, there is no interaction between the reactor channels, and flame quenching can be studied independent of the flow directions within the individual channels.

Figure 2.5a shows the flame speed as a function of heat losses for three different models. It illustrates that results from the heat-exchanger model obtained from a numerical limiting process (this study) closely match Eq. 2.29, representing the classical quenching curve developed by Buckmaster (1976). However, Figure 2.5a also illustrates the importance of the formulation of the jump equation representing the combustion process. An approximation commonly used in literature (Maruta et al., 2005; Fursenko et al., 2001; Ju and Choi, 2003) assumes that the peak temperature of the combustion zone remains close to the adiabatic flame temperature, i.e. $T_c/T_{\mathrm{ad}} \approx 1$. This assumption, however, results in a less accurate approximation.

Figure 2.5b shows graphs of flow rate versus heat loss for different rich equivalence ratios, where an increase in the equivalence ratios beyond the conventional flammability limit results in a drop of flow velocity as well as an increased suscepti-

Configuration	(A) Co-Flow	(B) Counter-Flow
Equivalence ratio ϕ	1.6	2.0
Inlet temperature T_0	0.1625[a]	0.1625
Ambient temperature T_∞	0.1625	0.1625
Non.-dim. channel width a	0.25	0.08333
Non.-dim. wall thickness b	0.04	0.01333
Nusselt Number Nu	5	5
Ext. Nusselt number Nu_∞	0.25	0.25
Peclet Number Pe	3.78944	3.78944
Conductivity ratio k	0.00383	0.00383
Emissivity ε	0.8	0.8
Heat transfer factor μ	0.34819	0.34819
Conductivity factor κ	20.9003	20.9003
Geometry factor ϵ	0.06597	0.02199
Wall heat loss factor χ	0.025	0.025
Radiative heat loss σ	0.40483	1.2145

---

[a] corresponds to 298 [K] .

Table 2.2: Parameter values used for base cases in co- and counter-flow configuration.

bility for quenching. As the case $\phi = 1.7$ represents the conventional rich flammability limit, the cases $\phi = 1.4$ and 1.6 lie within the flammable range, whereas the case $\phi = 1.8$ is subject to quenching in practical burners.

2.4.2 Co-flow Configuration

Assuming equal flow rates and directions at the channel inlets, the gas temperature distribution in the individual channels is identical. Thus, the reaction zone locations coincide and the solution consists of two segments upstream and downstream of the reaction front. By consequence, the solution is equivalent to combustion in straight channels or porous inert media. In the following, results are discussed based on the parameter values given for configuration A in Table 2.2, which corresponds to a co-flow reactor with channel dimensions of 50.8×6.35 mm with moderate axial conduction and interfacial heat transfer.

Figure 2.6 illustrates typical results for a burner in co-flow configuration at

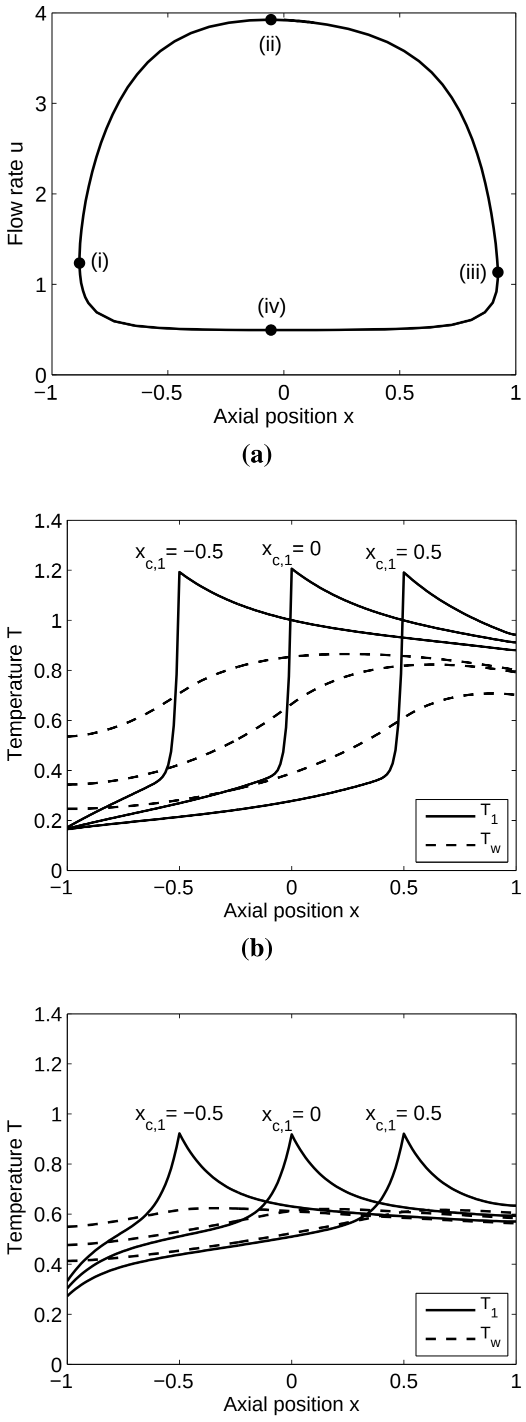

(a)

(b)

(c)

Figure 2.6: Position of the combustion zone in co-flow configuration at $\phi = 1.6$: (a) flow rate as function of axial position; (b/c) temperature profiles for fast/slow solutions at specified locations.

$\phi = 1.6$. In Figure 2.6a, the flow rate is plotted over the axial location of the combustion zone, where $x = -1$ and $x = 1$ correspond to channel inlet and outlet, respectively. Outside the region marked by points (*i*) and (*iii*) no solutions exist, which means that a combustion zone cannot be established close to the inlet and outlet face of the reactor. In the region between (*i*) and (*iii*) solutions for stationary combustion zones exist at two separate flow rates, which represent fast and slow solution branches. Examples for temperature profiles of fast and slow solutions are illustrated in Figures 2.6b and 2.6c, where the flow rates are solved at specified locations of the combustion zone. As will be shown, the possible ranges of flow rates and combustion zone locations are highly dependent on the model parameters. For the particular choice of parameters illustrated in Figure 2.6, the slow solution shows subadiabatic behavior, whereas the fast branch operates under superadiabatic conditions. Experimental results from porous two-section burners (Vogel and Ellzey, 2005) show that both fast and slow conditions can be established in a practical burner, where either stable or oscillating operation has been observed. Oscillatory operation has also been reported for combustion in narrow heated quartz tubes (Maruta et al., 2004).

While Figure 2.6a represents stationary solutions, it can be used indirectly to get an indication of stable and unstable combustion zone locations by examining small perturbations from the steady-state solution (Spalding, 1957). For solutions represented by segments with positive slopes ($du/dx > 0$), a perturbation of the combustion zone location in the downstream direction results in an increased burning rate, whereas a perturbation upstream yields a decreased reaction rate. In both cases, the combustion zone is pulled towards the original location, which establishes a self-stabilizing process. Using a similar argument, it can be shown that segments with negative slope ($du/dx < 0$) represent unstable solutions. Thus, stable solutions of the fast branch exist close to the burner inlet (segment $(i)-(ii)$), whereas stable solutions of the slow branch can be established close to the exit face of the reactor (segment $(iii)-(iv)$). The remaining solutions are either unstable or oscillatory unstable, as has been shown by Maruta, et.

al. (2004), who used an analytical analysis of small perturbations of a steady state solution to assess the stability of combustion in heated tubes.

In the following, the impact of different model parameters is discussed based on the reference case (Fig. 2.6). Figures 2.7 and 2.8 show the results for variations of a single parameters while the remaining parameters are held constant. Both equivalence ratio ϕ and inlet temperature T_0 have a large impact on attainable flow rates and characteristics of the solution (Fig. 2.7a/b), such as the existence of solutions at the inlet and outlet of the burner channels ($x = \pm 1$). Varying the equivalence ratio reveals solutions at the burner inlet and exit only for $\phi = 1.4$ (Fig. 2.7a). Similarly, an increase in inlet temperature also produces solutions at the burner inlet and exit (Fig. 2.7b).

Figures 2.7c and 2.7d show the influence of axial conduction and gas-to-solid heat transfer parameter on the performance of the burner. For low axial conductivities ($\kappa \to 0$) or low intensities of interfacial heat transfer ($\mu \to 0$), the superadiabatic performance deteriorates. In particular, at $\kappa = 0.209$ as well as $\mu = 0.00696$, the fast solution for the flow rate is close to unity and thus equal to the value predicted by an adiabatic combustion process at $\phi = 1.6$. On the other hand, large values of κ and μ result in flow rates that are higher than the adiabatic flow rate for both fast and slow solution branches. As superadiabatic performance hinges on both κ and μ, heat recirculation by axial conduction can be identified as the principal mechanism responsible for superadiabatic combustion in co-flow configuration.

The geometry factor ϵ is inversely proportional to the reactor length. Figure 2.8a illustrates that the gradient du/dx in the central part of the channel flattens for increasing burner lengths. Thus a slight change in the velocity results in drifts of the combustion zone location (Schoegl et al., 2004). While the maximum flow rate remains approximately constant as the channel length is increased, it drops significantly as the channels become shorter. The different behavior of thin and thick burners has been reported earlier (Mathis and Ellzey, 2003), where thin burners operate close to the laminar flame speed (Mital et al., 1997), whereas thick burners operate at considerably

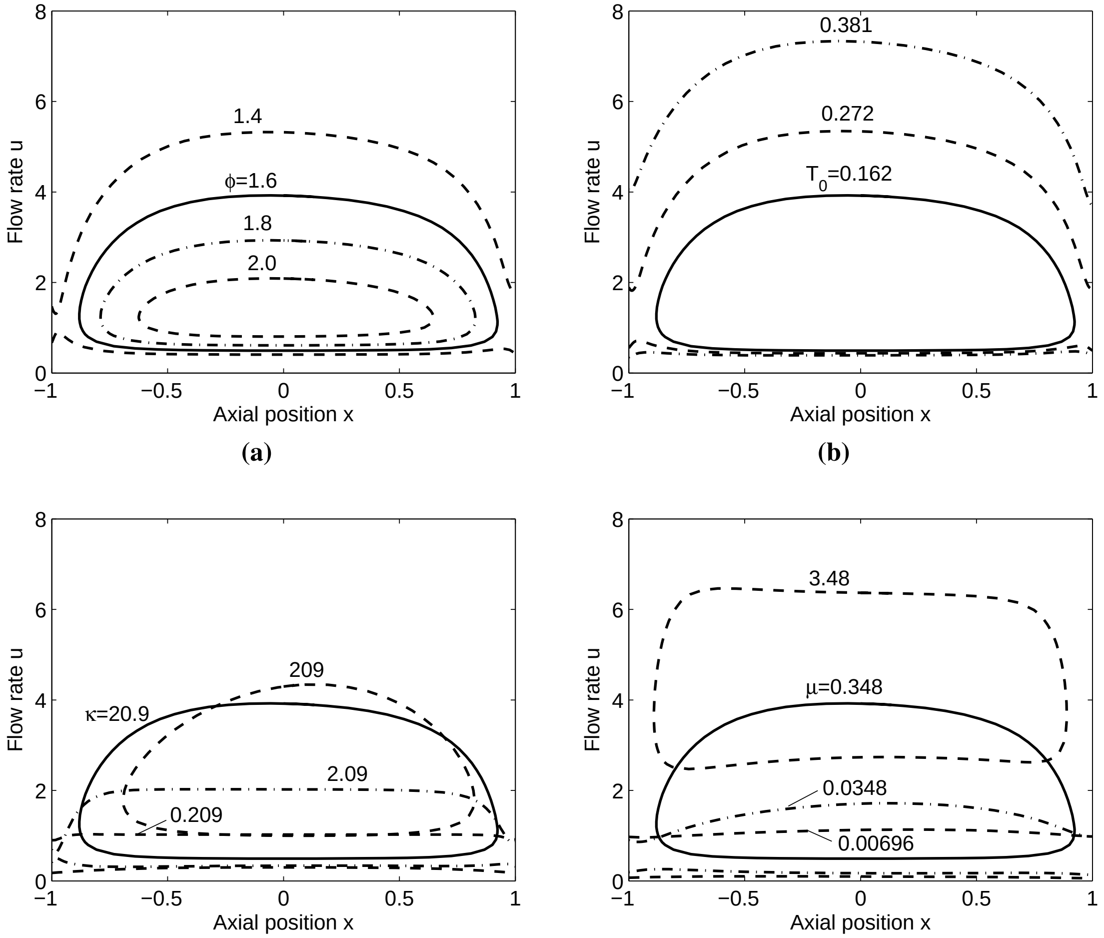

(a) (b) (c) (d)

Figure 2.7: Impact of model parameters on combustion characteristics in co-flow configuration: variation of (a) equivalence ratio ϕ; (b) inlet temperature T_0; (c) axial conduction parameter κ; (d) gas/wall heat transfer parameter μ. Solid lines correspond to the reference case (Fig. 2.6a).

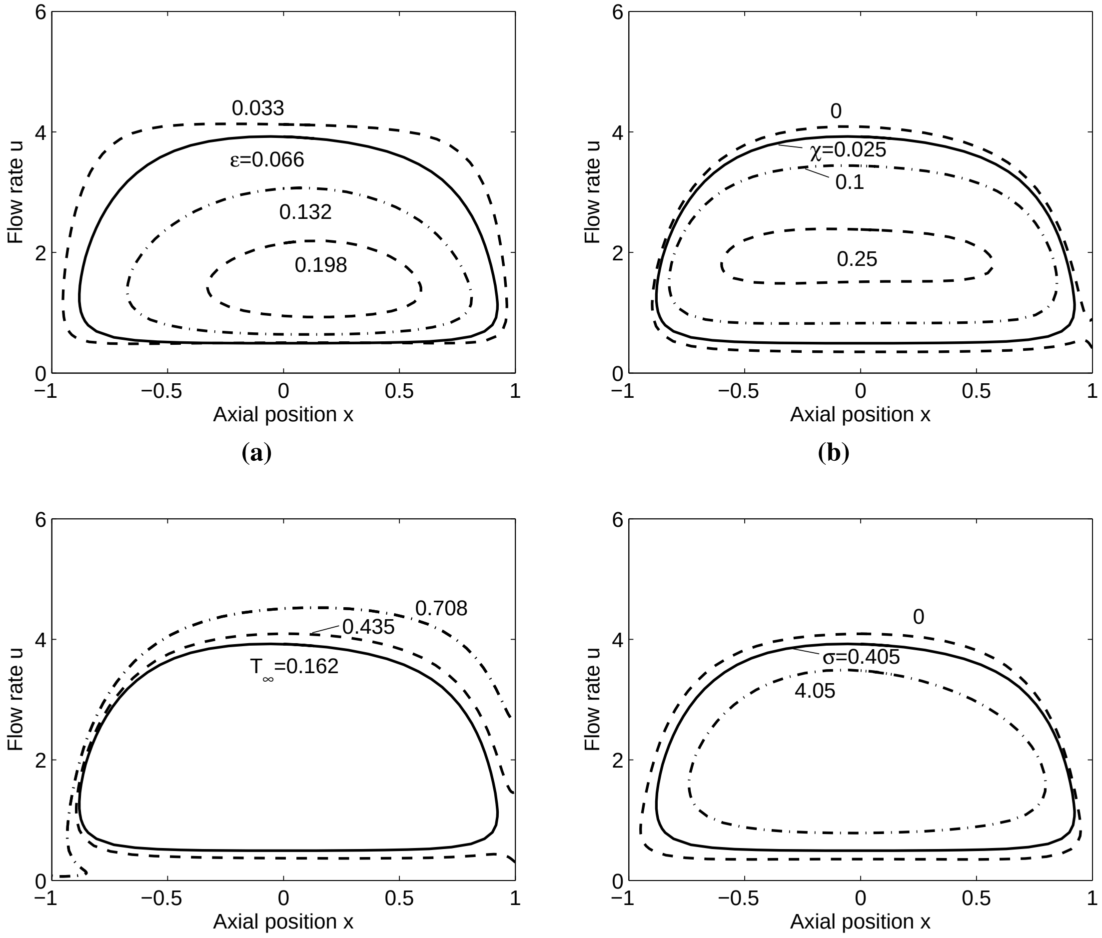

(a) (b)

(c) (d)

Figure 2.8: Impact of model parameters on combustion characteristics in co-flow configuration: variation of (a) reactor geometry ϵ; (b) external heat loss factor χ; (c) temperature of the environment T_∞; (d) radiative heat losses from reactor faces σ. Solid lines correspond to the reference case (Fig. 2.6a).

larger inlet velocities (Khanna et al., 1994).

The remaining variations illustrate the relevance of different heat losses (Figs. 2.8b-d). Figure 2.8b shows the influence of heat losses from the wall (parameter χ). It can be seen that the performance does not deteriorate significantly for moderate heat losses, while large heat losses result in a marked degradation of peak flow rates. External heat losses are also influenced by the temperature of the environment T_∞, which is illustrated in Figure 2.8c. A comparison of different external temperatures shows a moderate influence on the peak flow rates in the burner. The case of elevated external temperatures has been studied by Maruta, et al. (2005), who imposed a generic wall temperature profile to emulate the conditions in a heated channel. In their findings, they reported an "extraordinary" combustion mode at elevated ambient temperatures, where the flow rate lies below the regular slow and fast branches of the solution. This behavior is also present in Figure 2.8c at $T_\infty = 0.708$, where three separate solutions exist at certain positions close to the channel inlet.

The impact of radiative heat losses from reactor faces (parameter σ) is illustrated in Figure 2.8d, which shows a moderate influence on the performance of a burner with moderate channel length. A large value of σ represents the case of radiant combustors, which has been previously investigated by McIntosh and Prothero (1991), who developed an analytical solution for thin radiant burners. While their findings show that radiative heat losses have a significant impact on the burner operation, these results are still consistent with the results of the present model, since thin burners operate at lower speeds and temperatures, and thus are more susceptible to heat losses.

2.4.3 Counter-flow Configuration

Assuming equal flow rates with opposite flow directions (i.e. $u_1 = -u_2$), the temperature distribution in channel 1 becomes a mirror image of the temperature distribution in channel 2, i.e. $T_2(x) = T_1(-x)$. Moreover, a combustion zone at $x = x_c$ in channel 1 implies a combustion zone at $x = -x_c$ in channel 2. In the following, the counter-flow

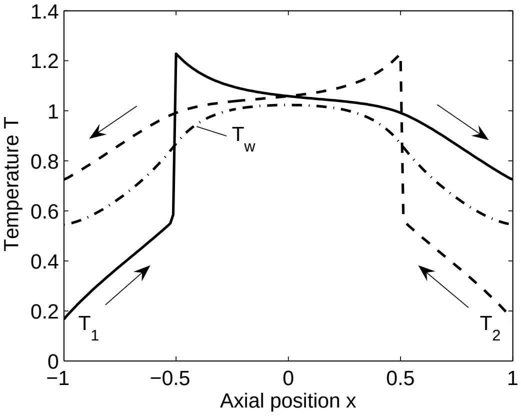

Figure 2.9: Temperature profiles for channels in counter-flow configuration at $\phi = 2.0$.

concept is discussed based on the parameter values given for configuration B in Table 2.2, which corresponds to a reactor with channel dimensions of 152.4×6.35 mm with moderate axial conduction and interfacial heat transfer.

Figure 2.9 shows a typical solution of the counter-flow case outside the conventional flammability limits of methane/air mixtures ($\phi = 2$), where the gases in channels 1 and 2 flow in the positive and negative x-direction, respectively. In channel 1, the unburned fuel/air mixture enters the burner and is heated by the combustion products in the adjacent channel until the gas temperature is sufficiently high to support a self-sustained reaction zone. In the center of the burner, the temperature gradient flattens and high temperatures are maintained until the gas passes the location of the reaction zone in channel 2. As the gases in channel 2 are flowing in the opposite direction, they undergo the same process, which forms a loop of heat recirculation between the channels.

The principal difference between the analytical model presented in this paper and previous studies on combustion in channels with opposed flow directions (Fursenko et al., 2001; Ju and Choi, 2003; Fursenko and Minaev, 2005) lies in the fact that earlier models used infinite channels combined with the assumption of large external heat losses instead of a finite channel length. As can be seen in Figure 2.9, the temperature profiles in the channel sections between reactor faces and the reaction zones reveal the classical behavior of a balanced counter-flow heat exchanger. In the case of infinite channels, however, heat transfer between the adjacent channels reduces the temperature difference to zero away from the combustion zone. Since the temperatures at the channel outlets match the inlet temperatures, external heat losses become the only mode of heat dissipation.

The most important aspect of combustion in two channels with opposing gas flows is counter-flow heat exchange. In order to further illuminate the differences between the present model and previous models, it is necessary to examine the limiting case of vanishing external heat losses ($\chi = 0$). For this case, the characteristic polynomial of the governing equations (Eq. 2.19) produces a double eigenvalue at zero, which results in an analytical solution different from Equation 2.20. Instead of having a solution consisting of the weighted sum of six exponential functions, the solution for the limiting case is formed as the superposition of a linear equation and four exponential functions, which decay rapidly and only affect the solution at the boundaries of the solution domains. The characteristics of this solution, however, cannot be consolidated with the requirement of finite temperatures at the reaction zone under the assumption of infinite channel length, since it would result in the loss of the counter-flow heat exchange mechanism. Thus, models based on infinite channels cannot be used for the case of small external heat losses, because they are not capable of reproducing the behavior of the limiting process $\chi \to 0$ correctly, where they predict an infinitely large separation distance between the individual combustion zones (Ju and Choi, 2003).

In Figure 2.10a, the flow rate is plotted over the axial position of the combustion zones in channel 1 for an equivalence ratio $\phi = 2.0$, where the reaction zones locations are determined by the counter-flow heat exchange mechanims. When compared to Figure 2.6a, which illustrates the co-flow configuration at $\phi = 1.6$, this shows that the flow velocities in the counter-flow burner are significantly higher, even though they are calculated for a fuel/air mixture with lower energy content. The results show that a minimum distance between channel inlet and reaction zone is required to preheat the

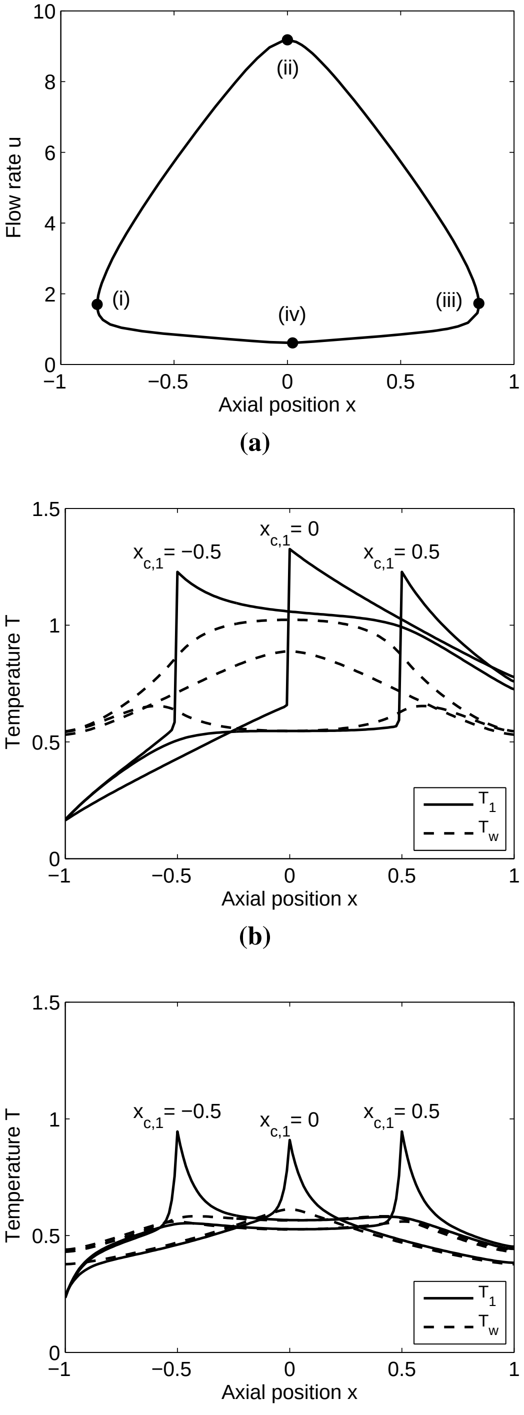

(a)

(b)

(c)

Figure 2.10: Position of the combustion zone in channel 1 for counter-flow configuration at ϕ = 2.0: (a) flow rate as function of axial position; (b/c) temperature profiles for fast/slow solutions at specified locations.

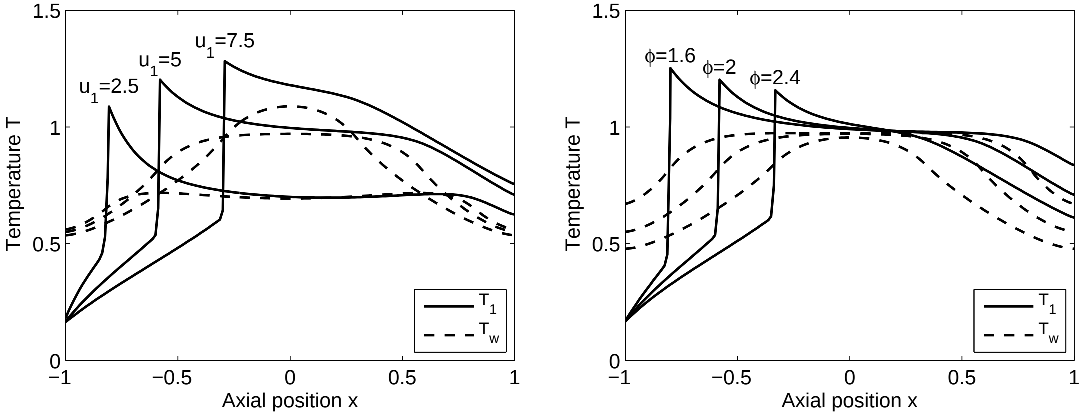

(a) **(b)**

Figure 2.11: Stabilization of the combustion zone in counter-flow configuration: (a) increasing flow rate at $\phi = 2$; (b) increasing equivalence ratio at $u_1 = 5$.

unburned mixture to a level where the gases are hot enough to react (point (*i*)). The reaction location moves towards the center of the combustor for feed rates both higher and lower than the one that corresponds to this minimum distance. It can also be seen that it is not possible to stabilize a reaction zone below a minimum flow rate (*iv*) and above a maximum flow rate (*ii*), which is consistent with early results on swiss-roll combustors based on a global energy balance of a heat-recirculating burner (Jones et al., 1978).

Similar to the co-flow case, counter-flow burners can support combustion zones for two different flow velocities at the same position, which establishes fast and slow solution branches, respectively. Examples of temperature profiles for fast and slow solutions at specified locations are illustrated in Figures 2.10b and 2.10c. In contrast to the co-flow case, however, it is not possible to assess the stability of individual solutions based on the slope $du/d\text{x}$ in Figure 2.10a. In the counter-flow case, Fursenko and Minaev (2005) showed that segments with $du/dx < 0$ may be stable and thus the stability of an individual solution can only be assessed based on an analysis of small perturbations from the steady-state conditions.

Figure 2.11 illustrates the flame stabilization mechanism in regions with $du/dx >$

0 (fast branch), where an increase in the flow rate moves the combustion zone closer to the mid-point of the heat exchanger, which increases the peak temperature and thus accelerates the reactions (Fig. 2.11a). In a similar process, an increase of the equivalence ratio at constant flow rate produces reaction fronts closer to the reactor center (Fig. 2.11b). Due to this mechanism, counter-flow burners are capable of supporting combustion zones at large inlet velocities even for air/fuel mixtures that lie outside of the conventional flammability limits.

Similar to the co-flow case, the influence of individual model parameters on the burner characteristics is investigated based on parameter variations (Figs. 2.12 and 2.13). Figure 2.12a illustrates that the counter-flow concept is able to stabilize combustion for a wide range of equivalence ratios. It can be seen that the minimum flow rate increases as the energy content of the fuel/air mixture decreases, which agrees with experimental results from small swiss-roll burners (Kim et al., 2005). Similar to the co-flow case, an increase in the inlet temperature results in a widening of the possible operating range of the burner (Fig. 2.12b).

For the particular parameter combination chosen for the reference case, axial conduction (Fig. 2.12c) has only a secondary impact on the burner performance, which indicates that the heat transfer across the dividing wall, rather than along the wall, is the primary process responsible for heat recirculation within the burner. Only for cases with high axial conductivities ($\kappa = 209$) the characteristics of the solution are changed, which justifies the thin wall approximation for cases with moderate axial conduction (Ju and Choi, 2003). By contrast, the burner behavior is extremely sensitive to both gas-to-solid heat transfer (Fig. 2.12b) and reactor geometry (Fig. 2.13a), which underscores the significance of the counter-flow heat exchange. In particular, moderate increases of either heat transfer coefficient or reactor length result in a dramatic increases of the supported flow rates.

Similar to the co-flow case, only large heat losses from the wall change the characteristics of the combustion process significantly (Fig. 2.13b), where the su-

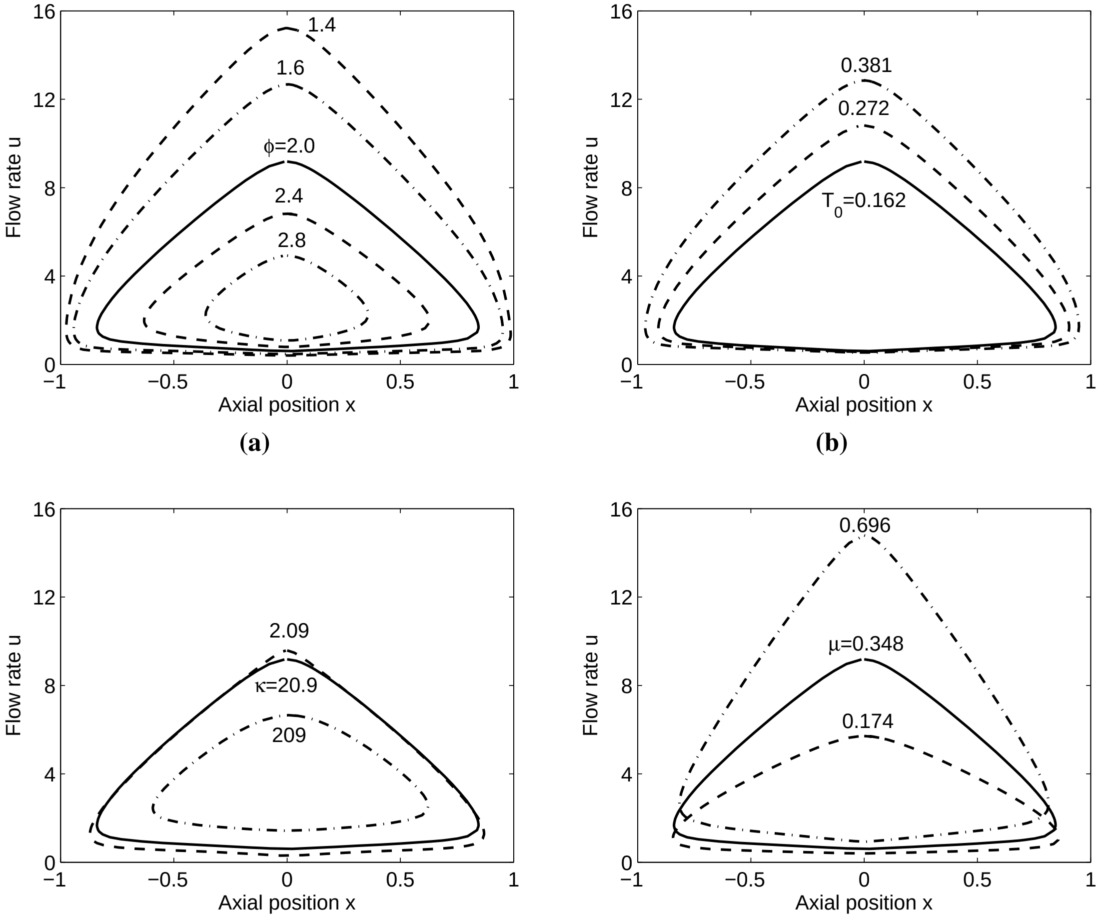

(a) (b) (c) (d)

Figure 2.12: Impact of model parameters on combustion characteristics in counter-flow configuration: variation of (a) equivalence ratio ϕ; (b) inlet temperature T_0; (c) axial conduction parameter κ; (d) gas/wall heat transfer parameter μ. Solid lines correspond to the reference case (Fig. 2.10a).

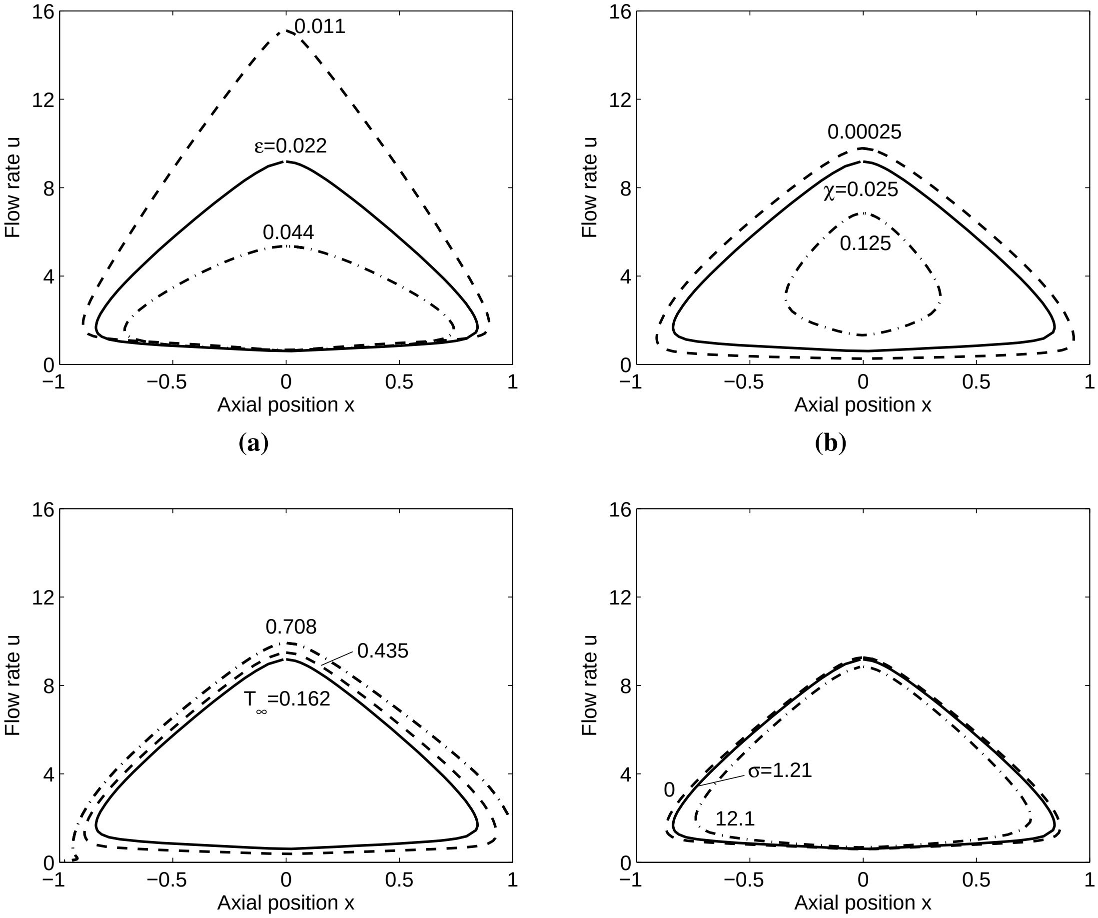

(a) **(b)**

(c) **(d)**

Figure 2.13: Impact of model parameters on combustion characteristics in counter-flow configuration: variation of (a) reactor geometry ϵ; (b) external heat loss factor χ; (c) temperature of the environment T_∞; (d) radiative heat losses from reactor faces σ. Solid lines correspond to the reference case (Fig. 2.10a).

peradiabatic performance degrades for large external heat losses. Neither the ambient temperature (Fig. 2.13c) nor radiative heat losses from the reactor ends (Fig. 2.13d) show a major influence on the peak flow rate, which can be explained by moderate heat losses and low wall temperatures at the reactor ends, respectively.

2.5 Summary

The most important feature of superadiabatic combustion is the possibility of combusting fuel/air mixtures outside the conventional flammability limits due to the presence of local high temperature zones. In contrast to superadiabatic filtration waves, which travel toward the reactor exit, the concepts presented in this study are based on energy concentration in heat exchangers. It has been demonstrated that temperatures above the adiabatic temperature are possible for stationary fronts. Based on a simplified analytical model, burner operation with equal flows in co-flow and counter-flow configuration was studied in order to illuminate the dominant model parameters responsible for superadiabatic performance. A variation of the model parameters shows that the principal parameters in co-flow configuration are axial conductivity and interfacial heat transfer, whereas the predominant parameters in the counter-flow case are reactor length and interfacial heat transfer. These results are intuitive, since they identify the dominant heat transfer processes as axial conduction for the co-flow case and heat exchange across the wall for the counter-flow case.

A comparison of the burner performance in co-flow and counter-flow configuration illustrates that the counter-flow concept is superior in terms of superadiabatic operation. The results of this study demonstrate that counter-flow burners can operate under conditions that lie outside the conventional flammability limits as well as at velocities that are significantly higher than the laminar flame speed. In each channel, the location of the combustion zone is determined by counter-flow heat exchange between the unburned fuel/air mixture and the combustion products in the adjacent channel. This mechanism anchors the combustion zone in a self-stabilizing process for a large range of flow velocities at a particular equivalence ratio, which results in a large turn-down ratio of the burner design.

Chapter 3

Experimental Results

The objective of the experimental investigations was to verify the viability of fuel reforming in a non-catalytic reactor based on combustion with counter-flow heat exchange. Several fuel reformer prototypes were built, tested for varying inlet velocities and equivalence ratios, and evaluated in terms of operating range and conversion efficiency. Based on first experimental results from a prototype with two adjacent flow channels in counter-flow configuration, the reactor was redesigned in order to improve the performance. The final design consisted of four channels with alternating flow directions, and was extensively tested for both methane and propane fuel (Schoegl and Ellzey, 2009; Schoegl et al., 2009).

The primary result of the experimental work is that combustion can be established in stationary reaction zones at conditions that are favorable for fuel reforming, i.e. at equivalence ratios beyond 2.0. In addition, experimental observations of temperature profiles along the channels confirmed the viability of reaction front stabilization by cross-wall heat transfer, as predicted by the analytical model outlined in Chapter 2. While experiments with methane/air mixtures focused on showing the feasibility of non-catalytic fuel reforming in stationary combustion zones, experiments with propane/air mixtures were conducted to show the fuel flexibility of the reformer concept. Propane is a fuel that is more similar to standard transportation fuels, and experiments were

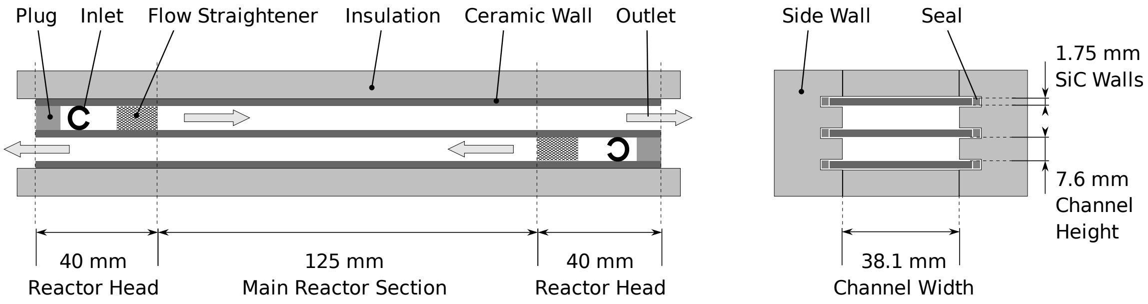

(a) stream-wise direction. **(b)** cross-stream direction.

Figure 3.1: Cross-sections of reactor prototype with two channels in counter-flow configuration.

designed to get a more detailed understanding of the fuel break-down during the reforming process.

3.1 Initial Tests with Two-Channel Reactor Prototype

3.1.1 Design Process

The initial test of the reactor design was performed using a prototype with 14 flow channels. The prototype used 0.25 mm thick stainless steel sheets (Type 316) as channel walls. The lateral channel confinements were constructed from alumina beads that acted as spacers, creating a channel height of 3.25 mm. The entire assembly was sealed and held in place using high-temperature adhesive (Cotronics Corp.; Brooklyn NY). Tests of the reactor prototype, however, failed due to differences in the thermal expansion coefficients of alumina beads and steel sheets resulted in warped channel walls that did not seal adjacent channels from each other. In addition, the relatively low melting point of stainless steel 316 (1375-1400°C) motivated a change of wall materials, and ceramics were used in all subsequent tests.

The reactor design used for the first operational fuel reformer prototype is illustrated in Figure 3.1. The flow channels are housed in slabs of alumina insulation, where ceramic tiles form internal divisions between adjacent flow channels. In order

Table 3.1: Revisions of reactor prototypes with two flow channels: wall materials and porous media.

Revision	Wall Material	Porous Media	Channel Height	Wall Thickness	Notes
1	Alumina	SiC	8.0	1.25	Cracked walls
2	Alumina	N/A	8.0	1.25	Cracked walls
3	SiC	N/A	7.5	1.75	Cracked walls
4	SiC	N/A	7.5	1.75	Success

to separate inlets and outlets, one end of each channel is blocked (Fig. 3.1a). At each blocked end, the cold reactants enter through ducts drilled through the side walls, and a section of Silicon Carbide (SiC) porous media (7.9 pores per centimeter, 90% porosity – Ultramet; Pacoima, CA) acts as a flow straightener to condition the flow. Chemical reactions occur in the main reactor section, and reaction products exit at the unblocked ends of each channel (Fig. 3.1a). The internal wall tiles are held by grooves cut into the side walls, where a seal made from alumina paper prevents gas leaks between adjacent channels (Fig. 3.1b). While the construction of the heat exchanger differs significantly, the configuration of inlets and outlets is similar to a design for a ceramic heat exchanger built from honeycomb media (Minjolle, 1981).

While the basic configuration was maintained, several revisions with different wall materials were tested (Table 3.1). The initial two prototypes used 205mm × 50mm × 1mm Alumina wall tiles, which were cut from 165 × 185 × 1.25 mm Alumina samples (CoorsTek; Golden, CO) using a diamond blade on a surface grinder. Instead of flow straighteners, the entire main reactor section of the first prototype was filled with slabs of porous SiC media (Ultramet; Pocoima, CA) to enhance the heat transfer between the adjacent channels (Boomsma et al., 2003). Tests both with and without the porous matrix, however, showed that Alumina walls could not withstand the large temperature gradients during the initial light-up process, resulting in wall failures within less than a minute of operation. After unsuccessful tests with Alumina tiles, additional tests were conducted with Silicon Carbide tiles (Saint-Gobain Ceramics; Niagara Falls,

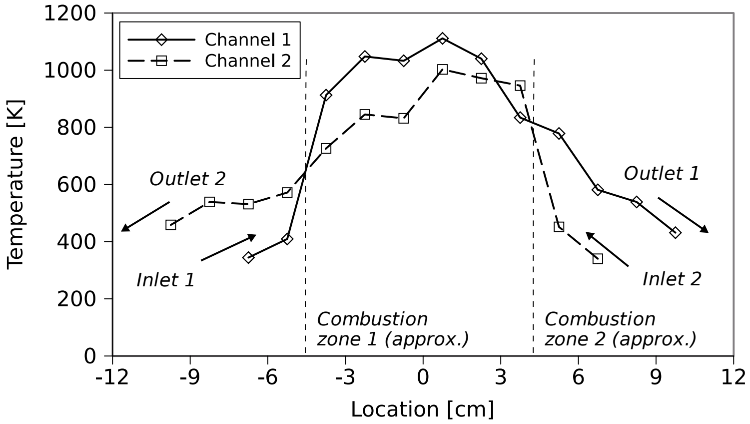

Figure 3.2: Temperature profile in 2-channel reactor at equivalence ratio 1.95 and inlet velocity 104.1 cm/s.

NY). The availability of thin SiC tiles was, however, limited to the dimension 50 × 50 × 1.25 mm and 100 × 100 × 1.75 mm. Thus, walls were constructed from two segments cut from the latter material, sized 100 × 50 × 1.75 mm, and pushed together at the channel center. The first prototype with SiC walls still failed due to the collapse of the central channel, which was attributed to insufficient tolerances resulting in excessive mechanical stresses within the reactor. A subsequent rebuild with wall tiles that were cushioned with alumina paper seals resulted in an operational prototype.

3.1.2 Concept Verification and Initial Results

Figure 3.2 shows typical temperature profiles observed during operation of the two-channel reactor. The solid curve shows the temperatures along channel 1 where the flow direction is from left to right (solid curve), and along channel 2 where the flow direction is from right to left (dashed curve). In both cases, the first temperature sensor was positioned upstream of the flame arrester to detect flash-back of the combustion zone through the flame arrester at the channel entrance. The remaining probes were exposed to temperatures in the main reactor section.

The temperature profiles illustrated in Figure 3.2 were taken at an equivalence ratio of 1.95 and an inlet velocity of 104.1 cm/s. At ϕ=1.95, the reactor operates beyond the conventional flammability limit of a rich methane/air mixture, which lies at ϕ=1.7 (Glassman, 1996). Also, the velocity is significantly higher than typical laminar flame speeds of methane/air mixtures, which further illustrates the effectiveness of heat recirculation. In particular, Figure 3.2 shows that the channel temperatures increase slightly at the channel inlets, where heat is transferred by counter-flow heat exchange from the hot combustion products in the adjacent channel. Continuing downstream, channel temperatures increase sharply between the second and third sensor, indicating the presence of combustion zones at approximately −4.5 and +4.5 cm.

With two distinct combustion zones, the reactor can be partitioned into an interior high temperature zone and two exterior zones, where counter-flow heat exchange is used to preheat the unreacted fuel/air mixtures to a level where self-sustained combustion is viable. The same behavior is predicted by the simplified analytical model of the process (Chapter 2). Taken together, results indicate that the combustion zone is stabilized by heat transfer across the wall, which is also shown in detailed numerical results (Chapter 4). As this stabilization mechanism does not require flame holders, the locations of the combustion zones adjust to independent changes in flow velocities and stoichiometry.

Figure 3.3 illustrates the operating range of the two-channel reactor in terms of equivalence ratio and inlet velocity. The focus of the experiments was the determination of limits beyond which combustion inside the channels was impossible. As shown in Figure 3.3, combustion of increasingly rich mixtures occurred as the flow velocity was decreased. While rich combustion beyond an equivalence ratio of 2.5 was observed at flow velocities below 50 cm/s, the combustion fronts were not stationary. At equivalence ratios smaller than 2.25, however, the results show a large turn-down ratio between highest possible flow rate and lowest possible flow rate, which is important for practical applications.

At low velocities, a comparison of the temperature profiles of the two flow

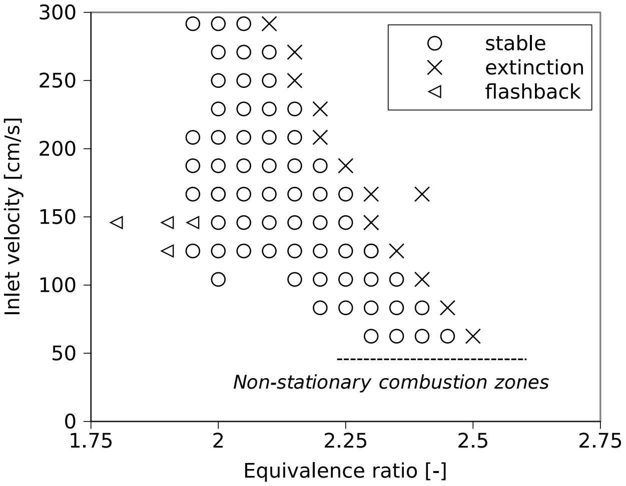

Figure 3.3: Operating range of 2-channel reactor.

channels revealed shortcomings of the reactor design. In theory, the temperature profiles in the two channels should be anti-symmetric, i.e. $T_1(x) = T_2(-x)$. In the experimental setup, channels were stacked on top of each other, where channel 1 was located below channel 2 (Fig. 3.1). Measurements showed that temperatures in channel 1 were consistently higher than the ones in channel 2, which can be explained by disparate heat losses from the exterior walls of the reactor. At low burning rates, where heat losses are proportionally more significant, this resulted in combustion locations that were not symmetric around the reactor center.

After finishing the experiments, the reactor was disassembled and the parts were inspected. Figure 3.4 shows photographs of walls after being removed from the reactor prototype. While the SiC tiles used for the wall separating the two flow channels remained intact, SiC tiles forming the exterior walls of the flow channels showed cracks, which may have further contributed to the asymmetric behavior discussed above. In addition, the surface of SiC tiles that were exposed to high temperatures revealed discoloring similar to annealing colors of steel. To determine the cause of the discoloring, the surface was investigated using X-ray spectroscopy. This did not reveal conclusive information on deposits due to an insufficient thickness of the surface layer. Yet, the

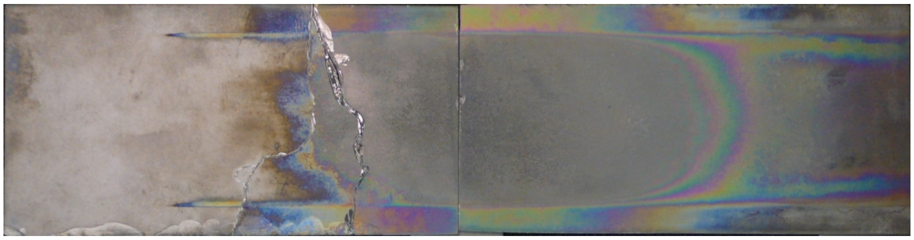

(a) Top channel (Flow direction left-to-right): bottom view of exterior wall.

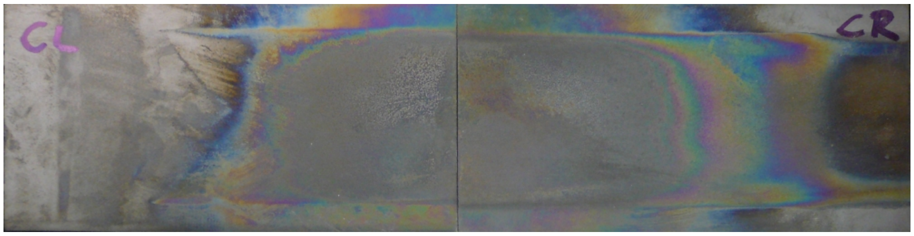

(b) Top channel (Flow direction left-to-right): top view of dividing wall.

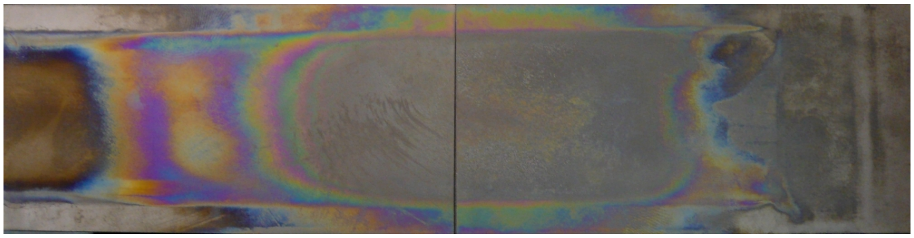

(c) Bottom channel (Flow direction right-to-left): bottom view of dividing wall.

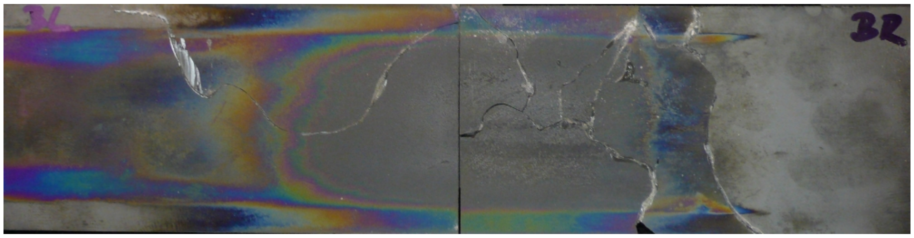

(d) Bottom channel (Flow direction right-to-left): top view of exterior wall.

Figure 3.4: Photographs of SiC tiles removed from two-channel prototype upon completion of the tests. Top and bottom of each tile show discoloring where tiles were inserted in grooves in the side walls (Fig. 3.1b). Broken tiles in (a) and (d) are reassembled.

Table 3.2: Dimensions of two-channel and four-channel reformer prototypes (in mm).

	2-channel design	4-channel design
Length of main section	125.0	91.5
Total length	205.0	183.0
Channel height	7.6	4.0
Channel width	38.1	33.6
Wall thickness	1.75	1.0

color patterns exposed by this surface layer can be used to identify different temperature zones within the channels, which reveal valuable information for a redesign of the fuel reformer inlet section for the four-channel design.

3.1.3 Redesign of the Fuel Reformer

Upon completion of initial tests with the two-channel prototype, the fuel reformer was redesigned. In order to decrease the impact of external heat losses, the number of channels was increased from two to four. An additional motivation for the redesign was to demonstrate the feasibility of fuel reforming in a compact reactor design, leading to an overall reduction of the channel dimensions, listed in Table 3.2.

A close inspection of color patterns on the dividing wall tiles used for tests with the two-channel reformer shows imperfect flow conditions downstream of the flow straighteners. Flow patterns in the center of the left tile in Fig. 3.4b and right tiles in Fig. 3.4c indicate that the flow velocity is larger in the corners formed by flow straighteners and lateral walls. In order to generate more uniform flow conditions, the inlet section was redesigned, where a second flow straightener was placed in each channel (Fig. 3.5).

Photographs of external wall tiles show cracks across the width downstream of the flow straightener, shown in the left half of Fig. 3.4a and the right half of Fig. 3.4d, respectively. As external tiles are not heated by adjacent flow channels, temperature gradients are expected to be higher than those experienced by interior walls. Thus,

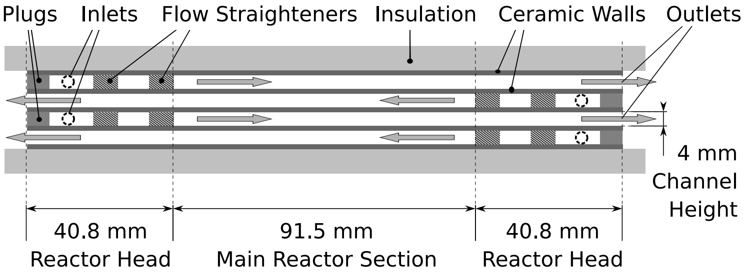

Figure 3.5: Fuel reformer based on counter-flow heat exchange between channels with opposing flow directions.

Table 3.3: Revisions of reactor prototypes with four flow channels: wall materials and tile patterns.

Revision	Tile pattern (numbers in parentheses are tile lengths in mm)	Wall Thickness
1/2	SiC(40.8) – SiC(40.8) – SiC(40.8) – SiC(40.8)	1.25
3	Alumina(40.8) – SiC(40.8) – SiC(40.8) – Alumina(40.8)	1.25
4/5/6	SiC(40.8) – SiC(91.5) – SiC(40.8)	1.25/1.75
7/8/9	SiC(40.8) – SiC(91.5) – SiC(40.8)	1.0

instead of using two wall tiles meeting at the center as in the two-channel design, walls for the four-channel design were sectioned according to the reactor parts. Walls of the main reactor section were constructed by either two 40.8 mm tiles or a single 91.5 mm tile, and two 40.8 mm tiles were used for the reactor heads containing inlets and outlets.

In order to guarantee long-term stability of the redesigned reactor, nine prototypes of the four-channel design were built and tested (Table 3.3). The first two revisions used four 40.8mm long and 1.25 mm thick SiC tiles, and the third revision used 1.25 mm thick Alumina tiles in the outermost positions. Again, tests showed that mechanical stresses due to imperfect alignment of parts during the assembly resulted in wall failures, which was exacerbated by the necessity to align four wall segments. Also, Alumina was ruled out as wall material due to its inferior performance. The next three revisions used 91.5 mm long tiles for the main reactor section, where tiles used in the interior were surface ground with a diamond wheel to 1.25 mm thickness, and

1.75 mm thick tiles formed the external walls. The third test of this series (revision 6) was successful, but showed problems with deposits that are detailed below. In order to obtain thin walls for efficient heat transfer, walls of the final three prototypes were ground to a thickness of 1 mm, where all walls were built with identical tile patterns. Out of the prototype series, revisions 6, 7 and 9 were used in successful tests, and revision 9 was used for extensive experimental work.

During prolonged tests close to the rich operating limits, silver-colored deposits were observed on channel walls, shown in Figure 3.6. During initial tests it was noted that if allowed to grow, deposits could peel off the walls and obstruct the channels. Further investigation using X-ray diffraction (XRD) identified the deposits as pyrolytic graphite (Yajima et al., 1965). The carbon deposits were, however, removed effectively by occasionally interrupting the fuel supply and purging the hot reactor with pure air for 10 to 20 seconds, after which the experiment was continued. The SiC wall tiles proved to be extremely stable at normal operating conditions with wall temperatures below 1400 °C, where no performance degradation was observed during a total operating time of more than 150h. Temperatures in excess of 1700 °C, however, resulted in wall failures. Scanning electron microscopy (SEM) analysis of failed SiC tiles revealed substantial surface erosion as well as thick layers of SiO_2. More details on surface erosion are discussed by Newcomb (2009).

3.2 Redesigned Reactor with Four Channels

3.2.1 Apparatus

The non-catalytic fuel reformer, illustrated in Figure 3.5, consists of four parallel channels separated by Silicon Carbide (SiC) walls, and was used for experiments with both methane/air mixtures and propane/air mixtures. The length of the main reactor section is 91.5 mm, whereas the length of the two reactor heads containing channel inlets and outlets is 40.8 mm each. The flow channels have a height of 4 mm each,

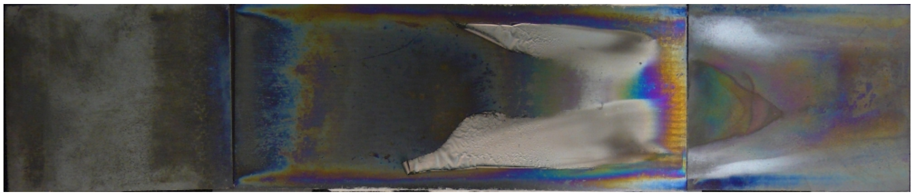

(a) Interior channel (Flow direction left-to-right): interior wall facing tiles in (b).

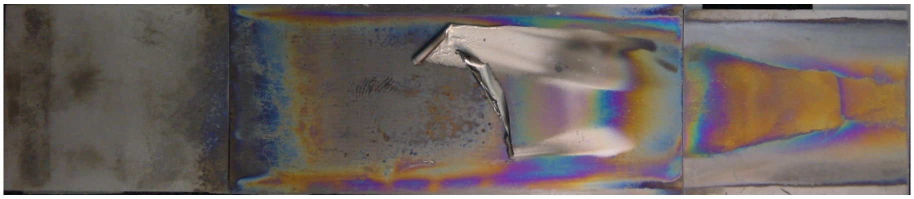

(b) Interior channel (Flow direction left-to-right): interior wall facing tiles in (a).

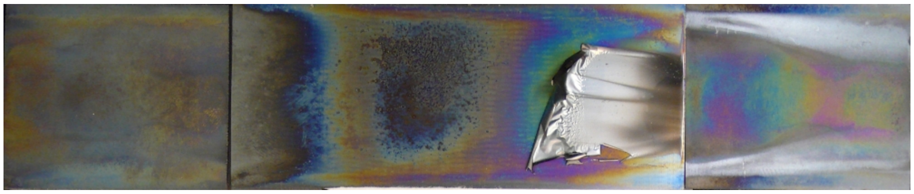

(c) Exterior channel (Flow direction left-to-right): interior wall facing tiles in (d).

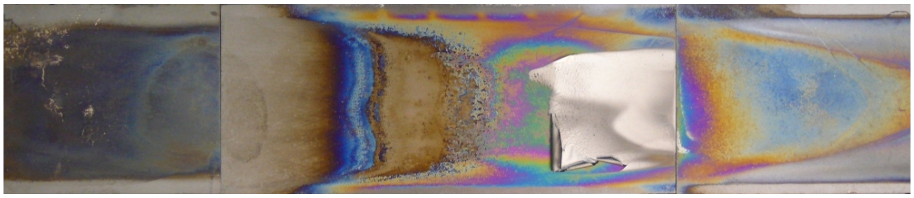

(d) Exterior channel (Flow direction left-to-right): exterior wall facing tiles in (c).

Figure 3.6: Photographs of SiC tiles removed from 6th out of nine revision of the four-channel design, which show silver-colored graphite deposits. Left tile in (d) shows discoloring from previous test where tile was used in a different location.

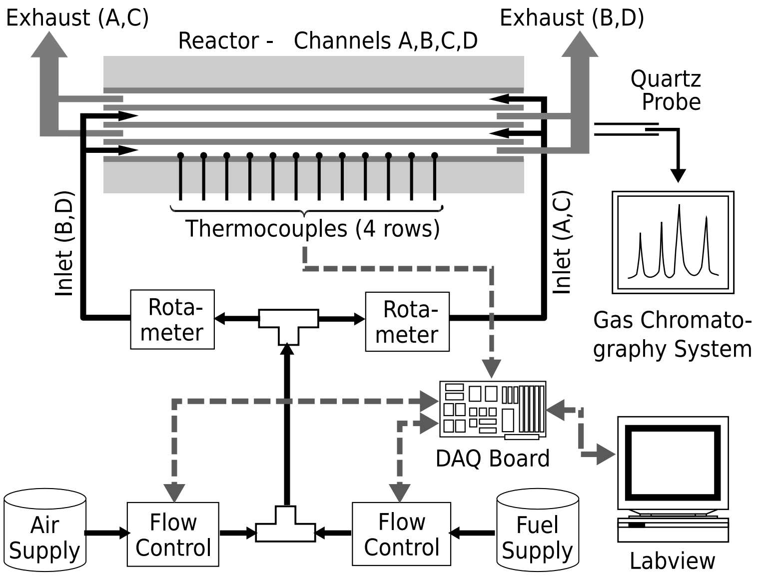

Figure 3.7: Experimental apparatus consisting of counter-flow reactor, flow conditioning system (solid connectors) and data acquisition system (dashed connectors).

and are divided by 1 mm thick SiC tiles. Two parallel alumina walls, spaced at 33.6 mm, form the lateral confinement of the flow channels. The SiC tiles are held in grooves cut into the lateral walls, which also contain an alumina paper seal to prevent gas leaks between neighboring channels. In order to minimize external heat losses, the entire reactor is contained in insulating alumina walls.

In both reactor heads every other channel is blocked to separate the combustion products from the unreacted mixture (Fig. 3.5). The cold reactants enter through the side walls at the blocked end of each channel and pass through two 6.35 mm long sections of porous SiC media (17.7 pores per centimeter, 9% density) acting as flow straighteners as well as flame arresters.

Figure 3.7 shows the experimental setup consisting of reactor, flow conditioning system, and data acquisition system. Depending on the test, either chemically pure methane or chemically pure propane is used as fuel and compressed dry laboratory air is used as oxidizer. Both fuel and oxidizer are regulated individually using calibrated mass flow controllers. Fuel and air are subsequently mixed and distributed between the opposing channels, where the flows are balanced manually using rotameters.

Each of the reactor channels is instrumented with fine-gage B-type thermocouples with a lead wire diameter of 50.8 μm and hand-soldered junctions. The thermocouples, spaced at a distance of 10 mm, are inserted through the side walls of the reactor and are positioned flush with the reactor walls to prevent the formation of flame holders. A LABVIEW data acquisition module is used to log temperature data to the hard drive and convert user specified set-points for flow rate and equivalence ratio to input signals for the flow controllers.

The dry species concentrations of the reaction products are determined using a VARIAN CP 4900 gas chromatography system (GC). The GC comprises three internal columns: a molecular sieve (Molsieve) detects H_2, N_2, CO, and unreacted oxygen (O_2) and methane (CH_4); a porous polymer unit (PPU) determines concentrations of CO_2, ethylene, ethane, acetylene, and propane; and a CP-SIL column detects higher hydrocarbons, specifically (iso,n-) butane, (iso-,n-) pentane, and n-hexane. The exhaust samples are extracted from the reactor's exhaust manifold through a quartz probe with inner and outer diameters of 2 mm and 4 mm, respectively, which is connected to the GC by inert Silco Steel tubing. All results for tests with methane/air mixtures are reported for a single probe location. The probe was centered between inner and outer channels at a distance of 10 mm from the reactor exit and a distance of 10 mm from the side wall.

Upon completion of tests with methane/air mixtures, the range of species captured by the GC system was extended by 1-butene, 1-pentene, 1-hexene, n-heptane and benzene for subsequent tests with propane/air mixtures. Also, an H-shaped traverse path was added to allow for mobility of the probe in a plane parallel to the exit face of the reactor. Measurements with propane/air mixtures are taken both between inner and outer channels in the horizontal direction as well as across each channel exit in the vertical direction.

3.2.2 Experimental Method for Tests with Methane/Air Mixtures

During the initial start-up procedure, the methane/air mixture was ignited at stoichiometric conditions at the channel outlets at an inlet velocity of 30 cm/s. Premixed flames propagated upstream until they stabilized downstream of the porous flow straighteners. As the reactor temperatures rose, inlet velocity u and equivalence ratio ϕ were slowly increased to $u = 125$ cm/s and $\phi = 2.0$. After this initial warm-up phase of approximately 15 minutes, operating conditions were selected according to specific test points, where measurements were taken at steady state.

All experiments were run at fuel-rich conditions, where three different aspects of the reactor behavior were investigated. First, the operating range of the reactor was mapped in terms of equivalence ratio and inlet velocity, and two additional test sets were designed to investigate the impact of the operating conditions on reactor wall temperatures and exhaust gas composition. In all cases, the inlet velocity was specified at standard atmospheric conditions, i.e. 25 °C and 1 atm.

For the determination of the operating range, inlet velocity and equivalence ratio were changed in steps of Δu=25 cm/s or $\Delta\phi$=0.1, and step sizes were reduced in the proximity of limits of the operating range. At u>125 cm/s and ϕ>2.2, the inlet velocity was adjusted first, after which the equivalence was increased. When evaluating u<125cm/s, the equivalence was increased to the desired value, after which the velocity was lowered incrementally. Test conditions were classified as stable if combustion could be sustained in the main reactor section for a duration of ten minutes.

Results for reactor wall temperatures were obtained for independent parameter variations of ϕ and u, which were based on the reference condition $u = 125$ cm/s and $\phi = 2.2$. Due to physical restrictions in the placement of the thermocouples, measurements contained components of both gas- and wall temperatures. In order to eliminate influences of the combustion zones on wall temperature profiles, measurements were taken after the fuel supply was briefly interrupted. The fuel/air mixture remaining in the lines was replaced by air after 5-10 seconds, which was marked by a rapid change of temperature readings. Upon extinction, temperatures started to drop, albeit at a significantly slower rate. Temperature readings were taken immediately after extinction occurred, after which the fuel supply was turned on and all combustion zones reestablished themselves by auto-ignition.

Exhaust gas measurements were taken for parameter variations similar to the ones described above. Three consecutive GC measurements were taken over a period of ten minutes, where the first sample was used to purge the system and was not included in the final results. In order to assess the repeatability of the GC measurements, the test procedure was repeated three times.

3.2.3 Method Modifications for Tests with Propane/Air Mixtures

Tests with propane/air mixtures followed a similar procedure to those conducted with methane/air mixtures. As the propane/air study focused on a closer investigation of the exhaust gas concentrations instead of showing the feasibility of the reformer concept as in the methane/air study, the experimental method was adjusted. In particular, propane tests included a variation of the equivalence ratio at an elevated inlet velocity of 250 cm/s, and the impact of the sample probe location on the measurement results was investigated.

The initial start-up procedure for reforming of propane/air was almost identical to that of methane/air, although the inlet velocity for the initial light-up was slightly higher at around 50 cm/s. During the initial warm-up phase with propane/air mixtures, however, a more pronounced tendency for unwanted propagation of combustion zones through the porous media sections was observed. Thus, the reference condition used for propane tests was shifted to ϕ=2.4 instead of ϕ=2.2 for the case of methane, although the inlet velocity used as a reference was maintained at 125 cm/s.

Results for exhaust gas concentrations were obtained for independent parameter variations of ϕ and u, which were based on two reference conditions at low and high inlet velocities, u=125cm/s and 250 cm/s, and a common equivalence ratio of

ϕ=2.4. The first measurement for variations of u was taken at the highest velocity, whereas variations of ϕ were started at the least rich condition. At each test point, two consecutive GC measurements were taken, where the first and second sample were taken downstream of inner and outer channel, respectively. Also, the influence of the sampling probe location on measurement results was investigated at the low velocity reference condition.

The inlet velocities tested with propane/air mixtures were restricted to the range of 37.5 cm/s to 300 cm/s. While the upper limit was due to limitations of the flow controller ranges, tests with 25 cm/s and lower were below the recommended limits of rotameters and resulted in oscillatory behavior.

3.2.4 Uncertainties

Results from methane/air and propane/air tests showed excellent repeatability for consecutive GC measurements. In order to get a realistic assessment of the uncertainty of the measurement, individual parameter variations were repeated in order to obtain independent measurements, where three and two test sets of experiments were conducted for experiments with methane and propane, respectively. The repeatability of GC measurements was calculated based on a Student-t distribution for all extracted samples, and complemented by a more detailed uncertainty analysis to include uncertainties of instruments and calibration gases, detailed in Appendix C. Uncertainties of measurement results were calculated at each data point as the root-sum-square of the contributing uncertainties. Whenever only a single error bar is plotted for a parameter variation, it represents the average uncertainty of the respective data set.

The uncertainty of u is based on uncertainties equal to 1% and 2% of the maximum ranges of air and fuel mass flow controllers, respectively, as well as tolerances of the channel cross-section area, estimated as 5%. The uncertainty of the inlet velocity, δu, is independent of ϕ and shows a linear increase with u. For methane, the uncertainty at the reference velocity u=125 cm/s is δu=±10.4 cm/s. For propane

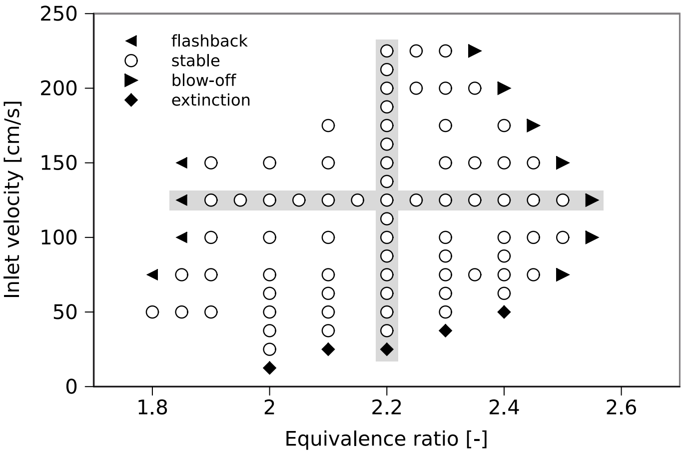

Figure 3.8: Operating range of the fuel reformer. Hatched areas indicate parameter variations discussed in Sections 3.3.2 and 3.3.3.

experiments, δu=±10.3 cm/s at u=125 cm/s and ±16.8 cm/s at u=250 cm/s. The uncertainty of the equivalence ratio, however, is a function of both ϕ and u. For methane experiments, $\delta\phi$=±0.12 at the reference condition ϕ=2.2 and u=125 cm/s, whereas for propane, $\delta\phi$=±0.15 at the reference condition ϕ=2.4/u=125 cm/s. For both fuels, $\delta\phi$ shows a marginal increase with increasing ϕ, whereas its increase is much more pronounced for decreasing u. At u=50 cm/s, $\delta\phi$ is ±0.31 for methane, whereas it reaches ±0.38 for propane.

3.3 Methane Results

3.3.1 Operating Range

Figure 3.8 shows the operating range of the reactor in terms of equivalence ratio and inlet velocity. At equivalence ratios around $\phi \approx 1.85$ flash-back was observed, where the combustion zone passed through at least one of the flow straighteners depicted in Figure 3.5. At richer conditions, primary reaction zones were stabilized downstream of the flow straighteners (Fig. 3.5), and the reactive syngas was burned in blue diffusion flames at the reactor exits (Fig. 3.9a). A further increase of the equivalence ratio led

(a) Stable operation.
(b) Blow-off.

Figure 3.9: Photographs of flames at reactor exits during stable operation and blow-off under fuel-rich operating conditions ($\phi \geq 2.2$).

to blow-off, where the primary reaction locations in the channels collapsed and the unreacted mixture burned in a yellow flame at the reactor exits (Fig. 3.9b).

A maximum equivalence ratio of 2.5 was reached at inlet velocities of 100 and 125 cm/s. At equivalence ratios smaller than 2.5 the results show a broad range of possible flow velocities for a specific equivalence ratio. Due to excessive reactor temperatures as well as hardware constraints, the number of data points was reduced for $u > 150$ cm/s and no data could be taken beyond $u = 225$ cm/s. As the inlet velocity was decreased, the reactor temperature dropped until combustion inside the channels was no longer viable and extinction occurred.

The results show a large turn-down ratio between highest possible flow rate and lowest possible flow rate, which is an important parameter for practical applications. At an equivalence ratio of 2.2 Figure 3.8 shows possible flow rates between 37.5 and beyond 225 cm/s, yielding a turn-down ratio greater than 6.

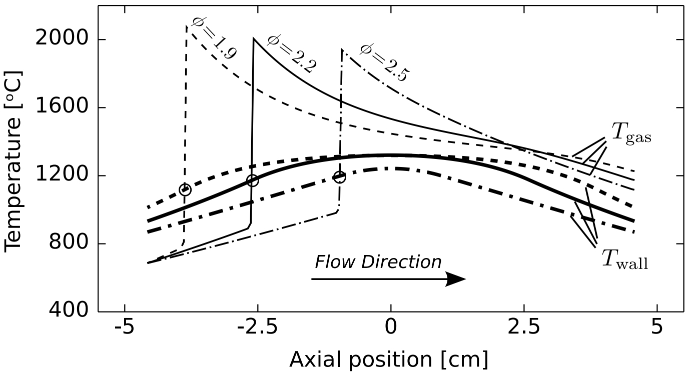

(a) Analytical results for changing ϕ at *u*=125 cm/s.

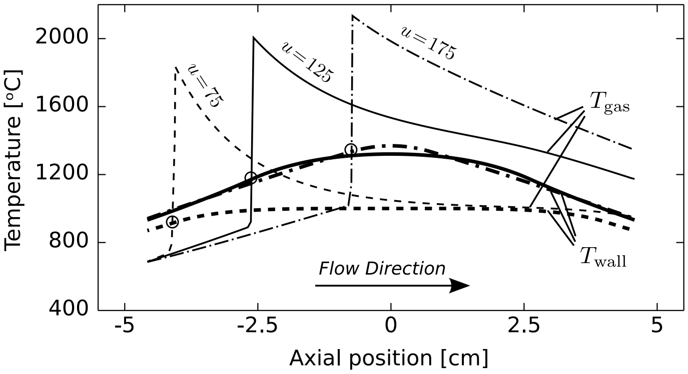

(b) Analytical results for changing *u* at ϕ=2.2.

Figure 3.10: Analytical predictions of gas and wall temperature profiles for variations of equivalence ratio (a) and inlet velocity (b). Gas temperatures for channel with opposite flow direction are not shown.

3.3.2 Reactor Temperatures

Results for the operating range (Fig. 3.8) illustrate that inlet velocity and equivalence ratio can be selected independently, which is due to a unique mechanism for the stabilization of the combustion process. Within the channels, combustion zone locations are determined by counter-flow heat exchange and thus are able to move along the channel and adjust to changes of ϕ and *u*.

Figure 3.10 shows analytical predictions for gas and wall temperature profiles that were obtained from the analytical model developed in Chapter 2 and converted to dimensional units. The model parameters used for the predictions are listed in Table 3.4, and the inlet temperature was increased to values observed in experiments

Table 3.4: Parameter values for analytical model.

Heat transfer factor μ	0.2717
Conductivity factor κ	139.006
Geometry factor ϵ	0.02038
Wall heat loss factor χ	0.05
Radiative heat loss at boundary σ	1.25

to account for preheating in the reactor heads. In Figure 3.10a, temperature profiles for three different values of ϕ at $u = 125$ cm/s illustrate that the combustion zone location, marked by a rapid increase of the gas temperature, adjusts to an increase of ϕ by moving towards the reactor center. Similarly, Figure 3.10b shows the situation for different inlet velocities u at $\phi = 2.2$, where higher inlet velocities shift the combustion zones toward the reactor center. In both cases, the additional channel length available for counter-flow heat exchange accounts for additional preheating of the cold reactants, which raises the gas temperature and thus increases the reaction rates to the level required to stabilize the combustion process.

Figure 3.10 also shows wall temperature profiles that correspond to the moving combustion front locations. The results show a broad high temperature zone in the center of the reactor, which narrows for both increases in ϕ (Fig. 3.10a) and u (Fig. 3.10b). Although the simplifications used for the analytical model restrict its application to qualitative predictions, a comparison of wall temperature predictions generally shows good agreement with experimental results, which are discussed below.

Figure 3.11 shows contour plots of wall temperature measurements along outer and inner channels of the four-channel reactor prototype (Fig. 3.5). In Figure 3.11a, temperature results are plotted versus equivalence ratio and axial position at a constant inlet velocity of 125 cm/s. In the reference case $\phi = 2.2$, the temperature in the outer channels rises quickly at the inlet and reaches temperatures above 1200 °C between axial locations -2.5 and 3.5 cm. For $\phi < 2.2$ peak temperatures remain at the same level and the high temperature zone broadens, whereas at richer conditions peak temperatures

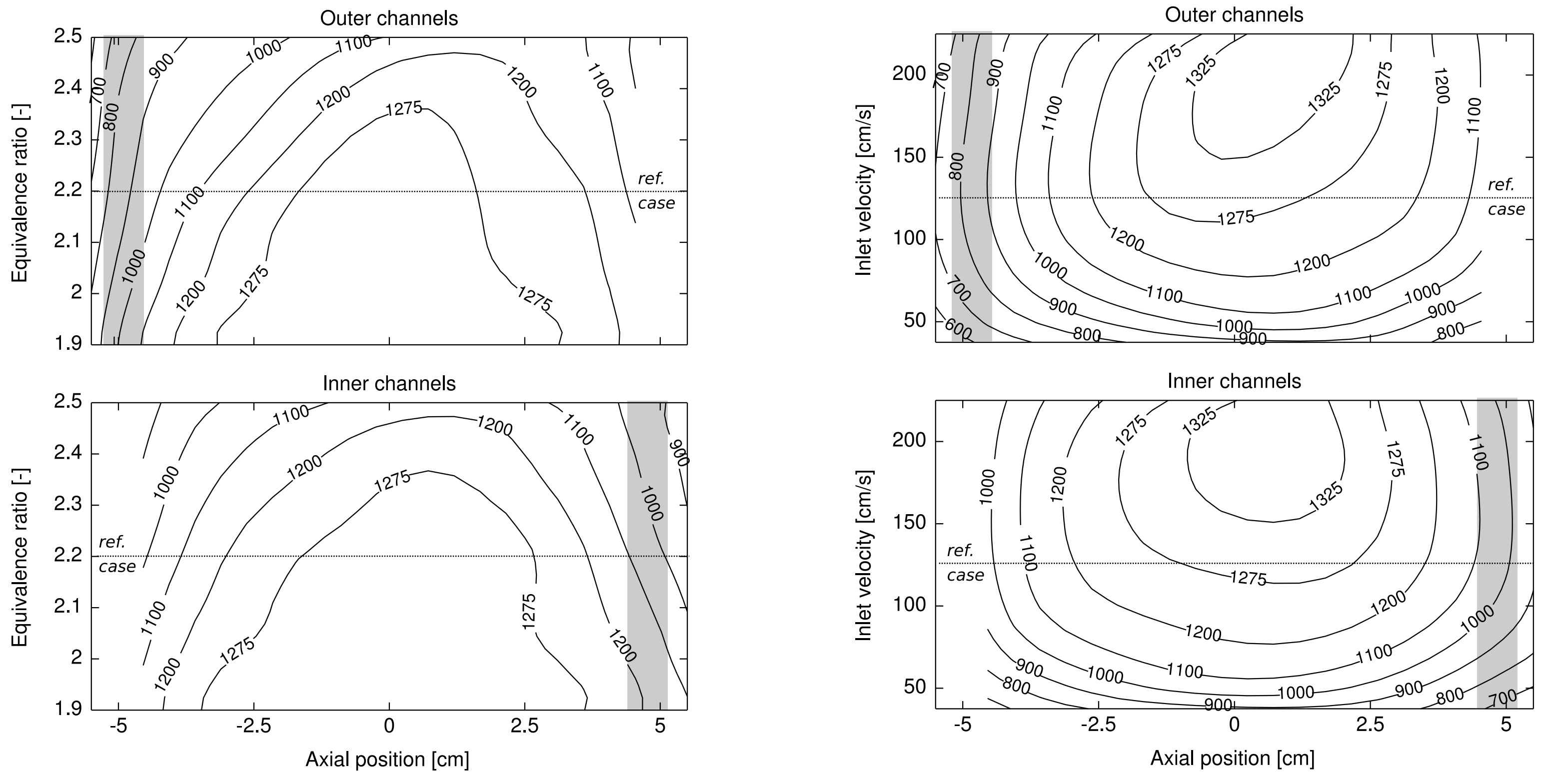

(a) Temperature profiles for changing ϕ.

(b) Temperature profiles for changing u.

Figure 3.11: Experimental results for wall temperature profiles along inner and outer channels. Contour plots illustrate dependence on equivalence ratio (a) and inlet velocity (b). Hatched areas represent flow straighteners at channel inlets (see Fig. 3.5).

drop and the high temperature zone narrows. Temperature profiles in the inner channels follow the same trend, although the high temperature zone is broader due to smaller external heat losses compared to the outer channels.

Figure 3.11b illustrates changes of temperature profiles prompted by changes of the inlet velocity at a constant equivalence ratio of 2.2. At inlet velocities higher than the reference case u = 125 cm/s, an increase of the inlet velocity prompts a moderate increase of the temperatures at the reactor center, whereas temperatures drop significantly for $u < 75$ cm/s. Variations of the inlet velocity show only a minor impact on temperatures at the flow straighteners. Similarly, the flashback-limit (Fig. 3.8) is relatively insensitive to inlet velocity, indicating that at $\phi \approx 1.85$ temperatures of the porous flow straighteners become too high to quench reactions effectively.

Figure 3.11a shows that at high equivalence ratios, the high temperature zones in outer and inner channels are shifted from the reactor center towards outlets and inlets, respectively. Similarly, Figure 3.11b displays the same shifts at high inlet velocities. In both cases the asymmetric behavior is due to differences in preheating between inlet sections upstream of the flow straighteners (Fig. 3.5). At the flow straighteners, temperatures in the outer channels are lower, and additional heat transfer across the dividing walls is required to stabilize the combustion process. Accordingly, blow-off and extinction first occurred in the outer channels, whereas flash-back was first observed in inner channels.

3.3.3 Exhaust Gas Concentrations

The impact of equivalence ratio ϕ and inlet velocity u on the syngas composition was investigated by a variation of ϕ at u = 125 cm/s and a variation of u at ϕ = 2.2. Figure 3.12a shows the exhaust gas composition as a function of equivalence ratio. H_2 concentrations increase with the equivalence ratio, but the slope flattens as conditions approach blow-off and reach a peak value of 18% between $\phi = 2.4$ and 2.5. CO reaches a peak of 14% between ϕ = 2.2 and 2.3. CO_2 levels are much lower

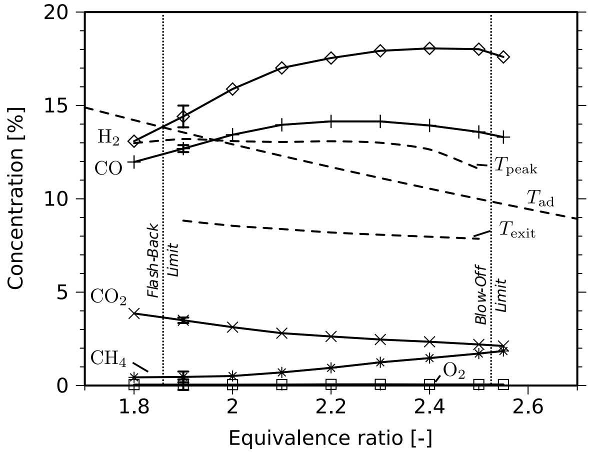

(a) Emission results for changing ϕ.

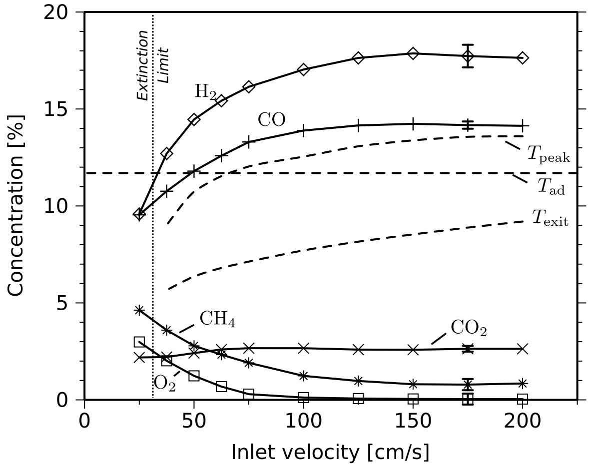

(b) Emission results for changing *u*.

Figure 3.12: Syngas composition and temperature results as function of equivalence ratio (a) and inlet velocity (b).

and continually decrease as ϕ increases. O_2 concentrations remain slightly above the detection limits in all cases, while unburned CH_4 steadily increase as ϕ increases and reaches a value of 1.8% at blow-off conditions. Temperature results show that peak reactor wall temperatures T_{peak} are superadiabatic for $\phi > 2.0$, where the theoretical adiabatic equilibrium temperature T_{ad} was evaluated using CANTERA (Goodwin, 2003). As expected, the reactor exit temperature T_{exit} remains below T_{ad}, where the difference between $T_{\mathrm{ad}} - T_{\mathrm{exit}}$ gages the magnitude of external heat losses relative to the heat released by the combustion process.

The impact of inlet velocity is illustrated in Figure 3.12b. T_{exit} increases for increasing inlet velocities, which indicates a reduced relative significance of heat losses at elevated inlet velocities. For increasing inlet velocities, results show a significant initial H_2 increase followed by a peak of 17.9% at $u = 150$ cm/s and a slight decrease at higher inlet velocities, which may be attributed to reduced residence times. CO follows the trend of H_2 with a peak of 14.2%, and CO_2 concentrations remain flat over the entire range. Peak reactor wall temperatures drop below T_{ad} for $u < 70$ cm/s where CH_4 levels increase and unreacted O_2 appears in significant concentrations. Together with a sharp decrease of H_2 concentrations, these results show the importance of superadiabatic reactor temperatures for non-catalytic fuel reforming.

In all experiments the highest hydrocarbon concentrations were measured for CH_4. All other hydrocarbon emissions remained close to the detection limit except at conditions near blow-off or extinction, where the most significant concentrations were observed for ethylene and acetylene. When increasing the equivalence ratio at $u = 125$ cm/s from $\phi = 2.2$ to 2.55 (blow-off), ethylene showed a moderate increase from 0.12 to 0.49%, whereas acetylene increased sharply from 0.01 to 0.85%.

The emission results clearly illustrate differences between conditions at blow-off and extinction, which were discussed briefly in Figure 3.8. Figure 3.12a shows that for an increase of the equivalence ratio H_2 concentrations continue to increase until blow-off occurs, where counter-flow heat exchange is no longer able to stabilize the

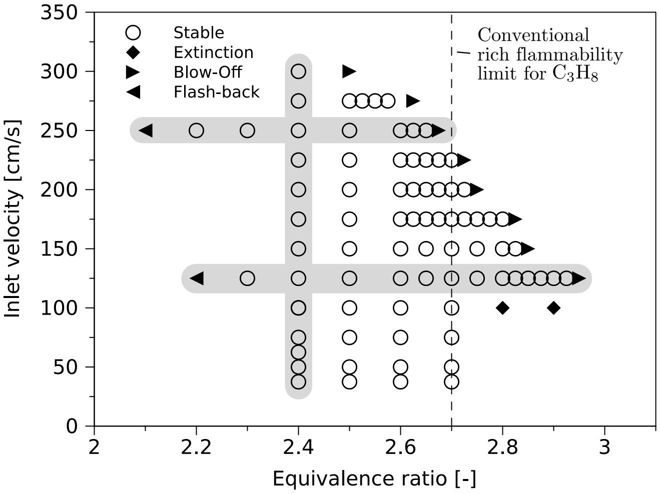

Figure 3.13: Operating range of the fuel reformer for C_3H_8/air mixtures. Shaded lines indicate parameter variations conducted for emissions analysis.

combustion process. For the case of extinction, Figure 3.12b shows that contrary to blow-off, the H_2 concentrations decrease continuously as the inlet velocity decreases. In addition, concentrations of unreacted CH_4 and O_2 increase as the reactor temperatures decrease, which indicates that reactions are quenched by wall heat losses.

3.4 Propane Results

3.4.1 Operating Range

Figure 3.13 shows the operating range of the reactor in terms of equivalence ratio and inlet velocity. Depending on the inlet velocity, flash-back was observed between ϕ=2.1 and 2.2, where the combustion zone passed through at least one of the flow straighteners depicted in Figure 3.5. At richer conditions, primary reaction zones were stabilized downstream of the flow straighteners (Fig. 3.5), and the reactive syngas was burned in blue diffusion flames at the reactor exits. A further increase of the equivalence ratio led to blow-off, where the primary reaction locations in the channels were no longer viable and the unreacted mixture burned in a yellow flame at the reactor

Table 3.5: Equilibrium composition for C_3H_8 combustion (based on standard atmospheric conditions: 25 °C, 1 atm).

	ϕ=2.4		ϕ=2.8	
	$[\%]_{wet}$	$[\%]_{dry}$	$[\%]_{wet}$	$[\%]_{dry}$
H_2O	5.45	—	2.45	—
H_2	21.51	22.75	26.66	27.33
CO	17.81	18.84	20.1	20.6
CO_2	2.41	2.55	1.76	1.80
CH_4	1.5×10^{-4}	1.6×10^{-4}	0.04	0.04
C_2H_2	4.6×10^{-10}	4.9×10^{-10}	1.3×10^{-8}	1.3×10^{-8}
C_2H_4	2.0×10^{-10}	2.1×10^{-10}	1.9×10^{-7}	1.9×10^{-7}
O_2	1.3×10^{-13}	1.3×10^{-13}	2.5×10^{-18}	2.5×10^{-18}
N_2	52.81	55.86	49.0	50.23
T_{ad}	1054.37 °C		837.61 °C	

exits.

At u=125 cm/s, stable combustion was observed between equivalence ratios of 2.3 and 2.9, whereas at u=250 cm/s, the stable range extended from 2.2 to 2.65. Thus, the operating range of the reactor extends beyond the conventional flammability limit for C_3H_8 at ϕ=2.7 (Glassman, 1996). At equivalence ratios lower than 2.9 the results show a broad range of possible flow velocities for a specific equivalence ratio, and maximum flow rates are an order of magnitude higher than those of conventional flames, which reach $u \approx 45$ cm/s at stoichiometric conditions (Glassman, 1996). The results show a large turn-down ratio between highest possible flow rate and lowest possible flow rate, which is an important parameter for practical applications. At ϕ=2.4 Figure 3.13 shows possible flow rates between 37.5 and beyond 300 cm/s, yielding a turn-down ratio close to 10. Due to hardware constraints, no data could be taken above u=300 cm/s. As the inlet velocity was decreased, the reactor temperature dropped until either combustion inside the channels was no longer viable and extinction occurred, or the lower limit of the tested velocity range was reached.

3.4.2 Exhaust Gas Concentrations

The results for the operating range illustrate that the counter-flow reactor stabilizes combustion zones for independent variations of inlet velocity and equivalence ratio. In order to investigate their respective impact on the exhaust gas concentrations, three parameter variations were performed: first, the impact of the inlet velocity was studied at a constant equivalence ratio of 2.4; second, the equivalence ratio was varied at a constant inlet velocity of 125 cm/s; and third, an additional variation of equivalence ratio was performed at an elevated inlet velocity of 250 cm/s. These are indicated in Fig. 3.8 as shaded lines.

Table 3.5 shows equilibrium predictions for "wet" and "dry" exhaust gas concentrations, referring to data including and excluding water vapor in the product stream. The equilibrium data were obtained for constant pressure and adiabatic conditions using the chemical kinetics package CANTERA (Goodwin, 2003). Chemical equilibrium is the idealized thermodynamic state where the reacted mixture assumes maximum entropy, which in practice, however, requires infinite residence time for all chemical reactions to complete. Below, equilibrium concentrations will be used as a benchmark to gage the efficiency of the reforming process. At the tabulated conditions, both propane and oxygen are consumed completely to form H_2O, H_2, CO and CO_2. Among small hydrocarbons, CH_4 occurs with the highest concentrations, which, however, are insignificant when compared to the main reaction products.

As ϕ is increased from 2.4 to 2.8, the adiabatic equilibrium temperature drops by more than 200° from 1054.37 °C to 837.61 °C. At the same time, concentrations of CO and H_2 increase, whereas the amount of H_2O decreases and concentrations of small hydrocarbons remain insignificant.

3.4.2.1 Impact of Sampling Probe Location

Variations of measurement results with the sampling probe placement were studied by moving the probe in a plane parallel to the exit face of the reactor at a distance of

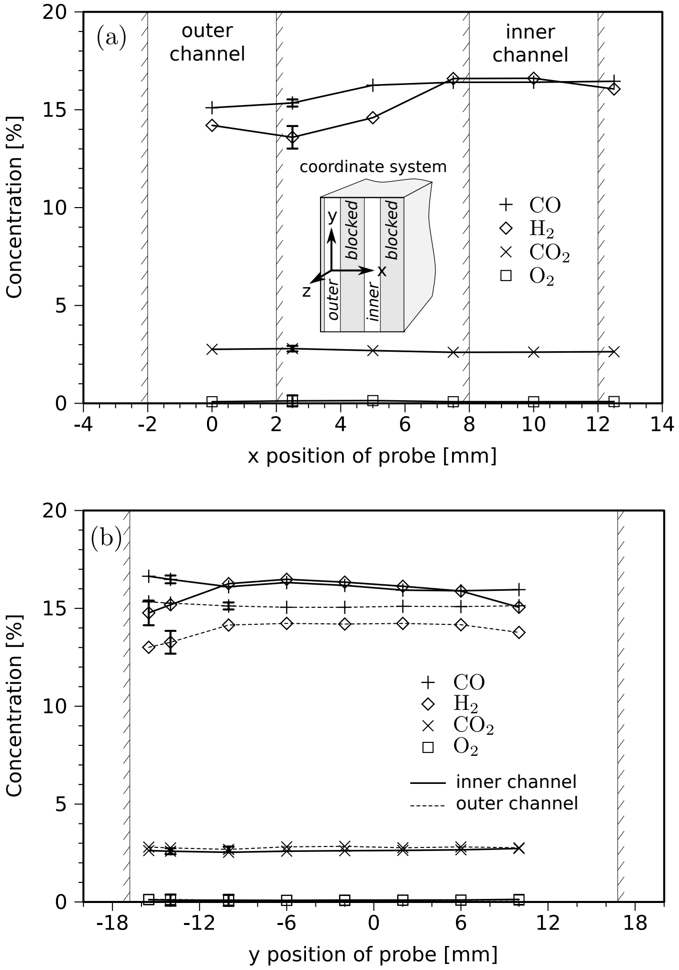

Figure 3.14: Concentration of major syngas components CO, H_2, CO_2 and O_2 at different probe locations at u=125 cm/s and ϕ=2.4: variations of x-position (a) and y-position (b) of the sampling probe.

10 mm, while holding the operating conditions constant at u=125 cm/s and ϕ=2.4. Figure 3.14 shows results for the major syngas components CO, H_2, CO_2 and O_2, where the inset in the figure specifies the coordinate system used for the positioning of the probe. Here, x-displacements illustrate variations of the syngas composition as the probe is moved between inner and outer channels at y=0 (Fig. 3.14a). Variations in the y-direction were conducted at x=0 and x=10, and show changes in concentration across the width of outer and inner channel, respectively (Fig. 3.14b).

Figure 3.14a illustrates that both CO and H_2 concentrations are higher in the inner channel, whereas the differences for CO_2 and O_2 are minute. Differences in species concentrations are attributed to different temperature levels in inner and outer channels, which are discussed in more detail in Sections 3.4.2.2 and 3.4.2.3. As expected for an oxygen-starved combustion process, O_2 levels are insignificant, as the uncertainty of oxygen measurements is ±0.28%. Figure 3.14b shows that species concentrations are almost independent of the probe location with the exception of regions close to the channel wall at y=-16.8 mm. Compared to the center region, CO increases, whereas H_2 decreases.

The impact of the probe location on minor syngas components occurring with significant concentrations, C_2H_2, CH_4, C_2H_4 and C_6H_6, is illustrated in Figure 3.15. Results for the x-direction (Fig. 3.15a) show that as the probe is moved from the outer channel toward the inner channel, concentrations of CH_4 and C_2H_4 increase sharply before they decrease downstream of the inner channel. Simultaneously, measurements of C_2H_2 show a local minimum between the channels. Results for the y-position (Fig. 3.15b) show that, consistent with Fig. 3.15a, concentrations of C_2H_2 and CH_4 are higher in the outer channel, whereas the level C_2H_4 is higher in the inner channel.

At ϕ=2.4, equilibrium calculations predict dry concentrations of H_2 at 22.75% and CO at 18.84% (Table 3.5). In comparison, experimental concentrations were significantly lower, where, depending on the probe location, measurements of H_2 yielded 13.0 to 16.6% and CO ranged from 15.1 to 16.6%. These discrepancies can be explained

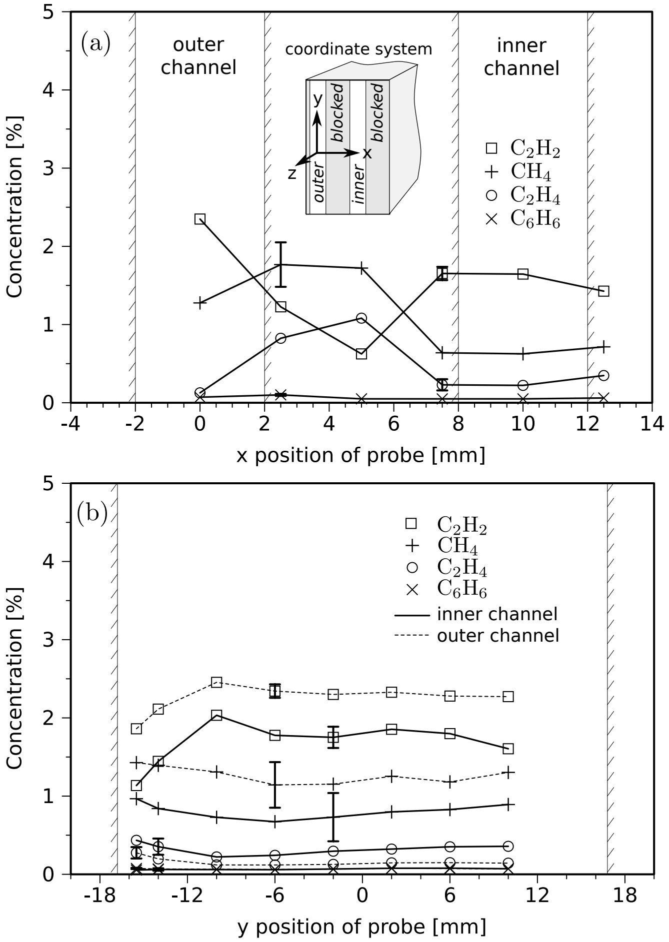

Figure 3.15: Concentration of minor syngas components C_2H_2, CH_4, C_2H_4 and C_6H_6 at different probe locations at u=125 cm/s and ϕ=2.4: impact of x-position (a) and y-position (b) of the sampling probe.

by the occurrence of partially reacted hydrocarbon species in the exhaust, which are not predicted by equilibrium. Also, a comparison of molar balances for both hydrogen and oxygen indicate increased amounts of H_2O vapor in the experiments, which will be discussed in more detail in Section 3.4.2.4.

3.4.2.2 Major Syngas Components

Figure 3.16 illustrates the impact of parameter variations of u and ϕ on the major exhaust gas species CO, H_2, CO_2 and O_2, which are presented for probe locations

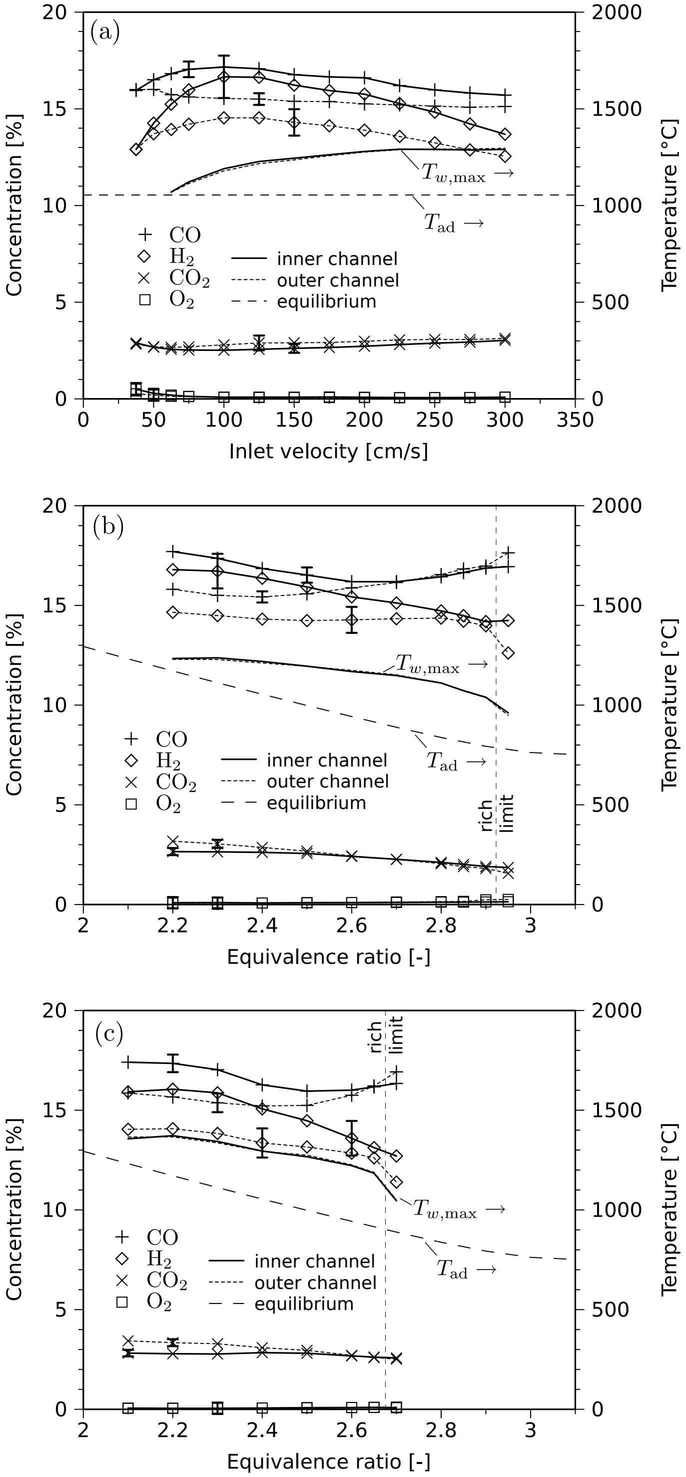

Figure 3.16: Concentration of major syngas components CO, H_2, CO_2 and O_2, and maximum wall temperature: variation of inlet velocity at ϕ=2.4 (a); variations of equivalence ratio at u=125 cm/s (b) and u=250 cm/s (c).

downstream of both inner and outer channels. Along with exhaust gas measurements, Fig. 3.16 also illustrates maximum wall temperatures, $T_{w,\mathrm{max}}$, within inner and outer reactor channels. In all cases, $T_{w,\mathrm{max}}$ lies above the adiabatic equilibrium temperature T_{ad}, indicating superadiabatic combustion temperatures. At elevated inlet velocities and conditions close to the rich operating limits, $T_{w,\mathrm{max}}$ exceeds T_{ad} by more than 200°.

Previous results from filtration combustion show that H_2 concentrations are strongly influenced by reaction temperatures (Dixon et al., 2008). Peak wall temperatures along inner and outer channels, however, do not show different peak values (Fig. 3.16a). A comparison of temperature profiles along inner and outer channels, however, reveals that the former are characterized by broadened high temperature zones, which is discussed in Section 3.3. Thus, differences in results for inner and outer channels are attributed to different residence times in high temperature zones.

Figure 3.16a shows the influence of the inlet velocity on the concentration of major syngas components. In the inner channels, concentrations of CO and H_2 peak between u=100-125 cm/s, where peak values are 17.2 and 16.7%, respectively. Beyond this velocity range, CO and H_2 levels show a slight decline, whereas at lower velocities, concentrations of both species decrease rapidly. At u>100 cm/s, H_2 concentrations in the outer channel show similar trends to those observed in the inner channels, albeit at lower levels. At the same time, CO concentrations decrease more markedly in the inner channels, while they remain almost constant in the outer channels. Concentrations of CO_2 are only marginally affected by the inlet velocity, where differences between inner and outer channels remain within their respective levels of uncertainty.

Increases in the velocity generally result in an increase of the maximum temperatures, which result in higher reaction rates to balance the increased flow rates through the reaction zones. While temperature increases are often accompanied by increases in the H_2 concentration (Dixon et al., 2008), the decline of H_2 observed with increased velocities in this work is attributed to shortened residence times, preventing a completion of chemical reactions. At the other end of the velocity range, temperature readings drop at an accelerated rate as u is decreased below 100 cm/s, which indicates that the relative importance of external heat losses increases as the rate of heat release decreases.

Figures 3.16b and 3.16c show variations of the equivalence ratio at two different inlet velocities, u=125 and 250 cm/s. Consistent with results discussed above, CO and H_2 concentrations are higher in the outer channels. Contrary to equilibrium calculations that predict an increase of H_2 concentrations with increasing ϕ, experiments show a decline with increasing ϕ. The drop of H_2 is explained by significant increases of small hydrocarbons species (CH_4, C_2H_2 and C_2H_4), which are intermediate reaction products of the fuel break-down (Section 3.4.2.3).

Results for CO concentrations in both low-speed and high-speed variations of ϕ (Fig. 3.16b/c) show that after an initial decrease with increasing ϕ, the trend reverses as the mixture becomes richer. The variation of CO is consistent with trends observed for small hydrocarbon species, which are discussed below.

3.4.2.3 Minor Syngas Components

As shown in Table 3.5, equilibrium calculations do not predict significant amounts of hydrocarbon species such as CH_4, C_2H_2 and C_2H_4. These species are, however, detected in experiments, which means that H_2 concentrations remain below equilibrium levels due to insufficient conversion of partially reacted hydrocarbons.

The literature on rich combustion chemistry provides some insights to the reaction kinetics involved in the break-down of propane (Glassman, 1996; Law, 2006). The initial attack is an H-abstraction reaction by either of the radicals H, O, or OH, which removes an H-atom from C_3H_8. Depending on whether the initial H-abstraction occurs on primary or secondary $C-H$ bonds, either *n*-propyl or *i*-propyl radicals are formed. Although the reaction forming *n*-propyl has a higher activation energy, a larger pre-exponential reaction constant results in both reactions occurring with similar magnitudes (Law, 2006).

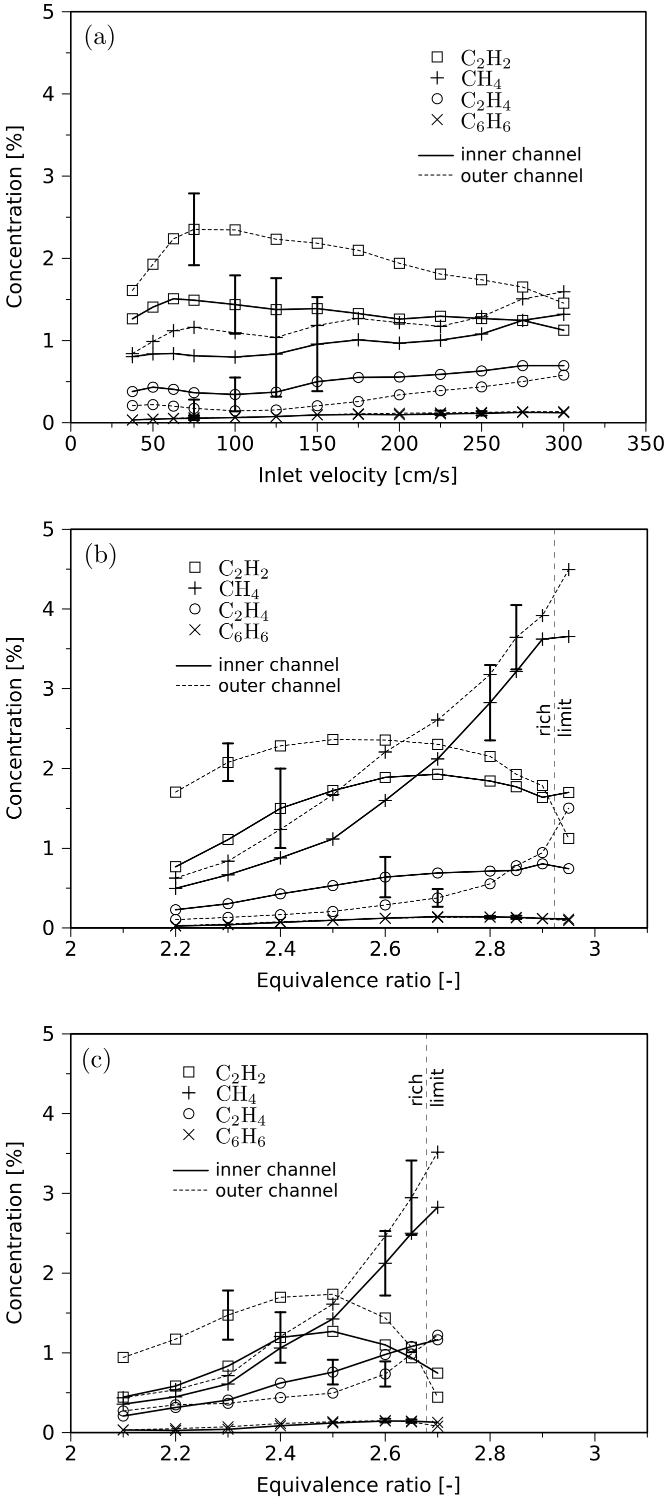

Figure 3.17: Concentration of minor syngas components C_2H_2, CH_4, C_2H_4 and C_6H_6: variation of inlet velocity at ϕ=2.4 (a); variations of equivalence ratio at *u*=125 cm/s (b) and *u*=250 cm/s (c).

The further break-down of *n*-propyl under rich conditions is most likely by a β-scission into ethylene (C_2H_4) and methyl radical (CH_3). A further H-abstraction of ethylene by H and OH produces a vinyl (C_2H_3) radical, which quickly reacts to form acetylene (C_2H_2). Alternatively, ethylene may be attacked by O to form the radicals CH_3 and HCO. The *i*-propyl radical, however, typically undergoes a further H-abstraction to form propene (C_3H_6). Propene is either oxidized by an O atom to break the C=C bond, or may undergo another H-abstraction to form an allyl radical (C_3H_5), which further reacts to form oxygenated or non-oxygenated C_1 and C_2 species (Law, 2006).

Many intermediates of the complex fuel break-down of rich propane combustion are found in the syngas, where CH_4, C_2H_2 and C_2H_4 were most significant (Fig. 3.17). Limitations of the GC system did not allow for a conclusive analysis of C_3 species, although results indicate that concentrations are significantly lower than those of C_2 intermediates. Among the remaining hydrocarbon species captured by the analysis, C_6H_6 was most significant with typical levels of 0.1%.

Fig. 3.17a illustrates concentrations of minor syngas for a variation of u. With the exception of C_2H_4, concentrations of partially reacted hydrocarbons are lower in the inner channels, which is consistent with higher hydrogen concentrations. Also, as u increases, the impact of the shortened residence time becomes apparent: concentrations of C_2H_2, which is formed late in the fuel break-down, decrease with shortened residence time, whereas intermediate species formed earlier increase.

Results for variations of ϕ at both intermediate and high velocities indicate a strong influence of reaction chemistry on the concentration of intermediate hydrocarbon species (Figs. 3.17b/c). The most significant feature in both graphs are characteristics of C_2H_2 concentrations, which decline at very rich conditions after an initial increase with increasing ϕ. This behavior is, however, consistent with earlier observations on CO results, which show a local minimum where C_2H_2 peaks. Moreover, CH_4 levels increase by significant amounts at ϕ beyond the C_2H_2 peaks. As ϕ increases, the lengths of the high temperature zones in both inner and outer channels decrease (Section 3.3), reducing residence times available for reactions. Thus, the increase of CH_4 is unlikely caused by an increased conversion of C_2H_2. The trend reversal of C_2H_2 concentrations with increasing ϕ coincides, however, with characteristic changes of the reactor temperature. Initially, $T_{w,\max}$ decreases much slower than T_{ad}, increasing the temperature difference (Figs. 3.16b/c). As ϕ increases further, the increase of temperature differences is less pronounced until $T_{w,\max}$ drops sharply close to the rich operating limits. Changes in reaction temperatures have a significant impact on reaction rates, which makes a shift in competing reaction paths in the break-down of propane a likely cause for the characteristic behavior of C_2H_2 and CO.

One significant result shown in Fig. 3.17 is the presence of C_6H_6 in the exhaust, where increased levels are observed at elevated velocities as well as at ϕ close to the rich operating limits. The formation of C_6H_6 is closely linked to C_2H_2 in the exhaust (Law, 2006), both of which are important precursors for PAH and, subsequently, soot (Richter and Howard, 2002; Kamphus et al., 2008). While inner and outer channels show significant differences in C_2H_2 levels, concentrations of C_6H_6 are, however, comparable. Also, it is noted that peak values of C_6H_6 are not observed at the same locations as C_2H_2 peaks. Together, the limited information on intermediates important for PAH formation is inconclusive. Thus, a more specific understanding requires detailed simulations with appropriate chemical kinetics mechanisms and/or inclusion of additional intermediate species for the GC analysis and quantitative soot measurements in the flue gas.

3.4.2.4 Hydrogen Balance

Numerical results for ultra-rich combustion of hydrocarbon fuels show strong evidence of the importance of steam-reforming reactions downstream of the main reaction zone, where the H_2O concentration decreases from its peak value (Zamashchikov

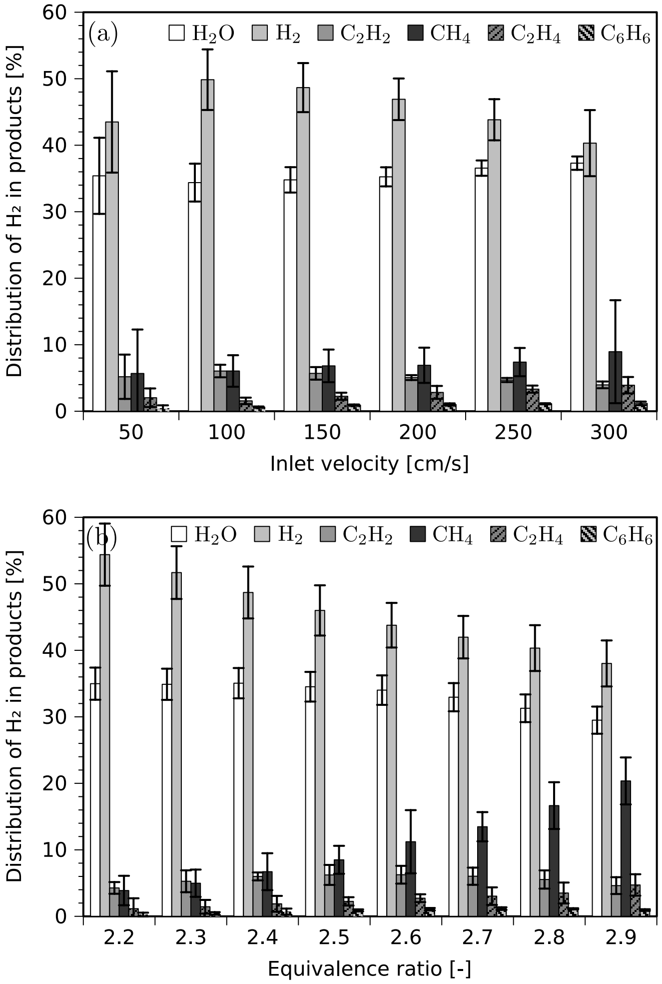

Figure 3.18: Distribution of H_2 in products: (a) variation of velocity at ϕ=2.4; (b) variation of equivalence ratio at *u*=125 cm/s.

et al., 2004; Dhamrat and Ellzey, 2006; Dixon et al., 2008). Steam-reforming reactions are endothermic, and can contribute significant amounts of H_2 to the net hydrogen production (Dixon et al., 2008).

Results for both major and minor species in the exhaust gas indicate a strong influence of steam reforming for the break-down of propane and intermediate hydrocarbon species. Due to limitations of the gas chromatography system, however, it was not possible to directly measure the H_2O content of the syngas. Still, the H_2O concentration can be determined in a post-processing step by molar balances of either hydrogen or oxygen between reactants and products.

Figure 3.18 illustrates the distribution of hydrogen in product species containing hydrogen as a function of u and ϕ. All percentages except those for H_2O are calculated from direct concentration measurements averaged between inner and outer channels. The percentage of H_2 bound by species i is defined as $\eta_{H_2,i}=m_i\dot{N}_{i,out}/4\dot{N}_{C_3H_8,in}$, with m_i defined as the number of H_2 moles bound in each mole of product i. The molar flow rates $\dot{N}_{i,out}$ are computed from molar concentrations as $\dot{N}_{i,out} = y_{i,out}\dot{N}_{out}$, where y_i is the dry molar concentration. Furthermore, the ratio of product to reactant molar flow rate was calculated from a nitrogen balance, i.e. $y_{N_2,in}\dot{N}_{in} = y_{N_2,out}\dot{N}_{out}$.

The percentage of hydrogen bound in H_2O is evaluated indirectly using an oxygen balance between reactants and products, along with the assumption that the only significant product species containing O are H_2O, CO, CO_2, and O_2, yielding

$$\dot{N}_{H_2O,out} = 2\left(\dot{N}_{O_2,in} - \tfrac{1}{2}\dot{N}_{CO,out} - \dot{N}_{CO_2,out} - \dot{N}_{O_2,out}\right)$$

While the water content of the syngas can also be found by a hydrogen balance between H_2 in reactants and products, the latter procedure has a higher uncertainty due to the large number of species containing H. A comparison of results for both approaches, however, shows good agreement, indicating that significant exhaust gas species containing H_2 are accounted for in the analysis of the exhaust gas.

A variation of the inlet velocity at constant ϕ shows the impact of steam reforming on the conversion to hydrogen (Fig. 3.18a). At the lowest inlet velocities, higher H_2O as well as lower H_2 concentrations are attributed to reduced reaction rates at low reactor temperatures, resulting in lower H_2 percentages. Peak conversion of propane to H_2 occurs around 100 cm/s. At higher velocities, concentrations of H_2 decrease while H_2O increases, which is attributed to a reduction of steam reforming as residence times shorten.

A comparison of hydrogen balances for increasing ϕ (Fig. 3.18b) shows only marginal decreases of the relative amount of H_2O in the products. At the same time, the hydrogen balance shows a shift from H_2 to small hydrocarbon species, implying a reduced efficiency of steam reforming.

In general, results show that the quantity of H_2O produced in experiments is substantially higher than predicted by equilibrium, where at ϕ=2.4, Table 3.5 lists wet concentrations of 21.51% for H_2 and 5.45% for H_2O. As equilibrium does not predict significant quantities of H in other product species, steam accounts for 20.2% of hydrogen, which is substantially lower than experimental percentages of 40 to 50% (Fig. 3.18a). Similarly, under-predictions of H_2O are apparent in numerical results with propane fuel (Zamashchikov et al., 2004). Results from rich filtration combustion of heptane, however, have shown that a more complete conversion of a hydrocarbon into H_2 is feasible at sufficiently high temperatures (Dixon et al., 2008).

It is noted that in principle, a similar carbon balance between reactants and products can be used to quantify carbon contained in product species not captured by the GC system. An analysis of the GC results reveals, however, that carbon contained in the measured product species balances the carbon in the reactant stream within the level of uncertainty. While this does not contradict formation of soot and graphite in experiments, it indicates that carbon is preferentially converted to CO, CO_2, and small hydrocarbon species.

3.5 Comparison of Methane and Propane Results

3.5.1 Operating Range

Figure 3.19 illustrates that experimental results from propane (Section 3.4) show a wider operating range compared to results for reforming of methane (Section 3.3). This result is consistent with expectations, as propane has a significantly richer conventional flammability limit (ϕ=2.7) than methane (ϕ=1.7) (Glassman, 1996). A comparison of the maximum ϕ to the respective conventional limit shows a more pronounced improvement for methane than for propane, which is attributed to differences in the

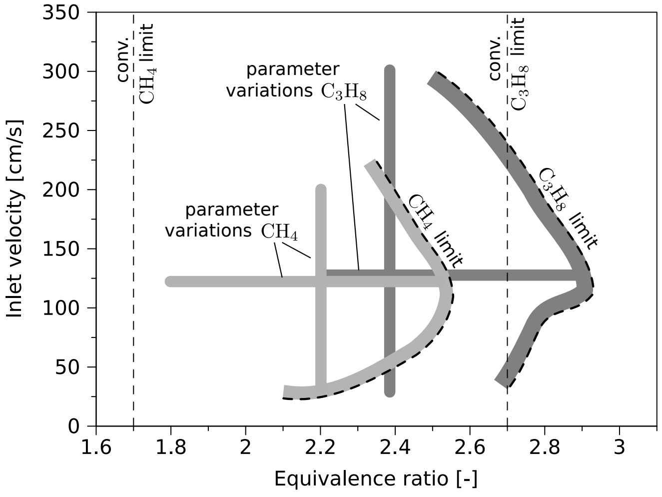

Figure 3.19: Comparison of operating range for C_3H_8/air mixtures to results for CH_4. Shaded lines indicate parameter variations conducted for emissions analysis..

reaction chemistry.

3.5.2 Exhaust Gas Concentrations

Figure 3.20 shows a comparison of major species concentrations for reforming of propane, averaged between inner and outer channels, with methane results. Due to different operating ranges, the propane data in Figure 3.20 was taken at a fixed equivalence ratio of 2.4 and the methane data was taken at 2.2. Variations of ϕ, however, were conducted at an identical inlet velocity of u=125 cm/s (Fig. 3.20b). Results for both variations show higher concentrations of H_2 for methane fuel, whereas CO is higher for propane fuel, which is attributed to differences in the ratio of carbon-to hydrogen atoms bound in a fuel molecule. In contrast to the results for propane, the concentrations of H_2 are higher than CO for methane. Also, a comparison of temperature results shows that wall temperatures are consistently lower for propane.

A variation of the inlet velocity (Fig. 3.20a) illustrates that H_2 concentrations peak at lower velocities for propane fuel and show a more pronounced decline as u is increased. At the lower end of the tested range, the methane data shows clear evidence

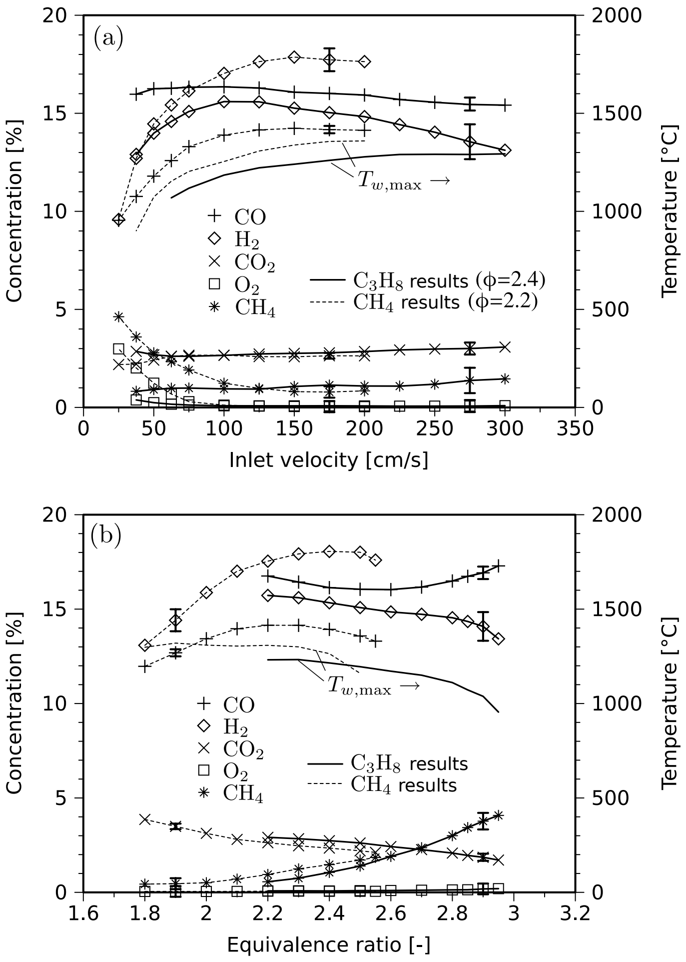

Figure 3.20: Comparison of experimental results for C_3H_8 to results for CH_4: (a) variation of velocity at constant ϕ; (b) variation of equivalence ratio at u=125 cm/s.

of extinction, as levels of unreacted O_2 increase sharply. Results for propane, however, show only a modest increase of O_2 under those conditions. The different behavior is consistent with the conventional flammability limits of the respective fuel. At ϕ=2.2, methane results lie beyond the conventional flammability limits, whereas propane data at ϕ=2.4 lies within the conventional flammable range.

Results for equivalence ratio variations (Fig. 3.20b) reveal significant differences in the progression of H_2 concentrations. In the case of propane, H_2 concentrations decrease as ϕ is increased, which is opposite to trends predicted by equilibrium (Table 3.5). Methane data, however, show an increase of H_2 concentrations as ϕ is increased.

The decrease of H_2 in the case of propane is, however, consistent with substantial increases of partially oxidized fuel, e.g., C_2 species and, at richer equivalence ratios, CH_4 (Section 3.4.2.3). While trace amounts of C_2 species were also found in syngas obtained from methane, concentrations were substantially lower. For methane, the most significant concentrations were observed for C_2H_4 and C_2H_2, where increases of ϕ from 2.2 to 2.55 at u=125 cm/s resulted in an moderate increase of C_2H_4 from 0.12 to 0.49%, whereas C_2H_2 increased sharply from 0.01 to 0.85%. The differing behavior of the two fuels is attributed to the fact that in the case of methane, C_2 species are synthesis products rather than intermediate species of the fuel break-down as in the case of propane.

A recent study for a direct comparison of different fuels for equivalence ratios between 1.0 and 2.5 was conducted in a filtration reactor, which is an alternative non-catalytic reformer concept with propagating reaction zones (Toledo et al., 2009). Results were obtained for low flow velocities, and revealed the same syngas components as those found in the counter-flow reformer, including significant quantities of C_2 species. Consistent with the results shown above, H_2 concentrations were higher for methane-air mixtures than for propane-air mixtures, with peak values of 15% and 13% at $\phi=2.4$, respectively. Peak values obtained for the counter-flow reactor investigated in this study were higher with 18% for methane-air and 15.6% for propane-air at similar equivalence ratios. Other results from filtration combustion, however, show comparable hydrogen concentrations at elevated inlet velocities (Dhamrat and Ellzey, 2006). In the same study, rich combustion of methane-air mixtures was demonstrated for equivalence ratios of up to 5.0, where peak H_2 concentrations exceed 25%.

3.5.3 Efficiency of the Reforming Process

Out of many possible metrics useful for the assessment of the fuel reforming efficiency, three are presented. First, the rate of H_2 moles generated can be compared to the maximum rate available in the reactant stream. Thus, the *molar hydrogen conversion* is given by

$$\eta_{\mathrm{H}_2} = \frac{\dot{N}_{\mathrm{H}_2,out}}{\dot{N}_{\mathrm{H}_2,max}} = \frac{\dot{N}_{\mathrm{H}_2,out}}{4\dot{N}_{\mathrm{C}_3\mathrm{H}_8,in}} \tag{3.1}$$

which has previously been introduced for the discussion of the hydrogen balance in Section 3.4.2.4. Second and third, two different energy conversion efficiencies are defined,

$$\eta_{\mathrm{Energy,H}_2} = \frac{\dot{N}_{\mathrm{H}_2}\ LHV_{\mathrm{H}_2}}{\dot{N}_{\mathrm{fu},in} LHV_{\mathrm{fu}}} \tag{3.2a}$$

$$\eta_{\mathrm{Energy}} = \frac{\sum_{out} \dot{N}_i\ LHV_i}{\dot{N}_{\mathrm{fu,in}} LHV_{\mathrm{fu}}} \tag{3.2b}$$

where *LHV* refers to the lower heating value of the species in kJ/kmol at standard atmospheric conditions. The *hydrogen energy conversion efficiency* (Eq. 3.2a) compares the chemical energy bound in H_2 produced by the reforming process to the chemical input energy of reactants and is a metric for the energy efficiency of hydrogen production. The *total energy conversion efficiency* (Eq. 3.2b) is defined similarly, but accounts for all energy carrying species in the syngas. Thus, η_{Energy} implicitly measures process losses, i.e. heat losses through reactor walls and sensible energy of the flue gases.

Fig. 3.21 illustrates η_{H_2}, $\eta_{\mathrm{H}_2,\mathrm{Energy}}$ and η_{Energy} for changing u and ϕ, where results for both methane and propane are plotted. Curves for molar hydrogen conversion as a function of u (Fig. 3.21a) show similar characteristics for both fuels, although propane results peak at lower u with 49.9% at u=100 cm/s, whereas CH_4 shows a peak value of 50.7% at a higher inlet velocity of u=150 cm/s. In addition, molar hydrogen conversion results for changing ϕ (Fig. 3.21b) show similar results for the overlapping range ϕ=2.2–2.5. Both fuels show a drop of efficiency for ϕ>2.2, which in both cases is explained by an increase of small hydrocarbon species.

The molar hydrogen conversion obtained for a filtration reactor, an alternative non-catalytic concept with propagating combustion zones, however, yielded close to 80% at similar conditions for *n*-heptane as the fuel (Dixon et al., 2008). The difference between the reactor concepts are attributed to longer residence times in high temperature

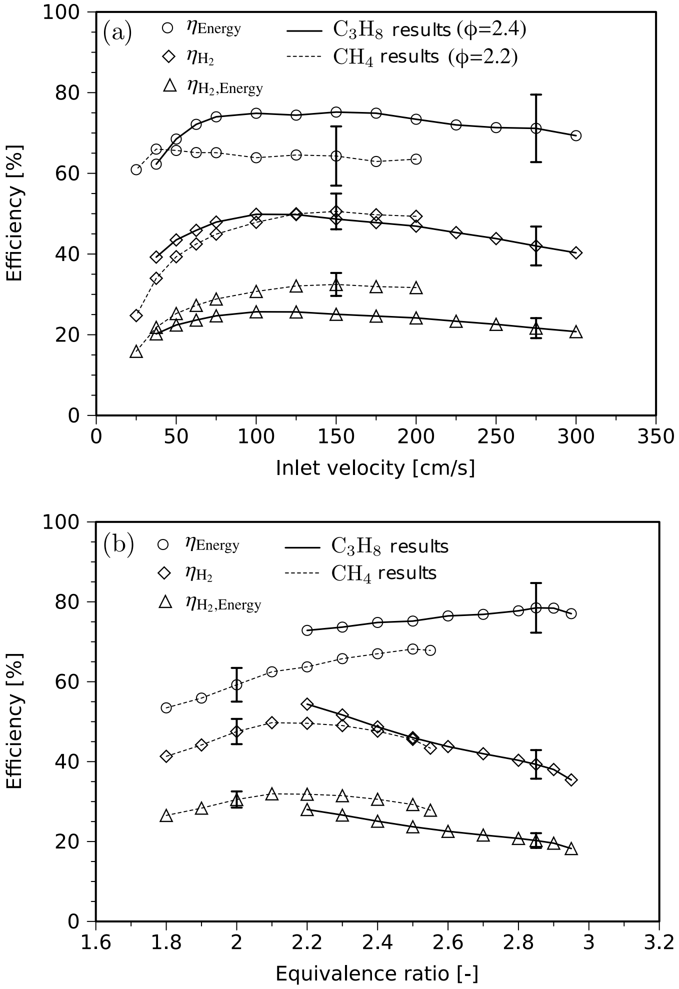

Figure 3.21: Conversion efficiencies: (a) variation of velocity at constant ϕ; (b) variation of equivalence ratio at *u*=125 cm/s.

zones in the case of the filtration reactor. This is consistent with lower concentrations of intermediate hydrocarbon species in the filtration reactor, indicating a more complete break-down of the initial fuel.

The hydrogen energy conversion efficiency is related to $\eta_{\mathrm{H_2}}$ by a scaling factor, which, however, depends on the choice of fuel. Methane contains more hydrogen atoms per carbon atom than propane, resulting in a lower $\eta_{\mathrm{H_2,Energy}}$ for propane. A variation of inlet velocities yields a peak efficiency for reforming of propane at 25.7%, compared to 32.5% for methane.

A comparison of the total energy conversion efficiency, η_{Energy}, generally shows a higher efficiency for propane reforming than for reforming of methane. For a variation of u, results for methane show a η_{Energy} between 60-65% for all but the lowest velocities, whereas those for propane show a broad peak of approximately 75% efficiency between 75 and 175 cm/s (Fig. 3.21a). The lower efficiencies for methane are attributed to higher reactor temperatures in methane reforming (Fig. 3.20), resulting in larger heat losses. Fig. 3.21b illustrates that the energy efficiency increases for increasing ϕ. This is expected, as mixtures become exceedingly oxygen-starved, and a smaller portion of the chemical energy bound in the fuel is utilized to drive the combustion process. At the same time, reactor temperatures decrease, which reduces overall process losses.

Figure 3.22 illustrates the distribution of chemical input energy that is retained by different product species in methane reforming, complementing results for energy conversion efficiencies shown in Fig. 3.21. In all cases, CO and H_2 account for the majority of the chemical energy of the syngas, where the contribution of H_2 exceeds that of CO. Under most conditions, the contributions of small hydrocarbon species – C_2H_2, CH_4 and C_2H_4 – is small. As u decreases, however, unreacted CH_4 as well as C_2H_2 increase significantly (Fig. 3.22a). Likewise, the energy content of small hydrocarbon species increases as ϕ is increased, which decreases the amount of energy bound in both H_2 and CO (Fig. 3.22b).

Figure 3.23 corresponds to Figure 3.22, where the distribution of chemical input

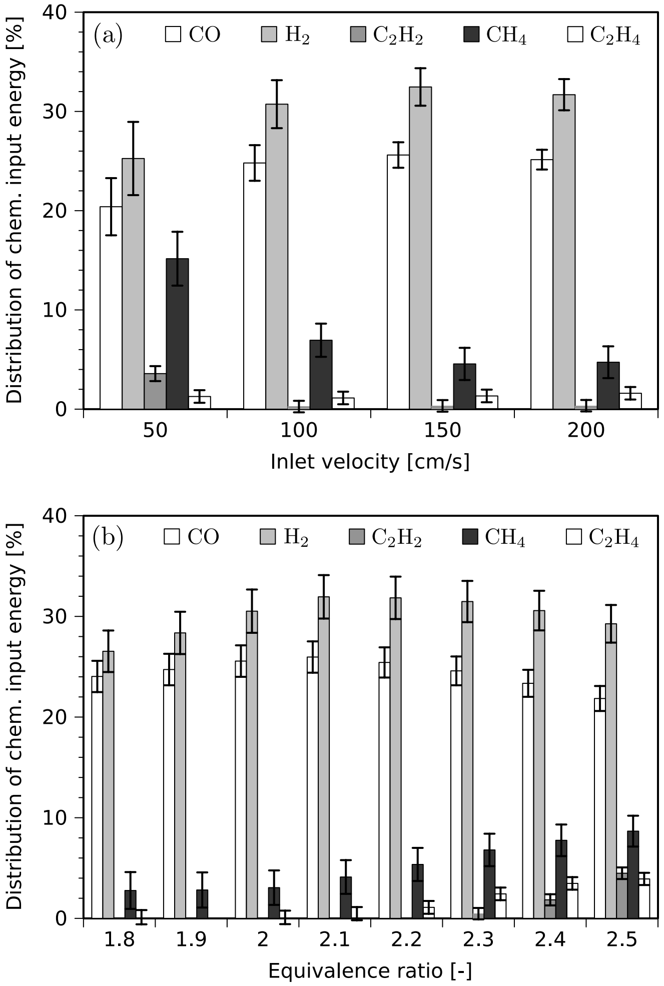

Figure 3.22: Distribution of chemical input energy retained by product species in reforming of methane: (a) variation of velocity at ϕ=2.2; (b) variation of equivalence ratio at *u*=125 cm/s.

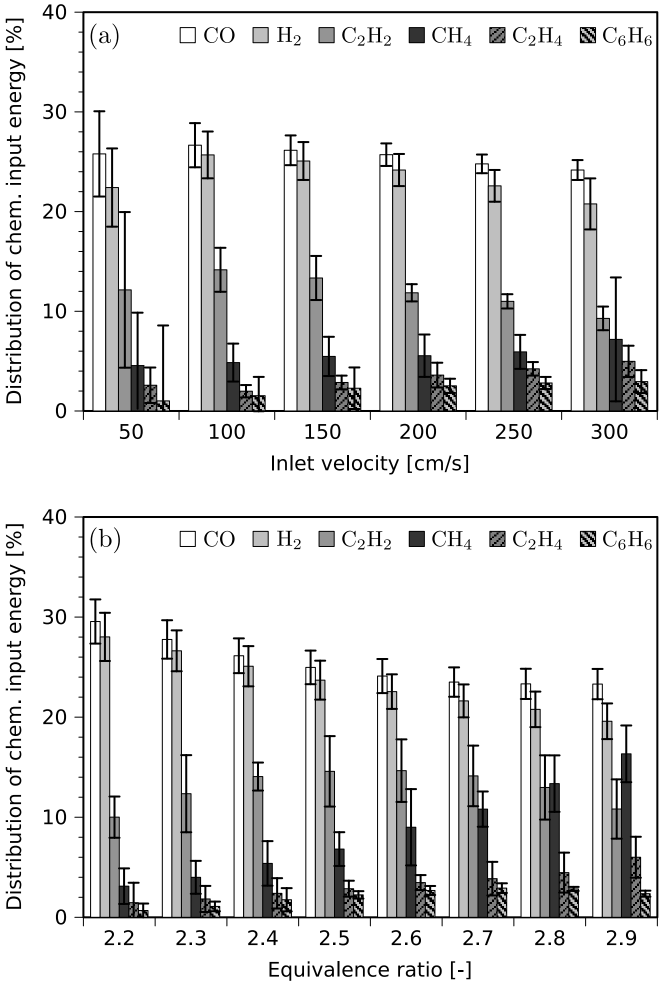

Figure 3.23: Distribution of chemical input energy retained by product species in reforming of propane: (a) variation of velocity at ϕ=2.4; (b) variation of equivalence ratio at u=125 cm/s.

energy is shown for the case of propane. Again, CO and H_2 account for the majority of the chemical energy of the syngas, although for propane the contribution of CO slightly exceeds that of H_2. Although molar concentrations of C_2H_2, CH_4, C_2H_4, and C_6H_6 are substantially smaller than than those of H_2 and CO, their contribution to the energy content of the syngas is significant at all examined conditions. This becomes particularly evident for a variation of ϕ, where the contributions of both H_2 and CO decrease with increasing ϕ. At ϕ=2.9, CH_4 accounts for 16.3% of the chemical input energy, which is just slightly lower than energy bound in H_2 at 19.6%.

3.6 Summary

Results presented in this chapter constitute the first experimental verification of non-catalytic reforming of a hydrocarbon fuel into hydrogen-rich syngas using a novel reactor design with stationary reaction zones. Combustion of a fuel-rich premixed methane/air mixture occurs inside adjacent channels with opposing flow directions. Heat transfer across walls separating hot exhaust and cold reactants stabilizes combustion in stationary reaction fronts, which allows for a continuous operation of a practical fuel reformer. In contrast, most previously studied non-catalytic reforming techniques are based on concentration of excess enthalpy in propagating combustion zones (Dhamrat and Ellzey, 2006; Fay et al., 2005; Kennedy et al., 2000; Dixon et al., 2008), where the fuel reforming process has to be restarted once the combustion zone leaves the reactor.

Temperature measurements show that wall temperatures were consistently higher than adiabatic equilibrium temperatures predicted by equilibrium calculations. Thus, significant increases of the combustion temperatures were accomplished without external heating, which illustrates the efficiency of heat-recirculation between channels in counter-flow configuration.

Stable combustion of premixed methane/air mixtures was sustained for equivalence ratios between 1.8 and 2.5, which lie beyond the conventional rich flammability limit at ϕ = 1.7 (Glassman, 1996). In comparison, tests with propane/air mixtures showed stable combustion for equivalence ratios between 2.2 and 2.9, which extend beyond the rich flammability limit of propane at 2.7 (Glassman, 1996). For both fuels, possible inlet velocities were substantially higher than those typical for conventional premixed combustors, where peak inlet velocities were limited by hardware constraints at 25 cm/s for methane and 300 cm/s for propane. The lowest flow rates were sustained at 25 cm/s and 37.5 cm/s for methane and propane, respectively. In both cases, the large difference between highest and lowest possible inlet velocities results in an excellent turn-down ratio for practical applications.

In experiments with methane, measurements of syngas concentrations showed peak H_2 levels of 18% at $u = 125$ cm/s and $\phi = 2.4$, which is comparable to published results from non-catalytic reforming in filtration waves (Fay et al., 2005; Dhamrat and Ellzey, 2006). In parameter variations of ϕ and u reactor wall temperatures exceeded the adiabatic equilibrium temperature for most cases except those close to flash-back or extinction. Reactor wall temperatures below the adiabatic equilibrium temperature coincided with decreased H_2 concentrations, which demonstrates that superadiabatic temperatures are favorable for non-catalytic fuel reforming.

Measurements with propane/air mixtures were conducted downstream of inner and outer channels of a four-channel reactor, where syngas concentrations downstream of an inner channel showed peak H_2 levels of 16.7% at u=125 cm/s and ϕ=2.4, whereas peak levels obtained for an outer channel were lower at 14.5%. Also, hydrogen levels were somewhat lower than results from methane reforming. In reforming of propane, concentrations of CO slightly exceeded those of H_2 with peaks at 17.2%, whereas in methane reforming, the situation was reversed. A further comparison to methane results revealed significant differences, where most notably reforming of propane produced significant amounts of intermediate C_2 species. While C_2 species were also found in methane reforming, concentrations were typically lower as they are synthesis products rather than intermediate products of an incomplete fuel break-down.

At $u = 125$ cm/s and $\phi = 2.2$, the total energy conversion efficiency was 66%, whereas the energy efficiency for conversion to hydrogen was 30%. At u=125 cm/s, typical total energy conversion efficiencies were about 65% for methane, and 75% for propane, whereas the energy efficiencies for conversion to hydrogen were 32.5% and 25.7%, respectively. In terms of molar hydrogen conversion, both methane and propane showed similar peak results, where about 50% of hydrogen bound in the fuel was extracted. The molar hydrogen conversion for the counter-flow reactor prototype was, however, lower than earlier results obtained for a filtration reactor, an alternative non-catalytic concept with propagating combustion zones. Here, tests for *n*-heptane as the fuel yielded close to 80% conversion at similar conditions (Dixon et al., 2008). The difference between the reactor concepts is attributed to longer residence times in high temperature zones in the case of the filtration reactor, resulting in a more complete break-down of intermediate hydrocarbon species. While residence times are mainly a function of channel length and flow velocity, analytical results from a simplified model predict that characteristics of the high temperature zone can be adjusted by tuning both reactor geometry and the conductivity of the wall material (Chapter 2).

Results from experiments with methane and propane show that the reformer design is fuel-flexible, where the use of larger hydrocarbon species as fuel feedstocks for fuel reforming purposes appears possible. Over a total operating time of approximately 150 hours, no deterioration of the reactor performance was observed under normal operating conditions, which indicates that the non-catalytic reformer design offers a robust alternative to conventional catalytic reformers.

Chapter 4

Numerical Model

The objective of the numerical study is the investigation of reaction zone characteristics typical for reforming of rich methane/air mixtures that are not accessible by experimental techniques. An outline of the numerical model as well as detailed results are discussed below; further details on the implementation of the numerical model are given in Appendix D.

4.1 Solution Method

In this study, the general-purpose computational fluid dynamics (CFD) code FLUENT 6.3 was used (Fluent Inc., 2006). The CFD code solves incompressible Navier-Stokes equations and conservation equations for energy and species with detailed reaction chemistry. In transient simulations, conservation equations are modeled as follows (Fluent Inc., 2006): mass and momentum are given by

$$\frac{\partial \rho_f}{\partial t} + \nabla \cdot \left(\rho_f \vec{u}\right) = 0 \tag{4.1}$$

$$\frac{\partial \left(\rho_f \vec{u}\right)}{\partial t} + \nabla \cdot \left(\rho_f \vec{u}\vec{u}\right) = -\nabla p + \nabla \cdot \bar{\tau} + \vec{F} \tag{4.2}$$

where ρ_f is the density of the fluid, $\vec{u}$ is the velocity vector and p is the static pressure. The stress tensor is defined $\bar{\tau} = \mu_f \left[\nabla\vec{u} + \nabla\vec{u}^T - \frac{2}{3}\nabla \cdot \vec{u}I\right]$, with the viscosity μ_f and the unit tensor I, and $\vec{F}$ represents a volumetric force term such as viscous forces within porous media.

Depending on whether the energy equation is solved for a fluid or a solid, one of the two following equations is used:

$$\frac{\partial\left(\rho_f E\right)}{\partial t} + \nabla \cdot \left(\vec{u}\left(\rho_f E + p\right)\right) = \nabla \cdot \left(k_f \nabla T - \sum_i h_i \vec{J}_i\right) + S_{h,f} \tag{4.3}$$

$$\frac{\partial\left(\rho_s h_s\right)}{\partial t} = \nabla \cdot \left(k_s \nabla T\right) + S_{h,s} \tag{4.4}$$

where compressibility effects and viscous heating are neglected. Here, $E \equiv h - p/\rho_f + u^2/2$, where the sensible enthalpy is defined for incompressible flow as $h = \sum_i Y_i h_i$, with Y_i being the local mass fraction of a chemical species i. The first two terms on the right hand of Eq. 4.3 side represent energy transfer due to conduction and species diffusion. The diffusion flux of species i is given by $\vec{J}_i = -\rho_f D_{i,m} \nabla Y_i$, where $D_{i,m}$ is the diffusion coefficient in the mixture. Furthermore, the source terms S_h include the heat of chemical reactions and user specified volumetric heat sources.

The conservation equation for Y_i, the local mass fraction of a chemical species i, is given by the equation

$$\frac{\partial\left(\rho_f Y_i\right)}{\partial t} + \nabla \cdot \left(\rho_f \vec{u} Y_i\right) = -\nabla \cdot \vec{J}_i + R_i \tag{4.5}$$

The net rate of creation/destruction of chemical species i, R_i, is computed as the sum of the Arrhenius-type reaction source terms over the N_R reactions, i.e. $R_i = M_{w,i} \sum_r \hat{R}_{i,r}$, where $M_{w,i}$ is the molecular weight and $\hat{R}_{i,r}$ represents the molar creation/destruction rate of species i in reaction r . With a low Mach number, the flow is is assumed to be incompressible with pressure variations that are negligible when compared to the atmospheric pressure. Thus, the ideal gas law is approximated as $\rho_f = p_0/\left(RT/M_w\right)$, where p_0 is a constant “operating” pressure, R is the universal gas constant and M_w is the molecular weight of the gas.

Detailed chemistry is handled by built-in FLUENT 6.3 functions up to a maximum number of 50 species. Among suitable reaction mechanisms, GRI-Mech 2.11 with 277 elementary chemical reactions and 49 species was chosen (Bowman et al., 1995), as it includes the most detailed reaction chemistry handled by the CFD code.

In transient simulations, the pressure-velocity coupling is handled by the SIMPLE algorithm, a semi-implicit method for pressure linked equations (Caretto et al., 1972). For time-stepping, a first-order implicit scheme is used, whereas in the spatial dimensions, a first order up-winded discretization scheme is used for the initial transient and a second order up-winded scheme is used for the final solution. Also, the computational mesh is locally refined at locations with rapidly changing solution variables, where additional elements are defined via a hanging node adaptation strategy (Fluent Inc., 2006).

4.1.1 Computational Model

The computational model approximates the configuration of a counter-flow reactor used in the experimental part of the study (Chapter 3). While the reactor used in experiments consists of four flow channels, the computational model assumes an infinite number of parallel channels, where symmetries of the computational domain are used to reduce the computational effort. Figure 4.1a shows a 2D slice across a reactor with multiple, 4 mm high flow channels with alternating flow directions, where channels are separated by 1 mm thick walls. Using symmetries, the computational domain can be reduced to one half-channel, shown in Figure 4.1b. For a semi-infinite domain, solutions are symmetric around the channel center line $y = 0$, i.e. for any scalar solution variable $f(x, y) = f(x, -y)$. In addition, the solutions are symmetric around the center of the reactor at $x = 0$ with an offset of the channel separation h, i.e. $f(x, y) = f(-x, y + h)$. Thus, the overall solution can be reconstructed from the solution of one half-channel.

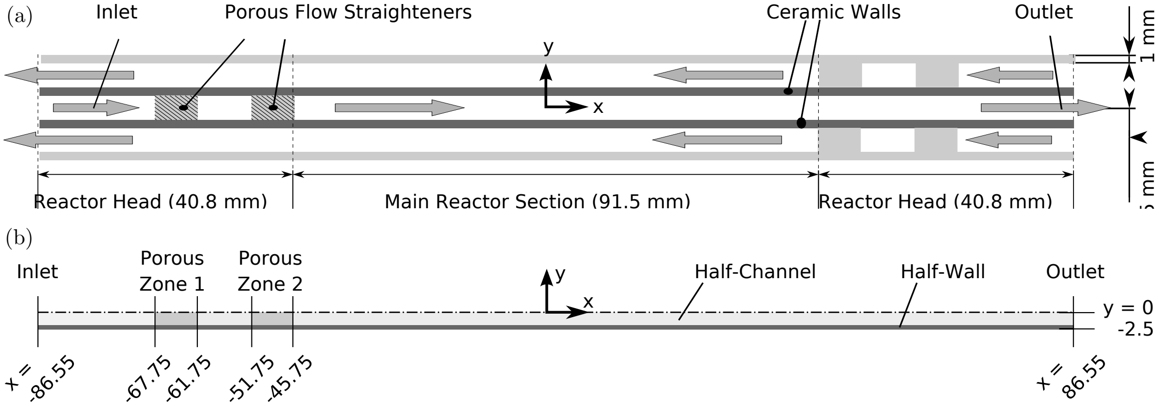

Figure 4.1: Counter-flow reactor: (a) geometry; and (b) computational domain.

The boundary conditions used for the simulations are a prescribed normal velocity u_{in} and mixture composition at the inlet ($x = -86.55$ mm), and atmospheric pressure at the outlet ($x = 86.55$ mm). The boundary at $y = 0$ is given by symmetry in the y-direction, whereas symmetric wall temperatures are forced as $T_w(x, -2.5) = T_w(-x, -2.5)$ in a user defined function (UDF). Finally, wall boundaries at both channel ends are modeled by radiative boundary conditions where the emissivity of the walls is assumed as 0.85. Further details on UDF's are given in Appendix D.

Property data of the fluid zone within the reactor channels are obtained from thermodynamic data included in GRI-Mech 2.11. Materials properties of the channel walls are chosen to match manufacturer's specifications for silicon carbide (SiC) used in experiments, with a heat capacity of 670 J/kg-K and a high-temperature conductivity extrapolated to 50 W/m-K. Characteristic times for fluid flow through channel and reaction layer are in the order of 17.3 ms and 0.2 ms, respectively, which are based on typical flow velocities of 10 m/s, a channel length of 173.1 mm and an estimated reaction layer thickness of 2 mm. Since the time constant for 1 mm thick SiC walls is significantly larger, the wall density is artificially reduced to reduce the simulation time required to attain steady-state conditions. A density reduction by a factor of 100 to 31 kg/m^3 results in a characteristic time of $\tau_w \approx 56$ ms, based on a channel height of 4 mm, Nu≈ 8 and assuming a gas conductivity of 0.093 W/m-K.

The reactor head contains two porous flow-straighteners, creating two fluid domains within the reactor head, and the main reactor section between x=-45.75mm and x=86.55 (Fig. 4.1). In FLUENT 6.3, the effect of porous domains on fluid dynamics is treated by an artificial viscous resistance term (3.846×10^7 $1/\mathrm{m}^2$) (Fluent Inc., 2006). Furthermore, the CFD code assumes a single temperature for fluid and porous solid, where conductivity and heat capacity are adjusted according to the porosity of the zone. In computations, the porosity of the porous zone was set to 0.92, according to silicon carbide flow straighteners used in experiments. Heat transfer between porous zone and wall is treated by a UDF modeling a contact resistance as $q = h_c \Delta T$, with $h_c \approx 1000$ W/m^{2}K (Mills, 1999). External heat losses are simulated by an additional user defined function (UDF) modeling a volumetric heat loss term along the wall as $q = -h_\infty (T_w - T_\infty)$. Here, external heat transfer coefficient and temperature of the environment were assumed as h_∞=11200 W/m^{2}K and T_∞=300 K, respectively, which corresponds to external heat losses in the order of 20% of the chemical input energy at ϕ=2.2 and u_{in}=125 cm/s.

Radiative surface-to-surface heat transfer in the symmetric channel segments between channel inlets, porous media zones, and channel outlet is modeled by a UDF solving for radiative heat fluxes between wall elements (Appendix D).

4.1.2 Computational Approach

The spatial discretization of the equations is based on a structured mesh that is subsequently refined once the solution approaches steady state conditions. In the horizontal direction, the domain between $x = -45.75$ and 86.55 uses 300 elements, resulting in an axial grid spacing of 0.441 mm. Porous zones and channel segments upstream of $x = -45.75$ are resolved by a coarser mesh. In the vertical direction, the initial mesh uses 12 elements with decreased element heights at bottom and top of for the fluid domain for half the channel height, and three elements to resolve half the wall thickness, yielding an average vertical grid spacing of 0.167 mm. In transient simulations,

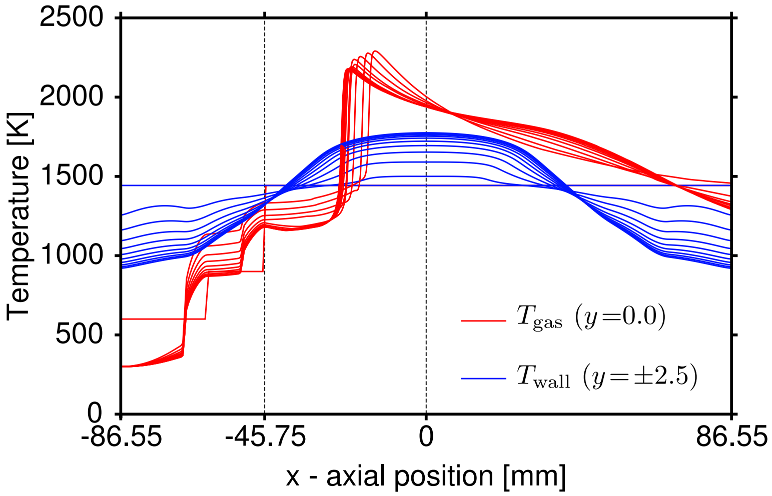

(a) Initial transient solution (base mesh).

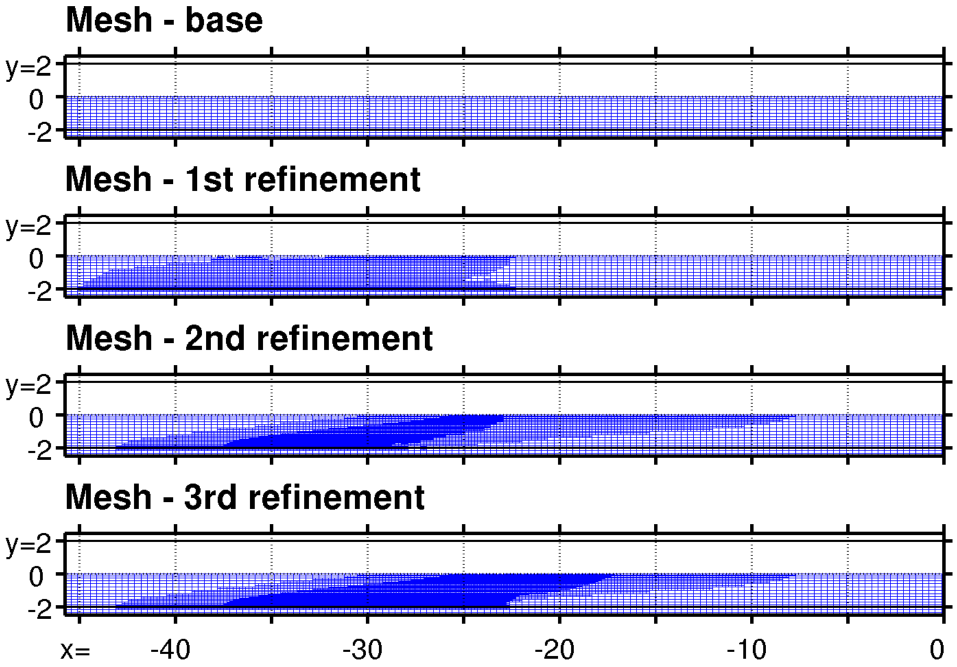

(b) Computational mesh (detail).

Figure 4.2: Computational model: (a) initial transient; (b) adjustments of computational grid.

solutions are advanced in fixed time-steps of $t = 10^{-5}$ s (0.01 ms).

Figure 4.2a illustrates the initial transient for temperature profiles along channel and wall center at y =0 and –2.5 respectively. The initial wall temperature is set to

1442.83 K, the adiabatic equilibrium temperature for methane/air mixtures at ϕ=2.2. In order to prevent auto-ignition throughout the gas phase at T=1442.83 K, the initial composition downstream of the porous zones is set to pure nitrogen. Upstream of the main reactor section, initial gas temperatures are reduced to 900 K (x<-45.75), and 600 K (x<-61.75), and the initial gas composition was set equal to the inlet conditions. Together, this approach resulted in an orderly auto-ignition process that established the reaction zone. Solutions are shown at an interval of 20 ms for a simulations over 200 ms, where profiles clearly indicate that a steady state solution is approached: during the initial transient, wall temperatures increase around x=0, whereas they drop at both ends at ±86.55 mm. Gas temperatures show that reaction zones, marked by steep temperature increases close to the temperature peaks, are established quickly, but stay around the same location. The two steep temperature increases upstream of $x = -45.75$ are caused by increased heat transfer in porous zones.

Once the transient solution is close to steady state, the computational mesh is refined to increase the quality of the numerical solution around the reaction zone (Fig. 4.2b). In a first adaptation, the zone upstream of the reaction zone is refined by subdividing individual elements into four parts, and transient solutions are continued for 20 ms. In a second adaptation, the mesh is refined in regions downstream of the reaction layer, the inner reaction layer is further subdivided, and simulations are run for another 10 ms. In a third grid adaptation, the mesh is adjusted and simulations are continued for 20 ms to a total simulation time of 250 ms. After the third grid adaptation, the spatial discretization scheme is changed from first-order upwind to second-order upwind, and simulations are run for an additional 30 ms. The last step was undertaken to obtain an improved solution for a grid-dependence study, detailed in Section 4.1.3. After the 2nd grid adjustment, the grid spacing of the most refined zones is 0.11 mm in x-direction, and approximately .042 in the y-direction. In the following, all results are shown for 28000 time-steps (i.e. 280 ms).

Table 4.1: Grid dependence of temperature deviations as function of local refinement levels in zones upstream and downstream of the reaction layer.

Grid	discretization	upstream zone	downstream zone	$\|\|\Delta T\|\|_{L_2}$
Base grid	1^{st}-order up-winded	unrefined	unrefined	16.93
Adaptation 1	1^{st}-order up-winded	1 level	unrefined	10.27
Adaptation 2	1^{st}-order up-winded	2 levels	1 level	22.85
Adaptation 3	1^{st}-order up-winded	2 levels	2 levels	6.28
Reference	2^{nd}-order up-winded	2 levels	2 levels	N/A

4.1.3 Grid Dependence

The objective of grid adaptations is to improve the quality of the solution. In the following, the impact of the computational grid on the numerical results is using an L_2 norm of the local temperature deviation,

$$||\Delta T||^2_{L_2} = \frac{1}{n}\sum_{i=1}^{n}\Big(T_k\left(t, x_i, y_i\right) - T_{ref}\left(t, x_i, y_i\right)\Big)^2 \tag{4.6}$$

where n is the number of grid points $\langle x_i, y_i \rangle$ of the coarsest grid, t is the simulation time, T_k is the temperature result obtained from the k-th adjustment, and T_{ref} is the temperature obtained for the highest quality simulation, which increases the quality of the solution by using a superior discretization scheme for the evaluation of gradients.

Table 4.1 shows results of the error norm defined in Eq. 4.6, where all results are evaluated at t=280 ms and operating conditions ϕ=2.2 and u_{in}=125 cm/s. In each refinement step, quadrilateral grid elements are partitioned into four sub-elements whenever a threshold based on a solution property is exceeded; the refinement level specifies how often an element of the coarsest grid was sub-divided. Results show that the first grid adaptation results in an improvement, whereas the second adaptation does not. The decrease of the solution quality between adaptation 1 and adaptation 2 is explained by the impact of the grid refinement on the position of the reaction layer, which shifts downstream, out of the zone with two levels of refinement. The third grid adaptation corrects this by using equal levels of refinement for regions upstream and

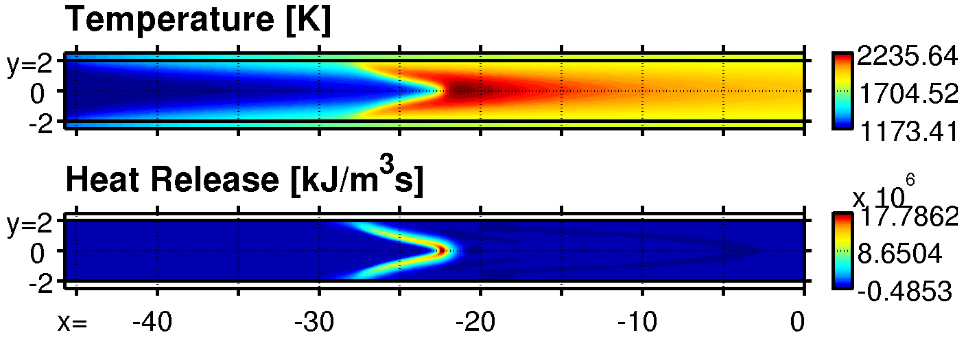

(a) Temperature and heat release.

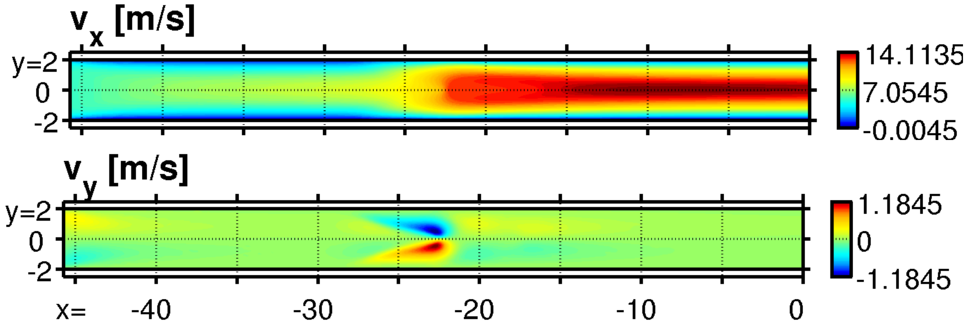

(b) Flow velocities in x- and y-direction.

Figure 4.3: Overview of temperature and velocity results for combustion of methane/air mixtures at ϕ=2.2 and u_{in}=125 cm/s. Flow direction is left-to-right; all figures show channel segment between porous zone 2 and reactor center.

downstream of the reaction layer, which is reflected by a decrease of the error norm. In the following, all simulation results are based on the highest quality solution, i.e. two levels of local grid refinement upstream- and downstream of the reaction layer, and a 2^{nd}-order up-winded discretization scheme.

4.2 Results and Discussion

Figure 4.3 illustrates simulation results for an equivalence ratio ϕ=2.2 and inlet velocity u_{in}=125 cm/s, where the channel segment between porous zone 2 at $x = -45.75$ mm and reactor center at x=0 mm is shown (Fig. 4.1). The porous zone acts as a flow

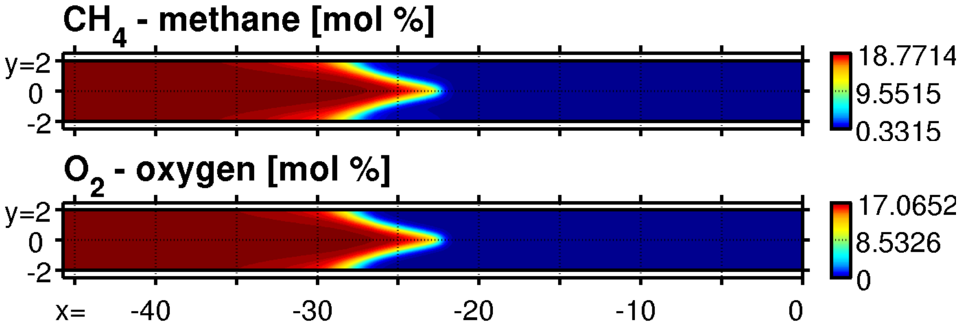

(a) Reactant species.

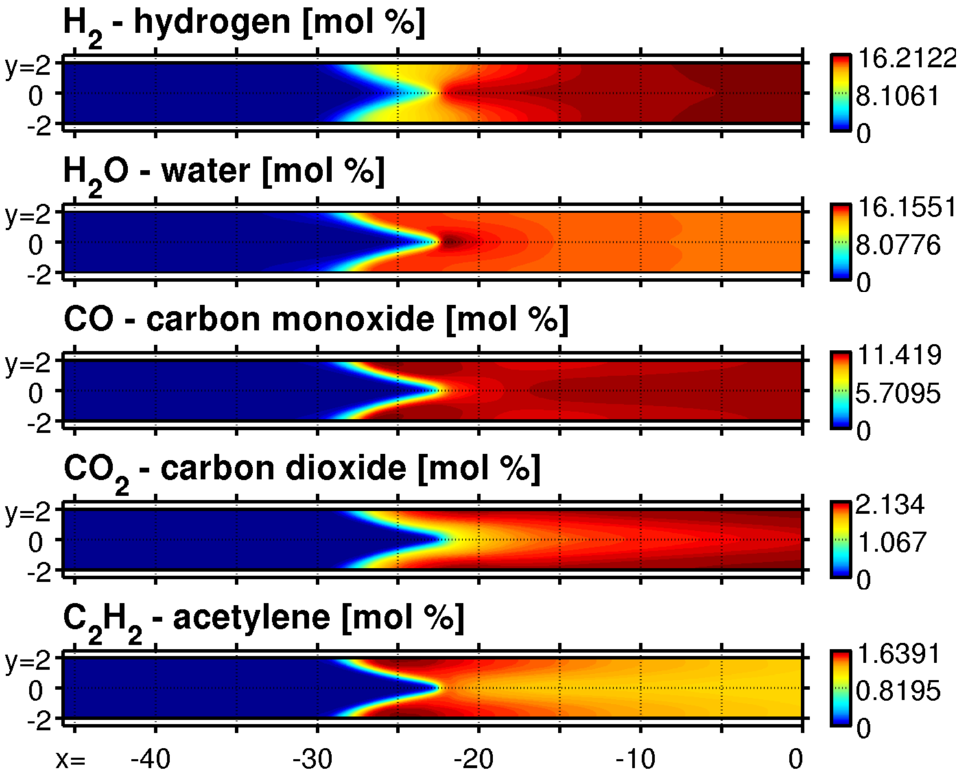

(b) Product species.

Figure 4.4: Overview of reactant- and major product species for combustion of methane/air mixtures at ϕ=2.2 and u_{in}=125 cm/s. Flow direction is left-to-right; all figures show channel segment between porous zone 2 and reactor center.

straightener, forcing plug-flow in the x-direction at $x = -45.75$, after which temperature results (Fig. 4.3a) and velocity results (Fig. 4.3b) show the development of boundary layers for $x \lesssim -28$ mm. Results for the heat release reveal a thin tulip shaped reaction layer , resulting in a rapid increase of temperature and u_x (Fig. 4.3a/4.3b). Using axial locations with maximum heat release along wall and channel center line, the reaction layer extends between $x = -27.9$ and -22.4 mm. Furthermore, the reaction zone thicknesses along wall and center line, defined as the length of the region where the heat release along a streamline exceeds 10% of its peak value, are 2.8 and 1.5 mm, respectively. Downstream of $x \approx -20$, temperatures decrease as heat is transferred to the channel walls and velocity boundary layers re-establish. In addition, results for u_y show a nozzling effect created by the reaction zone, where the flow is pushed towards the channel center by expanding gases (Fig. 4.3b). In the region downstream of the porous zones (x>-45.75), the pressure drop is 45.4 Pa, whereas the pressure drop between channel inlet and outlet is 163 Pa.

Results for reactant species concentrations show that while O_2 is consumed completely, a small amount of CH_4 is found downstream of the reaction zone (Fig. 4.4a). Figure 4.4b shows concentrations of species found in the product stream. While H_2 forms quickly at the reactor center, gradients along the walls are less steep, which is attributed to slower reactions at lower temperatures as well as increased up-stream diffusion in a low-velocity region. H_2O as well as CO show a steep increase across the reaction layer. In addition, H_2O concentrations peak at the channel center directly downstream of the reaction layer ($x \approx -22$), where the subsequent decrease is due to steam reforming (Dixon et al., 2008). In comparison to the rapid formation of CO, the further oxidation to CO_2 completes in a slower process downstream of the reaction layer. Apart from the species mentioned above, the only other product predicted with significant quantities at the exit is C_2H_2, where the highest concentrations are observed close to the walls. The heightened concentrations along the walls are attributed to differences in the reaction processes between the central parts of the channel and regions close to the walls, and is discussed below.

4.2.1 Fuel Breakdown

One of the advantages of using methane as a research fuel is its well known chemistry (Warnatz, 1981; Law, 2006). Figures 4.5 and 4.6 illustrate the fuel breakdown, including the current understanding of methane combustion (Fig. 4.6a), as well as selected species forming along different reaction pathways (Fig. 4.6b).

The breakdown of methane is typically initiated by an H-abstraction reaction through a radical attack by either O, H, or OH as

$$\mathrm{CH_4 + (O, H, OH) \rightleftharpoons CH_3 + (OH, H_2, H_2O)} \tag{4.7}$$

Figure 4.5a shows creation rates of CH_3, as well as creation rates of the radicals involved in reaction 4.7. All radical species start to be created with significant rates close to the wall around $x \approx -275$, after which zones with high creation closely match the tulip-shaped reaction layer revealed by the peak heat release (Fig. 4.3a). Creation rates peak at the channel center, which is due to the necessity to produce more radicals per time to sustain combustion in a region with increased flow velocities.

Figure 4.5b shows evidence of an alternative chain initiation mechanism, where the onset of HO_2 close to the walls is further upstream at $x \approx -29$. The mechanism most likely to be responsible is a pre-ignition reaction typical for auto-ignition,

$$\mathrm{CH_4 + O_2 \rightleftharpoons CH_3 + HO_2} \tag{4.8}$$

which is followed by the chain carrying reaction

$$\mathrm{CH_4 + HO_2 \rightleftharpoons CH_3 + H_2O_2} \tag{4.9}$$

producing an additional CH_3 radical and H_2O_2 (Law, 2006). Accordingly, local concentrations of H_2O_2 peak upstream of the tulip-shaped reaction layer close to the walls (Fig. 4.5b), where H_2O_2, although highly reactive, accumulates.

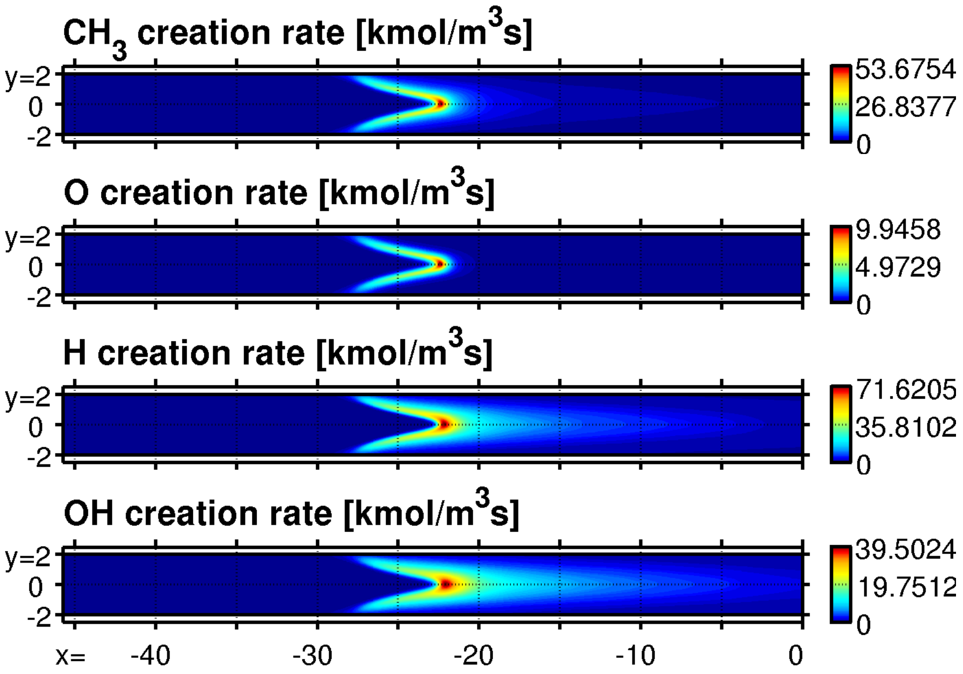

(a) Creation rates of species involved in initial fuel breakdown.

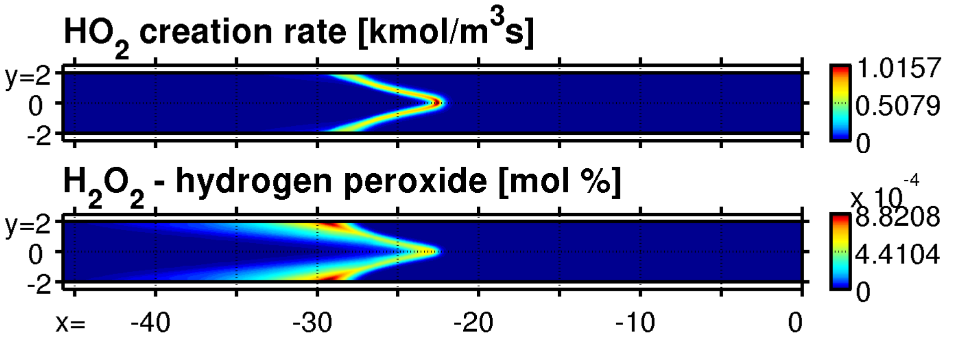

(b) High concentration of H_2O_2 marks pre-ignition zone.

Figure 4.5: Species involved in initial fuel breakdown.

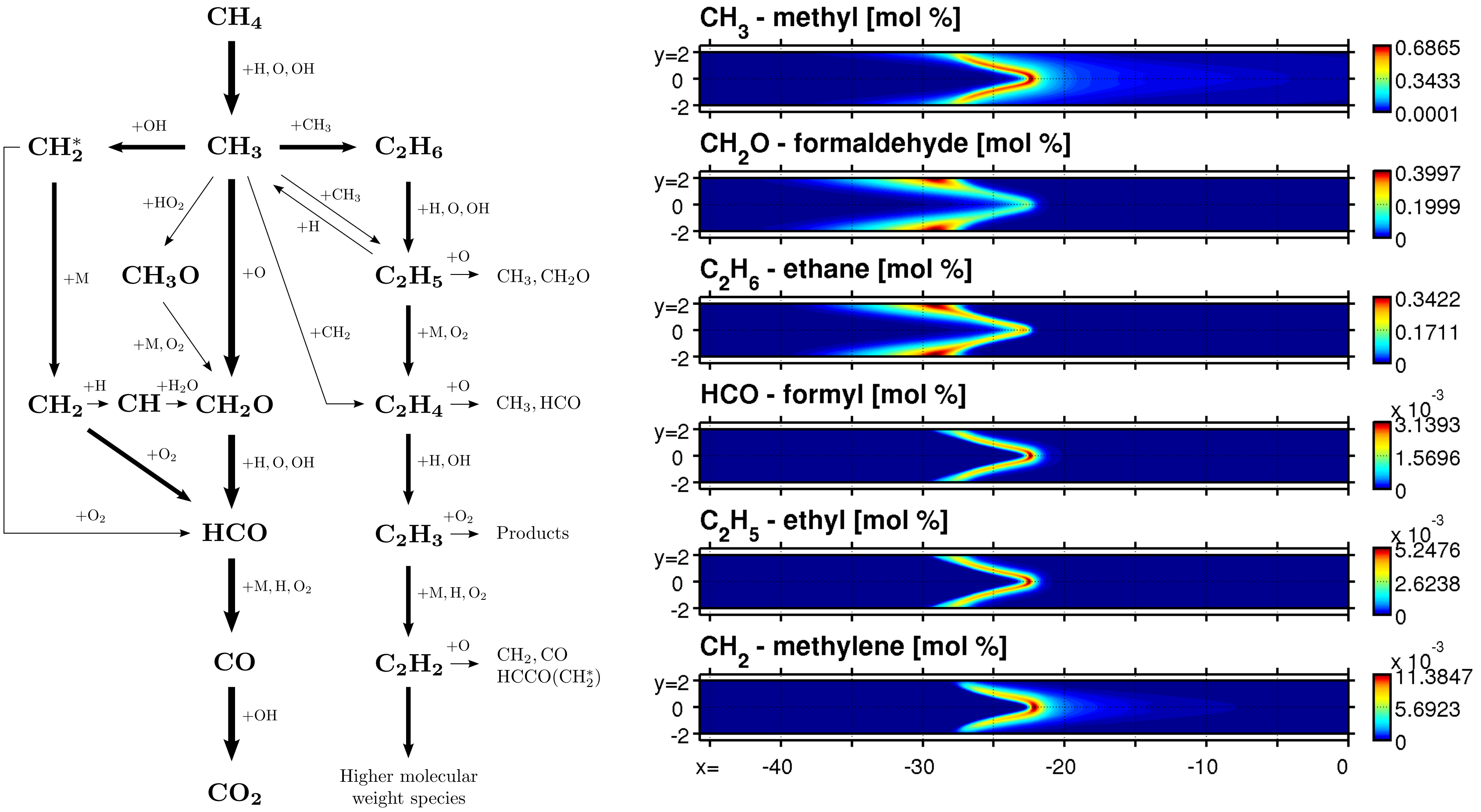

(a) Reaction pathways.

(b) Selected species.

Figure 4.6: Fuel breakdown: (a) reaction pathways in methane combustion (adapted from); (b) selected species forming during methane combustion: CH_3 is created from H-abstraction of methane; CH_2O and C_2H_6 accumulate in pre-ignition zones along walls ($x \approx -29$ mm, $y = \pm 2$ mm); HCO and C_2H_5 peak within reaction layer; and CH_2 shows highest concentrations in central combustion zone ($x \approx -22$ mm, $y \approx 0$ mm).

Further evidence for zones dominated by pre-ignition chemistry along the walls upstream of the tulip-shaped reaction layer is shown in Figure 4.6b, which illustrates concentrations of selected species produced along different reaction pathways (Fig. 4.6a). In pre-ignition, CH_3 reacts with molecular oxygen in

$$\begin{aligned} CH_3 + O_2 &\rightleftharpoons CH_2O + OH && (4.10a) \\ &\rightleftharpoons CH_3O + O && (4.10b) \end{aligned}$$

where the former reaction is chain carrying, and the latter is chain branching (Law, 2006). Similar to H_2O_2, concentrations of CH_2O show an accumulation upstream of the reaction layer (Fig. 4.6b). Also, high concentrations of C_2H_6 in the same regions point at the chain termination reaction

$$CH_3 + CH_3 + M \rightleftharpoons C_2H_6 + M \tag{4.11}$$

which inhibits ignition. Together, the accumulation of H_2O_2, CH_2O, and C_2H_6 upstream of regions with high radical creation rates (Figs. 4.5a/4.6b) corroborates the existence of pre-ignition zones along the walls at $x < -28$, which is further substantiated by high concentrations of methanol.

Once chain branching is initiated and ignition occurs, CH_2O forms the highly reactive HCO radical, which peaks in a thin tulip-shaped reaction layer as it quickly reacts to CO. Similarly, C_2H_5 peaks in the reaction layer before forming C_2H_4 and C_2H_2 (Fig. 4.6). In an alternative reaction path, CH_3 reacts to CH_2 before forming HCO. Concentrations of CH_2 peak in the center of the channel at $x \approx -22$ (Fig. 4.6b), which is also the location where peak combustion temperatures are observed (Fig. 4.3a).

Altogether, numerical simulations reveal a two-dimensional reaction zone. The combustion process is initiated by ignition at the hot channel walls. The ignition zones are connected to a central reaction zone by a thin oblique reaction layer, forming a tulip-shaped structure.

4.2.2 Impact of Operating Conditions

Figure 4.7 illustrates the impact of changes in equivalence ratio and inlet velocity on characteristic temperature profiles within the channels. Results from the one-dimensional analytical model predicts that for rich combustion, reaction zones move towards the reactor center at $x = 0$ as either equivalence ratio or inlet velocity are increased (Chapter 2). As a comparison, Figure 4.7a shows changes of reaction zone locations with changing equivalence ratios for the detailed numerical model. One-dimensional temperature profiles plotted for center of wall and channel at $y = 0$ and ± 2.5, respectively, show reaction zones that are marked by a sharp increase of gas temperatures. As predicted, the reaction zones move closer to the reactor center as ϕ is increased from 1.9 to 2.2 and 2.5. In addition, wall temperature profiles show that the widths of the high temperature zones decrease while peak temperatures remain almost unchanged, which closely matches the behavior observed in experiments with methane/air mixtures (Chapter 2). Similarly to the behavior observed for increasing ϕ, reaction zones move toward the reactor center as the inlet velocity is increased (Fig. 4.7b). At the same time, peak wall temperatures increase, which again matches experimental observations (Chapter 2).

Two-dimensional numerical results for increasing ϕ show that points where the reaction layer attach to the wall mov towards the reactor center while the length of the tulip shape, defined as the distance between attachment points and the cusp of the reaction layer, increases. In the following, attachment points and tulip cusps are specified by the respective locations where heat release curves, plotted along streamlines on channel walls and center lines, peak. At $\phi = 1.9$, reactions are initiated at the walls at $x = -38.7$, and the length of the tulip shape is 2.6 mm, whereas at $\phi = 2.5$, reactions start at $x = -19.1$, with a length of 8.6 mm. At the same time, the reaction layer thickness at the center line, defined as the length of the region where heat release exceeds 10%

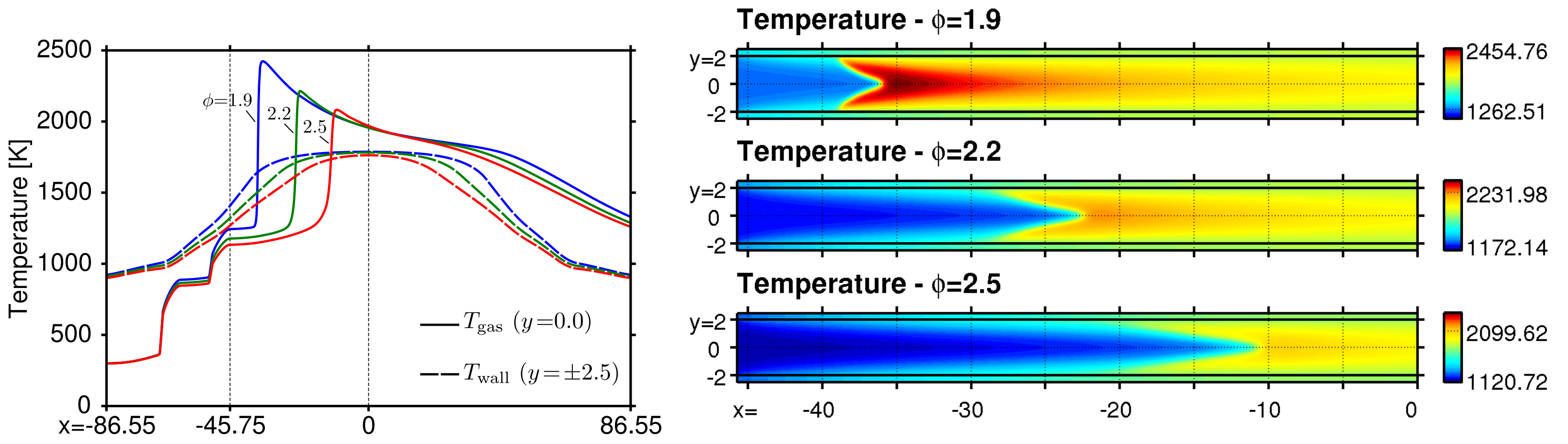

(a) Variation of equivalence ratio: (left) 1-D temperature profile along center lines of wall and gas in *x*-direction; (right) 2-D temperature plot.

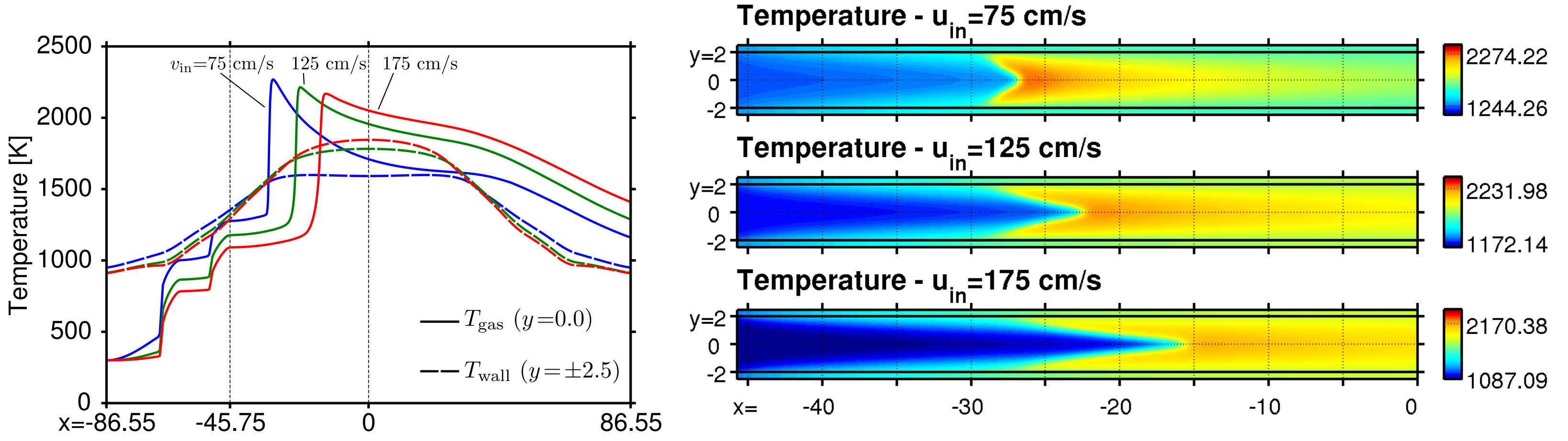

(b) Variation of inlet velocity: (left) 1-D temperature profile along center lines of wall and gas in *x*-direction; (right) 2-D temperature plot.

Figure 4.7: Temperature profiles illustrate impact of operating conditions on characteristics of the combustion zone. Tulip shapes elongate as ϕ and *u* increase, while peak temperatures decrease.

of its peak value, increases from 0.83 at ϕ =1.9 to 2.73 mm at ϕ =2.5. Similar characteristics are observed for increasing u_{in}, although the shift of the attachment points is less pronounced while the change of tulip shape length is more distinctive. At u_{in} =75 cm/s, the attachment point is at $x = -28.6$ with a length of 1.8 mm, whereas at u_{in} =175 cm/s, the reaction layer attaches at $x = -26.3$ and the length is 10.7 mm. The reaction layer thickness at the centerline increases with increasing inlet velocity, from 0.83 mm at u_{in} =75 cm/s to 2.73 mm at 175 cm/s. It is noted that the two sides of the tulip shape show some resemblance to developing boundary layers, which is particularly evident at high inlet velocities.

The changing shape of the combustion zone is important for a better understanding of characteristics of ultra-rich combustion typical for fuel reforming. In a two-dimensional process, the length of the reaction layer is variable, which influences the local mass flux. By comparison, one-dimensional models assume plug flow and do not account for variations of the reaction layer length. As a consequence, the mass flux through the reaction zone is specified by the inlet conditions. The ramifications of the model choice are especially significant for the prediction of peak combustion temperatures of stationary combustion zones. In a one-dimensional model, the reaction temperatures result from the necessity to match a specified mass flux by the local reaction rates. In a two-dimensional model, however, a lengthened reaction layer reduces the local mass flux, which allows for lower reaction rates at reduced reaction temperatures. This situation becomes evident for a comparison of numerical results to analytical predictions. While the movement of the reaction zone location and changes of peak wall temperatures are modeled correctly, the one-dimensional analytical model predicts an increase of reaction temperatures for increasing u_{in} (Chapter 2), whereas numerical results show a decrease.

Table 4.2 shows a comparison of dry syngas species concentrations at the reactor outlet for numerical simulations and experiments. In general, the data show excellent agreement, although some differences are noted for the lowest inlet velocity tested in

Table 4.2: Comparison of dry species concentrations from numerical simulations to experimental results obtained for variations of ϕ and u_{in}. Experimental values are given in parentheses.

ϕ=	1.9	2.2	2.5
H_2	16.1 (13.1)	19.0 (17.5)	19.6 (18.0)
CO	12.4 (12.0)	12.8 (14.1)	12.1 (13.6)
CO_2	3.7 (3.5)	2.6 (2.6)	2.3 (2.1)
O_2	0.0 (0.05)	<0.01 (0.06)	<0.01 (0.06)
CH_4	0.008 (0.4)	0.50 (1.0)	1.3 (1.9)
C_2H_2	0.004 (0.0)	1.2 (0.0)	2.3 (0.9)
C_2H_4	<0.01 (0.01)	0.1 (0.1)	0.2 (0.5)
C_2H_6	<0.01 (0.0)	<0.01 (0.02)	<0.01 (0.03)

(a) Variation of equivalence ratio.

u_{in}=	75 cm/s	125 cm/s	175 cm/s
H_2	18.7 (16.1)	19.0 (17.6)	18.4 (17.7)
CO	12.9 (13.3)	12.8 (14.2)	12.5 (14.2)
CO_2	2.6 (2.7)	2.6 (2.6)	2.6 (2.6)
O_2	<0.01 (0.3)	<0.01 (0.07)	<0.01 (0.04)
CH_4	0.6 (1.9)	0.5 (1.0)	0.6 (0.8)
C_2H_2	1.2 (0.1)	1.2 (0.01)	1.4 (0.2)
C_2H_4	0.1 (0.1)	0.1 (0.2)	0.09 (0.1)
C_2H_6	<0.01 (0.04)	<0.01 (0.02)	<0.01 (0.0)

(b) Variation of inlet velocity.

the numerical study, where in experiments, a degradation of the reactor performance is observed that is not present in the simulation data. In general, numerical results show slightly higher H_2 concentrations, while CO concentrations are generally underpredicted. The most significant differences are in the concentration of CH_4 and C_2H_2, both of which are predicted in significantly higher concentrations in numerical simulations. This discrepancy is explained by shortcomings of the reaction mechanism used for this study, which does not include formation of higher hydrocarbon species and soot precursors. Experimental results, however, show some evidence for the formation of aromatic hydrocarbons and other soot-precursors. Acetylene (C_2H_2) is seen as an important starting point in the formation of benzene, which itself is a precursor for polycyclic aromatic hydrocarbons (PAH) (Law, 2006). Acetylene, however, is created late in the fuel-breakdown (Fig. 4.6a) and peaks downstream of the reaction layer (Fig. 4.4b). This indicates that the formation of PAH and other higher hydrocarbons takes place in the post-combustion region. Therefore, the omission of higher hydrocarbon species is not expected to influence the reaction layer itself. A more detailed investigation of the formation of hydrocarbons in the post-combustion region, however, requires more detailed reaction kinetics that include larger hydrocarbon species and other soot-precursors (Richter and Howard, 2002; Hoyermann et al., 2004).

4.3 Summary

Simulations of a counter-flow reactor with detailed chemistry reveal the two-dimensional structure of the reaction zone resulting from rich combustion sustained by heat transfer from an adjacent combustion channel. Details of the reaction zone structure reveals that reactions start at the channel walls. Upstream of the ignition zone, the accumulation of H_2O_2, CH_2O, and C_2H_6 along the channel walls shows strong evidence for the importance of pre-ignition reactions that are typical for an auto-ignition process (Law, 2006). Once chain branching is initiated and ignition occurs on top and bottom wall of the channel, reactions occur in thin oblique reaction layers, that join at the channel center to form a tulip shaped structure.

A comparison of two-dimensional numerical results to one-dimensional analytical predictions (Chapter 2) shows that while the simplified model is capable of predicting the reaction zone movement qualitatively, it is limited by the omission of two-dimensional effects which reveal elongated reaction layers, and reduced reaction temperatures. When compared to experimental results (Chapter 3), simulated wall temperature profiles closely match observations. In addition, a comparison of predicted product species to experimental data shows favorable agreement.

Chapter 5

Conclusions

In this study, a novel, non-catalytic reactor design for reforming of rich hydrocarbon/air mixtures is proposed, tested and investigated. The operating principle is based on counter-flow heat exchange between adjacent channels, where heat is transferred from the reaction products to preheat the incoming fuel/air mixture. This internal heat recirculation increases local reaction temperatures, which can surpass the adiabatic equilibrium temperature by a significant amount, resulting in *superadiabatic* operation of the fuel reformer. Tests of a reformer prototype show promising results, where reaction zones are stationary for a broad range of flow velocities and equivalence ratios. In contrast, most alternative non-catalytic reforming techniques are based on propagating high temperature zones. Thus, the biggest advantage of the counter-flow design over alternative non-catalytic techniques is its capability of continuous operation.

5.1 Summary

A simplified one-dimensional analysis of combustion in two adjacent channels with opposing flow directions illustrates the general operating principle of the reactor. The effective length of regions with counter-flow heat exchange determines the amount of heat recirculated between adjacent channels. This heat transfer raises the temperature level of the preheated reactant mixture before reactions occur, which increases the reaction temperatures. In general, the analytical model predicts that reaction zones move towards the reactor center as either inlet velocity or equivalence ratios of rich mixtures are increased. Furthermore, results predict that the stabilization mechanism allows for the independent selection of flow velocity and mixtures stoichiometry, which is verified in experiments.

Experiments were conducted with both methane/air and propane/air mixtures. The operating range of both fuels extends beyond the respective conventional rich flammability limit. Also, flow rates are substantially higher than those observed in conventional combustion applications, which is attributed to a substantial increase of reaction rates due to internal heat recirculation. A detailed analysis of the reaction product shows that in both cases, the fuel/air mixture is successfully converted into a hydrogen-rich syngas, where the main constituents are CO, H_2, CO_2 and N_2. A molar balance reveals substantial amounts of H_2O, which is not directly measured by the gas analyzer. Syngas also contains small amounts of unreacted or partially reacted hydrocarbons, most notably CH_4, C_2H_2, C_2H_4, and C_6H_6. In addition, experiments reveal the formation of graphite layers on the the reactor walls. The growth of graphite layers can, however, be controlled by periodically interrupting the fuel supply, which promotes the oxidation of carbonaceous deposits by air flowing through the hot reactor.

Numerical simulations with detailed reaction chemistry reveal a two-dimensional “tulip”-shaped reaction layer with a downstream curvature. The reaction process starts at points where the reaction layer attaches to a wall. Furthermore, the accumulation of products of pre-ignition reactions upstream of the attachment points is attributed to an auto-ignition process. Upon ignition, a thin reaction layer curves downstream, and joins with the reaction layer originating from the opposite wall at the center-line of the channel.

5.2 Conclusions

The starting point of this work was the development of an analytical model that is based on significiant simplifications (Chapter 2). Subsequently, analytical results were used to specify dimensions and materials of reactor prototypes that were tested successfully (Chapter 3). The last part of the study involved numerical simulations of a two-dimensional model with detailed reaction chemistry, which yielded detailed information on the combustion process (Chapter 4).

In general, experimental and numerical results agree favorably. Furthermore, both experimental and numerical results show that the simplified one-dimensional analytical model is capable of predicting shifts of the reaction zone location qualitatively.

The development of the analytical model employs results of large activation energy asymptotics, and thus is based on the assumption of thin reaction layers. In addition, the one-dimensional governing equations of the analytical model imply plug-flow within the channels, and thus do not allow for two-dimensional effects. Two-dimensional numerical simulations, however, show significant two-dimensional effects, which cause curved reaction layers. Furthermore, numerical results show that curvature affects reaction temperatures due to an increased surface area, which is particularly evident at high inlet velocities and high equivalence ratios of fuel-rich mixtures.

In numerical simulations, reductions of either inlet velocity or fuel-rich equivalence ratio result in substantially decreased reaction zone curvatures. In addition, results at those conditions show significantly reduced reaction layer thicknesses, which approach those typical for conventional combustion processes. Thus, the assumptions of the analytical model - i.e. thin reaction layers and one-dimensional flow - are valid for low inlet velocities and moderately rich fuel/air mixtures. As either inlet velocity or equivalence ratio is increased, these assumptions lose in strength. However, a comparison of analytical and numerical solutions shows that the analytical results still predict the correct trends for shifts of the combustion zone locations.

When compared to conventional catalytic reformers, non-catalytic reactor designs have the inherent advantage that they do not contain damageable catalytic surfaces. This advantage becomes particularly important for fuel reforming technologies that are based on the partial oxidation of a fuel, where reactions are strongly exothermic and excessive temperatures can damage catalytically active surfaces. A direct comparison to results obtained from studies involving catalytic reforming is, however, difficult, as catalytic approaches usually involve multiple stages in the reforming process. In addition to a stage where catalysts promote the partial oxidation of a fuel, catalytic technologies often utilize dedicated water-gas shift reactors that increase the hydrogen concentration by reacting steam and carbon monoxide to hydrogen and carbon dioxide.

The goal of this study was to demonstrate the feasibility of a non-catalytic fuel reformer design that stabilizes reaction zones by counter-flow heat exchange. Due to its suitability for continuous operation, the reactor design developed in this study is superior to earlier reactor designs used in non-catalytic fuel reforming that are largely based on propagating reaction zones in filtration reactors. Efficiencies for the conversion of a primary fuel to syngas are, however, somewhat lower than those found in filtration reactors. The difference between the reactor designs is attributed to longer residence times in high temperature zones in the case of the filtration reactor, resulting in a more complete break-down of intermediate hydrocarbon species. While residence times are mainly a function of channel length and flow velocity, analytical results predict that characteristics of the high temperature zone can be adjusted by tuning both reactor geometry and the conductivity of the wall material.

5.3 Recommendations

Future work based on this study should consider the findings from both experimental and numerical work. Experiments showed a propensity for the formation of graphite layers on the reactor walls, which requires further investigation. In particular, the operating conditions under which deposits are formed need to be identified. In this, concentrations of soot precursors such as C_2H_2, C_6H_6, among others, may reveal cues to the formation of graphite and soot. Furthermore, numerical results from this study indicate that the curvature of the reaction zone affects reaction temperatures, and, by consequence, the composition of the product stream. While the capabilities of the current numerical model are limited to 50 chemical species, a better understanding of the formation of soot precursors requires larger reaction mechanisms that have become available recently (Richter and Howard, 2002; Hoyermann et al., 2004). In addition, the impact of differences in heat losses from internal and external reactor channels deserves attention, as the current numerical model assumes an infinite array of reactor channels.

In further optimizations of the reactor geometry, both the simplified analytical model as well as the detailed numerical model yield valuable information. While the strength of the analytical model lies in its capability to predict the effect of parameter changes qualitatively, the 2-D model is essential for the assessment of shape and structure of reaction layers, which depend on flow velocity, mixture properties and, as shown in other numerical studies (Michaelis and Rogg, 2004; Kim and Maruta, 2006), channel height.

A significant hurdle for a broader commercialization of the reformer design is a suitable manufacturing process, as the construction of reactor prototypes used for this study entailed a cumbersome assembly. Work on manufacturing was started by Newcomb (2009), who used selective laser sintering (SLS), a rapid prototyping technique, for the construction of a monolithic fuel reformer.

Appendix A

Large Activation Energy Asymptotics

The analytical model described in Chapter 2 is based on results obtained from large activation energy asymptotics. While many solution processes are documented in the combustion literature (see Section 2.1), the specific approach used for the analytical model is based on a solution that was originally put forward by Matkowsky and Sivashinsky (1979). In their work, they showed that the inner solution of the flame sheet can be approximated to first order by a delta function, where the strength is obtained from the solution of the simpler case of a rectilinearly propagating flame front. Since, this result has been used for a series of studies on non-adiabatic combustion processes, e.g. Zamashchikov and Minaev (2001), Fursenko, et al. (2001), Ju and Choi (2003), Maruta, et al. (2005), and others.

The underlying idea for the analytical model of a combustion process subject to cross-wall heat exchange is that the reaction terms of the non-adiabatic process are treated as a perturbation of the classical solution of the adiabatic flame speed (Bush and Fendell, 1970). This approach is equivalent to the assumption that the characteristic length scale of heat transfer between gas phase and solid wall is significantly larger than respective length scales for gas diffusion and reaction zone.

In the following, the derivation of the analytical model in Chapter 2, published in Schoegl and Ellzey (2007a), is enhanced by highlighting critical steps taken in the approximation of distributed reaction zones by point sources. Also, the solution process necessary for the calculation of results of the analytical model is further illuminated. It is noted that none of the equations listed below contain new results, but instead refer to significant equations in Chapter 2.

In Section 2.2.2, the non-dimensional governing equations for gas phase temperatures T_i and concentrations of limiting species y_i are given by Eqs. 2.6 and 2.7 as

$$\begin{aligned}\frac{d^2T_i}{dx^2} &= \frac{u_i}{\epsilon}\frac{dT_i}{dx} + \frac{\mu}{\epsilon^2}(T_i - T_w) - \frac{\gamma}{\epsilon^2}w_i \\ \frac{1}{\text{Le}}\frac{d^2y_i}{dx^2} &= \frac{u_i}{\epsilon}\frac{dy_i}{dx} + \frac{1}{\epsilon^2}w_i\end{aligned}$$

where subscripts $_i$ denote the channel number in a two-channel configuration, u_i are flow velocities, x is the axial position along the channel,ϵ and μ are parameters for geometry and interfacial heat transfer, respectively, T_w is the wall temperature, γ pertains to the temperature scaling, and Le is the Lewis number. Furthermore, the non-dimensional reaction terms

$$w_i \approx y_i \Lambda \exp\left(\frac{\beta(T_i - T_{\text{ad}})}{T_i / T_{\text{ad}}}\right)$$

model the combustion processes occurring in each of the two channels (Eq. 2.5). Here, Λ is an eigenvalue, β is a non-dimensional activation energy, and T_{ad} is the adiabatic equilibrium temperature for the mixture. It is noted that the reaction rate expression given above is not localized, i.e. reactions take place in a combustion zone of finite thickness. Assuming a large activation energy β, however, w_i vanishes for $T_i \ll T_{\text{ad}}$ and it can be assumed that the chemistry is frozen upstream of the reaction zone. Once gas temperatures approach the vicinity of T_{ad}, reaction rates increase significantly, resulting in a rapid decrease of reactant concentrations. As a consequence of a large activation energy β, reaction processes take place within thin reaction layers.

The first critical step for the development of the analytical model is taken in Section 2.2.3, where the result of an asymptotic expansion (Matkowsky and Sivashinsky, 1979) is employed to replace the distributed combustion zones by point sources (Eq. 2.8) as

$$w_i \approx \epsilon\delta\left(x - x_{c,i}\right)\exp\left(\frac{\beta\left(T - T_{\mathrm{ad}}\right)}{2T/T_{\mathrm{ad}}}\right)$$

Here, $\delta\left(x - x_{c,i}\right)$ are Dirac delta functions at the combustion zone locations $x_{c,i}$. One important implication of this replacement is that the reaction terms are no longer explicitly dependent on the species concentrations y_i.

The assumption of point sources at - thus far unknown - reaction zone locations allows for the subdivision of the solution domain into sections defined by the locations of the two combustion zones (see Fig. 2.3). Thus, the original non-linear governing equations (Eqs. 2.6 and 2.7) become a set of three piecewise-linear differential equation systems linked by internal boundary conditions at the combustion zone locations. In particular, the introduction of point sources at the combustion zone locations are represented by discontinuities in the first derivative of solutions for temperature T_i and limiting species y_i (Section 2.2.4). In mathematical terms, these discontinuities are expressed by jump conditions given in Eqs. 2.14a and 2.14b,

$$\begin{aligned}
\left[\frac{dT_i}{dx}\right]_-^+ &= \frac{\gamma}{\epsilon}\exp\frac{\beta\left(T_i - T_{\mathrm{ad}}\right)}{2T_i/T_{\mathrm{ad}}} \\
\left[\frac{dy_i}{dx}\right]_-^+ &= -\frac{\mathrm{Le}}{\epsilon}\exp\frac{\beta\left(T_i - T_{\mathrm{ad}}\right)}{2T_i/T_{\mathrm{ad}}}
\end{aligned}$$

where $[f]_-^+$ denotes the difference of function values to the left and right of an internal boundary.

The second critical step is based on the observation that by using the simplifications outlined above, the coupling between species concentration and temperature only appears in the internal boundary condition of the equation system resulting from the governing equation for species concentration y_i (Eq. 2.7). Furthermore, the solution of Eq. 2.7 can be obtained in symbolic form without using the jump condition at the reaction front, where flow velocities u_i and combustion locations $x_{c,i}$ remain unknown. The solution for y_i, given in Eq. 2.16, can be combined with the internal boundary condition to obtain a relation between the magnitude of flow velocities u_i and peak temperatures at the combustion zone location $T_{c,i}$,

$$|u_i| \quad = \quad \exp \frac{\beta (T_{c,i} - T_{\mathrm{ad}})}{2T_{c,i}/T_{\mathrm{ad}}} \tag{A.1}$$

given in Eq. 2.17.

Once the solution of the species concentration y_i is obtained in symbolic form, the remaining analysis involves the solution of a heat transfer problem. As discussed in Section 2.3, the governing equations are given by a set of linear differential equations, where the reaction terms are modeled by non-linear internal boundary conditions at unknown combustion zone locations.

In order to solve the heat transfer problem, Eq. A.1 needs to be satisfied, which requires consistent values for flow velocities u_i, combustion zone locations $x_{c,i}$ and peak temperatures $T_{c,i}$. In most cases, the solution process requires either the determination of the combustion zone location $x_{i,c}$ for specified flow velocities u_i, or vice versa. In either case, Eq. A.1 is used to simplify the jump conditions at the combustion zone locations, which allows for a straightforward solution of the heat transfer problem (Section 2.3). As this step eliminates the non-linear reaction term, the solution does not involve Eq. A.1 directly, and either $x_{c,i}$ or u_i need to be adjusted in an iterative solution process until Eq. A.1 is satisfied.

Appendix B

Single-Step Mechanism

The analytical model for combustion in finite parallel channels, developed in Chapter 2, is based on a simplified reaction mechanism with mixture-dependent parameters, listed in Table 2.1. The simplified reaction mechanism is a single-step Arrhenius-type reaction model, and is calibrated using numerical results from the combustion code PREMIX (Kee et al., 1985) with the reaction chemistry given by GRI-MECH 3.0 (Smith et al., 1999).

In the following, the single-step kinetics model is derived from a semi-empirical correlation relating the mass flux through the combustion zone to preheating level and energy content of the unburned mixture. The derivation is structured in three sections: first, parameters of a semi-empirical correlation are fitted to numerical results; second, a calibration curve yielding constant mass flux is defined; and third, the semi-empirical correlation is linearized to obtain the single-step kinetics model used in Chapter 2, together with the parameters listed in Table 2.1. Due to this approach, the single-step kinetics model acts as an approximation of a detailed reaction mechanism.

B.1 Semi-Empirical Correlation

Following the ideas of Zeldovich, Frank-Kamenetskii, and Semenov, the adiabatic flame speed u'_{ad} is a function of the unburned temperature T'_u, the adiabatic flame temperature T'_{ad}, the adiabatic temperature increase $\Delta T' = T'_{\mathrm{ad}} - T'_u$ and the reaction rate. The theory is outlined in detail in Glassman (1996), and the final result can be written in generalized form as

$$\rho' u'_{\mathrm{ad}} \approx Z' \, {T'_u}^{\varkappa_1} \, {T'_{\mathrm{ad}}}^{\varkappa_2} \, (T'_{\mathrm{ad}} - T'_u)^{\varkappa_3} \exp\left(-\frac{\tilde{E}'_a}{2R'T'_{\mathrm{ad}}}\right), \tag{B.1}$$

The left-hand-side of the expression gives the mass flux $\rho' u'_{\mathrm{ad}}$, which specifies the rate at which reactants are consumed. On the right-hand-side, property values as well as the reaction frequency are lumped together in the constant Z', and the reaction rate is approximated by Arrhenius-type kinetics as $\exp\left(-\tilde{E}'_a/R'T'_{\mathrm{ad}}\right)$, with activation energy $\tilde{E}'_a$ and universal gas constant R'. Furthermore, Eq. B.1 contains several terms modeling temperature dependencies, where the exponents $\varkappa_i$ depend on the reaction order.

The constant Z' can be eliminiated by taking the ratio of two mass fluxes at different inlet temperatures and/or equivalence ratios, yielding the correlation

$$\frac{\left(\rho' u'_{\mathrm{ad}}\right)_1}{\left(\rho' u'_{\mathrm{ad}}\right)_2} \approx \left(\frac{T'_{u,1}}{T'_{u,2}}\right)^{\varkappa_1} \left(\frac{T'_{\mathrm{ad},1}}{T'_{\mathrm{ad},2}}\right)^{\varkappa_2} \left(\frac{\Delta T'_1}{\Delta T'_2}\right)^{\varkappa_3} \exp\left(-\frac{\tilde{E}'_a}{2R'}\left(\frac{1}{T'_{\mathrm{ad},1}} - \frac{1}{T'_{\mathrm{ad},2}}\right)\right) \tag{B.2}$$

Eq. B.2 still contains the unknowns $\varkappa_1$, $\varkappa_2$, $\varkappa_3$ and $\tilde{E}'_a$. For a known reaction order, it is possible to determine values for $\varkappa_i$ analytically (Glassman, 1996). In the more general approach taken below, $\varkappa_i$ as well as $\tilde{E}'_a$ are calibrated based on numerical results for combustion of rich methane/air mixtures.

Table B.1: Parameter fit of Eq. B.2 for methane/air mixtures.

ϕ_{ref}	T_{ref}	$\varkappa_1$	$\varkappa_2$	$\varkappa_3$	E'_a
1.6	298	0.0086	3.5793	-1.2530	13,463

Numerical values for the parameters of Eq. B.2 were obtained by parameter fits of numerical results from the premixed combustion code PREMIX (Kee et al., 1985) with the reaction mechanism GRI-MECH 3.0 (Smith et al., 1999). Values denoted by subscipt “2” in Eq. B.2 were defined at a the common reference condition $\phi_{\text{ref}} = 1.6$ and $T'_{u,\text{ref}} = 298\,[\text{K}]$, which is close to the conventional rich flammability limit of methane/air mixtures at $\phi = 1.7$. Results of the parameter fit are listed in Table B.1.

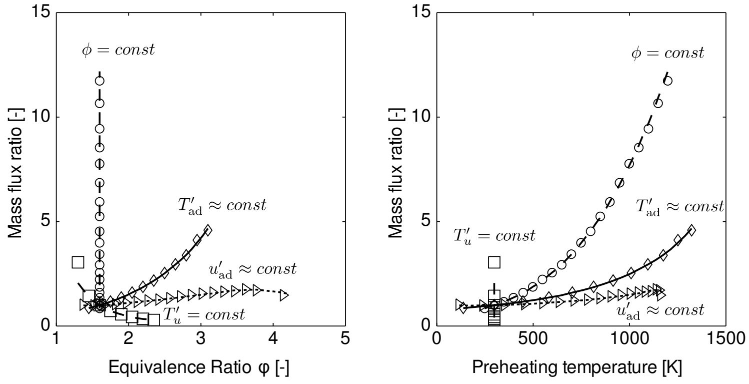

Figure B.1: Comparison of mass-flux ratios computed by PREMIX (markers) and predicted by correlation B.2 (lines) for different variations of equivalence ratios and inlet temperatures.

Figure B.1 compares mass-flux ratios predicted from the correlation to numerical results for variations of equivalence ratios and/or inlet temperatures. Predictions from the calibrated correlation show excellent agreement to numerical PREMIX results over a wide range of equivalence ratios and inlet temperatures.

B.2 Calibration

Both the adiabatic flame speed and the adiabatic flame temperature are functions of the temperature of the unburned mixture T'_u and the equivalence ratio ϕ. Thus it is possible to define a preheating level that guarantees a constant mass flux through the

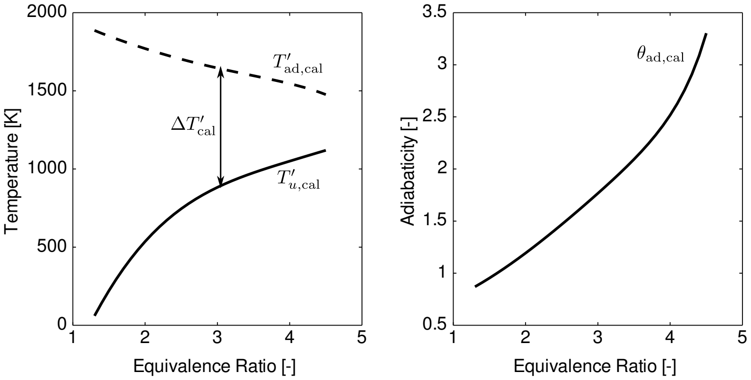

Figure B.2: Calibration for constant mass flux: results for (a) unburned and peak temperatures, $T'_{u,\mathrm{cal}}$ and $T'_{\mathrm{ad,cal}}$; and (b) adiabaticity $\theta_{\mathrm{ad,cal}}$.

combustion zone, i.e. the preheating level is adjusted such that the condition

$$\frac{\left(\rho' u'_{\mathrm{ad}}\right)_{\mathrm{cal}}}{\left(\rho' u'_{\mathrm{ad}}\right)_{\mathrm{ref}}} = 1 \tag{B.3}$$

is satisfied along a calibration curve for $T'_{u,\mathrm{cal}}$ in dependence of the equivalence ratio. The reference mass flux $\left(\rho' u'_{\mathrm{ad}}\right)_{\mathrm{ref}}$ is calculated at $\phi_{\mathrm{ref}} = 1.6$ and $T'_{u,\mathrm{ref}} = 298\,[\mathrm{K}]$, yielding a mass-flux of 9.29e-03 g/cm^2/s^2 ($u'_{\mathrm{ad,ref}} = 8.38$ cm/s). By enforcing constant mass-flux along the calibration curve, Eq. B.3 makes it possible to tie the correlation given by Eq. B.2 to a unique mass flux that is independent of the equivalence ratio ϕ.

Figure B.2a shows results for unburned and peak temperatures, $T'_{u,\mathrm{cal}}$ and $T'_{\mathrm{ad,cal}}$ at calibrated conditions.. In order to maintain a constant mass flux, the temperature of the unburned mixture has to be increased as the equivalence ratio increases, while the resulting peak temperatures decrease.

Defining an adiabaticity θ as

$$\theta = \frac{c'_p}{y'_0 Q'}\left(T' - T'_\infty\right) = \frac{T' - T'_\infty}{\left(T'_{\mathrm{ad}} - T'_u\right)_{\mathrm{cal}}} = \frac{T' - T'_\infty}{\Delta T'_{\mathrm{cal}}}. \tag{B.4}$$

where Q' is the adiabatic heat addition, y'_0 is the initial concentration of the species limiting the reaction, c'_p is the specific heat of the gas and T'_∞ is the temperature of the environment, $\theta > 1$ becomes the condition for superadiabatic combustion. Figure B.2b shows the adiabaticity as a function of the equivalence ratio. As the energy content of the air/fuel mixture decreases with increasing equivalence ratio, the adiabaticity increases.

B.3 Linearization

The semi-empirical correlation developed in Section B.1 is closely related to chemical kinetics approximations commonly used in combustion theory, which follow from a linearization of Eq. B.2. In addition, the actual peak combustion temperature T'_{ad} at any given equivalence ratio ϕ and unburned temperature T'_u can be related to an unique mass-flux by choosing linearization points along the calibration curve for $T'_{\mathrm{ad,cal}}$.

The parameter fit of Eq. B.2 to numerical results from PREMIX yields $\varkappa_1 \ll 1$ (Table B.1), i.e. the mass flux ratio is almost independent from the preheated temperature and thus can be neglected. Furthermore, the temperature increase $\Delta T'$ at any given ϕ is generally a weak function of the preheated temperature T'_u, and the approximation $\Delta T'_{\mathrm{ad}}/\Delta T'_{\mathrm{ad,cal}} \approx 1$ eliminates the term with the exponent $\varkappa_3$. Taking the logarithm, the linearized relation can be expressed as

$$\log \frac{\left(\rho' u'_{\mathrm{ad}}\right)}{\left(\rho' u'_{\mathrm{ad}}\right)_{\mathrm{cal}}} \approx -\frac{\tilde{E}'_a}{2R'T'_{\mathrm{ad,cal}}}\left(\frac{T'_{\mathrm{ad,cal}}}{T'_{\mathrm{ad}}} - 1\right) - \varkappa_2 \log \frac{T'_{\mathrm{ad,cal}}}{T'_{\mathrm{ad}}}$$

$$\approx \left(\frac{\tilde{E}'_a}{2R'T'_{\mathrm{ad,cal}}} + \varkappa_2\right)\left(1 - \frac{T'_{\mathrm{ad,cal}}}{T'_{\mathrm{ad}}}\right)$$

where the Taylor series approximation $\ln(1+x) \approx x$ has been used. Defining the modified activation energy $E'_a = \tilde{E}'_a + 2\varkappa_2 R' T'_{\mathrm{ad,cal}}$ and introducing the Zeldovich number

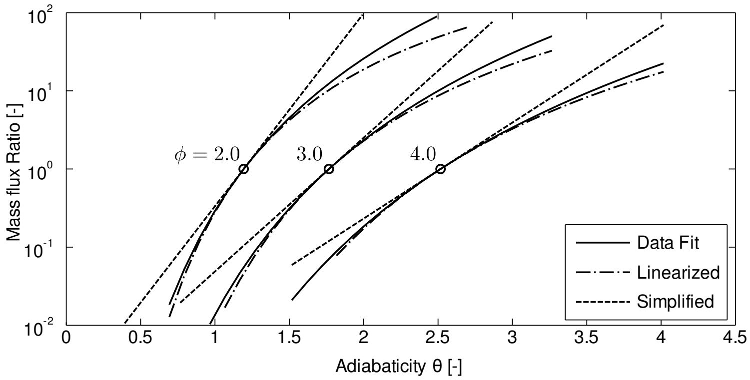

Figure B.3: Comparison of correlation (Eq. B.2) with different approximation levels (Eq. B.5 - linearized; and Eq. B.6 - simplified) to illustrate the dependence of mass flux ratios on adiabaticies θ. Circles mark linearization points.

$\mathrm{Ze} = E'_a \Delta T'_{\mathrm{ad,cal}} / R' \, {T'_{\mathrm{ad,cal}}}^2$ follows

$$\log \frac{\left(\rho' u'_{\mathrm{ad}}\right)}{\left(\rho' u'_{\mathrm{ad}}\right)_{\mathrm{cal}}} \approx \frac{\mathrm{Ze}}{2} \frac{\left(T'_{\mathrm{ad}} - T'_{\mathrm{ad,cal}}\right) / \Delta T'_{\mathrm{cal}}}{T'_{\mathrm{ad}} / T'_{\mathrm{ad,cal}}} \tag{B.5}$$

which is the dimensional form of the non-dimensional expression used in Chapter 2.

For small deviations from the calibration curve, i.e. $T'_{\mathrm{ad}}/T'_{\mathrm{ad,cal}} \approx 1$, this can be further simplified to

$$\log \frac{\left(\rho' u'_{\mathrm{ad}}\right)}{\left(\rho' u'_{\mathrm{ad}}\right)_{\mathrm{cal}}} \approx \frac{\mathrm{Ze}}{2} \frac{T' - T'_{\mathrm{ad,cal}}}{\Delta T'_{\mathrm{cal}}} \tag{B.6}$$

which is another approximation commonly used in combustion theory (Fursenko et al., 2001; Ju and Choi, 2003).

Figure B.3 compares results for different approximation levels of the empirical correlation for the mass-flux ratio, Eqs. B.2, B.5 and B.6. Results for changes in mass flux ratios are illustrated for a variation of adiabaticities θ, based on linearizations at equivalence ratios $\phi = 2.0, 3.0, 4.0$. The different curves compare the predictions of the correlation given by Eq. B.2 to expressions linearized around the calibration curve (Figure B.2a). The linearization given by Eq. B.5 is used in Chapter 2 and captures the correct behavior over a wide range of temperatures. The more simplified form

Eq. B.6 shows good agreement in the immediate neighborhood of the linearization point, but overpredicts the mass flow for equivalence ratios far below and far above the linearization point. Noting the logarithmic scaling used for the mass flux ratios, all cases illustrate that small temperature changes cause large changes of the mass flux (Ronney, 2003).

Appendix C

Processing of Experimental Data

A better understanding of experimental results, presented in Chapter 3, requires some data processing of direct measurement to illustrate the efficiency of the reforming process. While appropriate definitions are given whenever new metrics are introduced in Chapter 3, the purpose of this appendix is to list a more complete deduction of the equations. Below, conversion efficiencies are developed from molar balances, and appropriate uncertainty calculations are specified.

C.1 Conversion efficiencies

C.1.1 Molar Balances

Reactant Stream For a generic hydrocarbon fuel C_nH_{2m}, the reactant side of the global reaction equation is written as

$$\phi \; C_nH_{2m} + r\,(O_2 + 3.76N_2) \rightarrow \mathit{products} \tag{C.1}$$

where ϕ is the equivalence ratio, C_nH_{2m} is the fuel species, and $r = n + m/2$ is the number of O_2 moles needed for complete oxidation of the fuel, e.g. $r = 2$ for CH_4 fuel or $r = 5$ for C_3H_8 fuel. At ϕ=1, reaction C.1 uses r moles of oxygen and $4.76r$

moles of nitrogen for every mole of fuel.

Assuming a molar flow rate of fuel $\dot{N}_{\mathrm{fu}}$, the molar rates of atomic carbon and diatomic hydrogen contained in reactant stream can be expressed by the ratios

$$\frac{\dot{N}_{\mathrm{C,reac}}}{\dot{N}_{\mathrm{fu}}} = n \tag{C.2a}$$

$$\frac{\dot{N}_{\mathrm{H_2,reac}}}{\dot{N}_{\mathrm{fu}}} = m \tag{C.2b}$$

Likewise, the molar flow rates of oxygen and nitrogen necessary for reactions at a specified equivalence ratio ϕ can be written as

$$\frac{\dot{N}_{\mathrm{O_2,reac}}}{\dot{N}_{\mathrm{fu}}} = \frac{r}{\phi} \tag{C.3a}$$

$$\frac{\dot{N}_{\mathrm{N_2,reac}}}{\dot{N}_{\mathrm{fu}}} = \frac{3.76r}{\phi} \tag{C.3b}$$

while the total flow rates reactant moles normalized by the molar flow rate of fuel is given by

$$\frac{\dot{N}_{\mathrm{reac}}}{\dot{N}_{\mathrm{fu}}} = 1 + r\frac{4.76}{\phi} \tag{C.4}$$

Product stream The molar flow rate of any species i in the product stream produced is given by $\dot{N}_{i,\mathrm{prod}} = y_{i,\mathrm{prod}}\dot{N}_{out}$, where y_i is the molar concentration of species i. Thus the molar flow rate of products can be related to the molar flow rate of fuel as

$$\frac{\dot{N}_{\mathrm{prod}}}{\dot{N}_{\mathrm{fu}}} = \frac{1}{y_i}\frac{\dot{N}_{i,\mathrm{prod}}}{\dot{N}_{\mathrm{fu}}} \tag{C.5}$$

Nitrogen balance At rich conditions typical for fuel reforming, equilibrium calculations do not predict any significant amounts of nitrogen oxides (NO_x) or other nitrogen compounds in the products. Thus, the molar flow rate of nitrogen is conserved throughout the chemical reactions, i.e. $\dot{N}_{\mathrm{N_2,prod}} = \dot{N}_{\mathrm{N_2,reac}}$. Combining Eqs. C.3b and C.5, the molar rate of product species is written in terms of the equivalence ratio ϕ and the molar concentration of y_{N_2} as

$$\frac{\dot{N}_{\text{prod}}}{\dot{N}_{\text{fu}}} = \frac{r}{y_{N_2}}\frac{3.76}{\phi}$$

As the ratio of molar flux of product to the molar flux of fuel is essential for subsequent calculations, it is defined as a new variable, $\varkappa$, as.

$$\varkappa \equiv \frac{r}{y_{N_2}}\frac{3.76}{\phi} \tag{C.6}$$

Oxygen balance The ratio of oxygen bound in a specific chemical species in the product stream to oxygen available in the reactant stream can be used to track the distribution of oxygen in the product species. Using Eqs. C.3a and C.6, this ratio can be written as

$$\frac{\dot{N}_{i,\text{prod}}}{\dot{N}_{O_2,\text{reac}}} = \frac{3.76}{y_{N_2}}\left(o_i y_{i,\text{prod}}\right) = \frac{\varkappa\phi}{r}\left(o_i y_{i,\text{prod}}\right) \tag{C.7}$$

where o_i is the number of O_2 moles in each mole of species i.

The oxygen balance can be used to compute the amount of water vapor produced by the reactions, which can otherwise not be quantified in measurements obtained from a gas chromatography system. Assuming that the only exhaust gas species containing significant amounts of O are H_2O, CO, CO_2, and O_2, the amount of water vapor produced by the reactions is given by

$$\frac{\frac{1}{2}\dot{N}_{H_2O}}{\dot{N}_{O_2,\text{reac}}} = 1 - \frac{3.76}{y_{N_2}}\left(y_{O_2} + \frac{1}{2}y_{CO} + y_{CO_2}\right) = 1 - \frac{\varkappa\phi}{r}\left(y_{O_2} + \frac{1}{2}y_{CO} + y_{CO_2}\right) \tag{C.8}$$

Hydrogen balance Similar to the oxygen balance, the ratio of hydrogen bound in a specific chemical species in the product stream to hydrogen available in the reactant stream tracks the distribution of hydrogen in the product species. Using Eqs. C.2b and C.6, this ratio becomes

$$\frac{\dot{N}_{i,}}{\dot{N}_{H_2,\text{reac}}} = \frac{\varkappa}{m_{\text{fu}}}\left(m_i y_{i,\text{prod}}\right) \tag{C.9}$$

where the individual m_i are the number of H_2 moles bound per mole of product species i .

An alternative, albeit less accurate, calculation of the amount of steam in the products is based on the hydrogen balance. Assuming that all major hydrogen-carrying components are measured, the balance can be written as

$$\frac{\dot{N}_{\mathrm{H_2O}}}{\dot{N}_{\mathrm{H_2,reac}}} = 1 - \frac{\varkappa}{m_{\mathrm{fu}}} \sum_i m_i y_{i,\mathrm{prod}} \tag{C.10}$$

This method is, however, affected by a large number of possible product species. A more exact calculation converts the fraction of water obtained from the oxygen balance (Eq. C.8), i.e.

$$\frac{\dot{N}_{\mathrm{H_2O}}}{\dot{N}_{\mathrm{H_2,reac}}} = \frac{2r}{m\phi} \frac{\frac{1}{2}\dot{N}_{\mathrm{H_2O}}}{\dot{N}_{\mathrm{O_2,reac}}} \tag{C.11}$$

which follows directly from a combination of Eqs. C.2b and C.3a.

Carbon balance Finally, the ratio of carbon bound in a specific chemical species in the product stream to carbon available in the reactant stream tracks the distribution of carbon. Using Eqs. C.2b and C.6, this ratio becomes

$$\frac{\dot{N}_{i,\mathrm{prod}}}{\dot{N}_{\mathrm{C,reac}}} = \frac{\varkappa}{n_{\mathrm{fu}}} \left(n_i y_{i,\mathrm{prod}} \right) \tag{C.12}$$

where n_i is the number or carbon moles per mole of product species i.

C.1.2 Hydrogen conversion

The hydrogen conversion efficiency is defined as the ratio of rate of H_2 moles generated to the maximum rate available in the reactant stream. Thus, the molar efficiency for hydrogen production is given by

$$\eta_{\mathrm{H_2}} \equiv \frac{\dot{N}_{\mathrm{H_2,}}}{\dot{N}_{\mathrm{H_2},max}}$$

Using Eqs. C.2b, C.5 and C.6, the hydrogen conversion can be written as

$$\eta_{\mathrm{H}_2} = \frac{y_{\mathrm{H}_2}}{m}\frac{N_{\mathrm{prod}}}{N_{\mathrm{fu}}} = y_{\mathrm{H}_2}\frac{\varkappa}{m} \tag{C.13}$$

C.1.3 Total Energy conversion efficiency

The *total energy conversion efficiency* compares the chemical energy content of the products to that of the reactants and thus is defined as

$$\eta_{\mathrm{Energy}} \equiv \frac{\sum_{\mathrm{prod}} \dot{N}_i \; LHV_i}{\dot{N}_{\mathrm{fu}} LHV_{\mathrm{fu}}} \tag{C.14}$$

where $\dot{N}_i$ represent molar flow rates of product species containing energy, and *LHV* refers to the lower heating value of the species in kJ/kmol at standard atmospheric conditions.

Using Eqs. C.5 and C.6, the total energy conversion efficiency can be expressed in terms of molar concentrations as

$$\eta_{\mathrm{Energy}} = \frac{\sum_{\mathrm{prod}} \dot{N}_i/\dot{N}_{\mathrm{fu}} \; LHV_i}{LHV_{\mathrm{fu}}} = \varkappa \frac{\sum_{\mathrm{prod}} y_i \; LHV_i}{LHV_{\mathrm{fu}}} \tag{C.15}$$

C.1.4 Hydrogen Energy Conversion Efficiency

The hydrogen energy conversion efficiency is defined similar to Eq. , but only considers hydrogen among the energy carrying product species, i.e.

$$\eta_{\mathrm{Energy},\mathrm{H}_2} = \frac{\dot{N}_{\mathrm{H}_2} \; LHV_{\mathrm{H}_2}}{\dot{N}_{\mathrm{fu,reac}} LHV_{\mathrm{fu}}} = \varkappa y_{\mathrm{H}_2} \frac{LHV_{\mathrm{H}_2}}{LHV_{\mathrm{fu}}} \tag{C.16}$$

C.2 Uncertainties

C.2.1 Uncertainty of Operating Conditions

The operating condition is given by the inlet velocity u as well as the equivalence ratio ϕ, which result from mixing of two separately controlled streams of air and fuel.

The inlet velocity is easily calculated from the cross-section area of the reactor, A, and the volumetric flow rates of fuel and oxidizer, $\dot{V}_{\mathrm{fu}}$ and $\dot{V}_{\mathrm{ox}}$, i.e.

$$u\left(\dot{V}_{\mathrm{fu}}, \dot{V}_{\mathrm{ox}}, A\right) = \frac{1}{A}\left(\dot{V}_{\mathrm{fu}} + \dot{V}_{\mathrm{ox}}\right) \tag{C.17}$$

Thus, the uncertainty is given by the root-sum-square of partial derivatives as

$$\begin{aligned} \delta u &= \left[\left(\frac{\partial u}{\partial \dot{V}_{\mathrm{fu}}}\delta \dot{V}_{\mathrm{fu}}\right)^2 + \left(\frac{\partial u}{\partial \dot{V}_{\mathrm{ox}}}\delta \dot{V}_{\mathrm{ox}}\right)^2 + \left(\frac{\partial u}{\partial A}\delta A\right)^2\right]^{1/2} \\ &= \frac{1}{A}\left[\delta \dot{V}_{\mathrm{fu}}^2 + \delta \dot{V}_{\mathrm{ox}}^2\right]^{1/2} + \frac{1}{A}\left(\dot{V}_{\mathrm{fu}} + \dot{V}_{\mathrm{ox}}\right)\left(\frac{\delta A}{A}\right) \end{aligned} \tag{C.18}$$

The uncertainties for $\delta \dot{V}_{\mathrm{fu}}$ and $\delta \dot{V}_{\mathrm{ox}}$ are assumed as 2% and 1% of the maximum ranges of air and fuel flow controllers, respectively, whereas the tolerance of the channel cross-section area is estimated as 5%.

The equivalence ratio is defined as

$$\phi = \frac{\left(\dot{N}_{\mathrm{fu}}/\dot{N}_{\mathrm{ox}}\right)}{\left(\dot{N}_{\mathrm{fu}}/\dot{N}_{\mathrm{ox}}\right)_{stoich}} \tag{C.19}$$

where the oxidizer stream is given by $\dot{N}_{\mathrm{ox}} = \dot{N}_{\mathrm{O_2}} + \dot{N}_{\mathrm{N_2}}$. Assuming an ideal gas with constant molar density at a given pressure and temperature, the volumetric flow is directly proportional to the molar flow rates, and Eqs. C.3a and C.3b yield

$$\phi = 4.76 m \frac{\dot{V}_{\mathrm{fu}}}{\dot{V}_{\mathrm{ox}}} \tag{C.20}$$

Table C.1: Uncertainties for gas chromatography system and calibration gases.

	Uncertainty
Gas chromatography system	±1% of calibrated range
O_2, H_2, N_2, CO, CO_2, methane, ethylene, acetylene	±1% of specified value
ethane, propane, n-butane, n-pentane, n-hexane, n-heptane	±5% of specified value
iso-butane, iso-pentane, 1-butene, 1-pentene, 1-hexene, benzene	±5% of specified value

Thus, the uncertainty in the equivalence ratio becomes

$$\delta\phi = \phi\left[\left(\frac{\delta\dot{V}_{\mathrm{fu}}}{\dot{V}_{\mathrm{fu}}}\right)^2 + \left(\frac{\delta\dot{V}_{\mathrm{ox}}}{\dot{V}_{\mathrm{ox}}}\right)^2\right]^{1/2} \tag{C.21}$$

C.2.2 Uncertainty of Exhaust Gas Measurements

A large number of measurements of exhaust gas concentrations at one condition can be assumed as a stochastic process. Thus, the measured value can be bracketed by the sum of the average value plus/minus the uncertainty as $y_{i,meas} = \bar{y}_i \pm \delta y_i$. A common metric used to quantify the uncertainty is the standard deviation, which, however, requires a large number of measurements to get an accurate mean value. Whenever only a small number of experiments is available, the random uncertainty of the mean value can be estimated using the Student-t distribution as

$$\delta y_{i,meas} \approx t_{a,n-1}\frac{\sigma_n}{\sqrt{n}} \tag{C.22}$$

where σ_n is the standard deviation calculated from n samples, and $t_{a,n-1}$ is the tabulated value of the Student-t distribution (Wheeler and Ganji, 2004). The value of $t_{a,n-1}$ is a function of $n-1$ and the parameter a, which is the probability that the true value lies outside a confidence interval .

The uncertainty given in Eq. C.22 cannot, however, assess uncertainties that originate from non-stochastic processes, e.g. systematic error such as linearity errors, or calibration errors. In order to include non-stochastic influences, specifications for the uncertainty of the gas chromatography system, $\delta y_{i,GC}$, and calibration gases, $\delta y_{i,calib}$, were considered (Table C.1). Using root-mean-square values, the overall uncertainty of the gas concentration of species i is given by

$$\delta y_i = \left[(\delta y_{i,meas})^2 + (\delta y_{i,GC})^2 + (\delta y_{i,calib})^2\right]^{1/2} \tag{C.23}$$

C.2.3 Uncertainty of Molar Balances and Efficiency Calculations

Nitrogen Balance The uncertainty of the moles of reactants per moles of fuel, defined through the nitrogen balance in Eq. C.6, is given by

$$\delta\varkappa = \varkappa\left[\left(\frac{\delta\phi}{\phi}\right)^2 + \left(\frac{\delta x_{N_2}}{x_{N_2}}\right)^2\right]^{1/2} \tag{C.24}$$

Oxygen Balance The uncertainty of the amount of oxygen bound in product species i compared to oxygen available in the reactants is

$$\delta\left(\frac{\dot{N}_{i,\mathrm{prod}}}{\dot{N}_{\mathrm{O_2,reac}}}\right) = \frac{\dot{N}_{i,\mathrm{prod}}}{\dot{N}_{\mathrm{O_2,reac}}}\left[\left(\frac{\delta y_{i,\mathrm{prod}}}{y_{i,\mathrm{prod}}}\right)^2 + \left(\frac{\delta y_{\mathrm{N_2}}}{y_{\mathrm{N_2}}}\right)^2\right]^{1/2} \tag{C.25}$$

Likewise, the uncertainty of the water vapor computed from oxygen balance, defined in Eq. C.8, is given by

$$\delta\left(\frac{\frac{1}{2}\dot{N}_{\mathrm{H_2O}}}{\dot{N}_{\mathrm{O_2,reac}}}\right) = \left(1 - \frac{\frac{1}{2}\dot{N}_{\mathrm{H_2O}}}{\dot{N}_{\mathrm{O_2,reac}}}\right)\left[\frac{\delta y_{\mathrm{O_2}}^2 + \frac{1}{2}\delta y_{\mathrm{CO}}^2 + \delta y_{\mathrm{CO_2}}^2}{\left(y_{\mathrm{O_2}} + \frac{1}{2}y_{\mathrm{CO}} + y_{\mathrm{CO_2}}\right)^2} + \left(\frac{\delta y_{\mathrm{N_2}}}{y_{\mathrm{N_2}}}\right)^2\right]^{1/2} \tag{C.26}$$

Hydrogen Balance The portion of hydrogen bound in product species i compared to hydrogen available in the input stream is

$$\delta\left(\frac{\dot{N}_{i,}}{\dot{N}_{\mathrm{H_2,reac}}}\right) = \frac{\dot{N}_{i,}}{\dot{N}_{\mathrm{H_2,reac}}}\left[\left(\frac{\delta\varkappa}{\varkappa}\right)^2 + \left(\frac{\delta y_{i,\mathrm{prod}}}{y_{i,\mathrm{prod}}}\right)^2\right]^{1/2} \tag{C.27}$$

The amount of water vapor per hydrogen bound in the fuel is defined by Eq. C.11. The uncertainty is given by

$$\delta\left(\frac{\dot{N}_{\mathrm{H_2O}}}{\dot{N}_{\mathrm{H_2,reac}}}\right) = \left(\frac{\dot{N}_{\mathrm{H_2O}}}{\dot{N}_{\mathrm{H_2,reac}}}\right)\left[\left(\frac{\delta\phi}{\phi}\right)^2 + \left(\delta\left(\frac{\frac{1}{2}\dot{N}_{\mathrm{H_2O}}}{\dot{N}_{\mathrm{O_2,reac}}}\right) \Big/ \left(\frac{\frac{1}{2}\dot{N}_{\mathrm{H_2O}}}{\dot{N}_{\mathrm{O_2,reac}}}\right)\right)^2\right] \tag{C.28}$$

Carbon Balance The uncertainty of the ratio of carbon bound in product species *i* to carbon available in the reactants is

$$\delta\left(\frac{\dot{N}_{i,\mathrm{prod}}}{\dot{N}_{\mathrm{C,reac}}}\right) = \frac{\dot{N}_{i,\mathrm{prod}}}{\dot{N}_{\mathrm{C,reac}}}\left[\left(\frac{\delta\varkappa}{\varkappa}\right)^2 + \left(\frac{\delta y_{i,\mathrm{prod}}}{y_{i,\mathrm{prod}}}\right)^2\right]^{1/2} \tag{C.29}$$

Hydrogen Conversion The hydrogen conversion $\eta_{\mathrm{H_2}}$ is defined in Eq. C.13. The uncertainty follows as

$$\delta\eta_{\mathrm{H_2}} = \eta_{\mathrm{H_2}}\left[\left(\frac{\delta\varkappa}{\varkappa}\right)^2 + \left(\frac{\delta y_{\mathrm{H_2}}}{y_{\mathrm{H_2}}}\right)^2\right]^{1/2} \tag{C.30}$$

which is

Total Energy Conversion Efficiency Staring with the definition of the total energy conversion efficiency in Eq. C.14, its uncertainty can be evaluated as

$$\delta\eta_{\mathrm{Energy}} = \eta_{\mathrm{Energy}}\left[\left(\frac{\delta\varkappa}{\varkappa}\right)^2 + \sum_{\mathrm{prod}}\left(\frac{\delta y_j\ LHV_j}{\sum_{\mathrm{prod}} y_i\ LHV_i}\right)^2\right]^{1/2} \tag{C.31}$$

Hydrogen Energy Conversion Efficiency The uncertainty of the hydrogen energy conversion efficiency follows directly from its definition in Eq. C.14 as

$$\delta\eta_{\mathrm{H_2,Energy}} = \eta_{\mathrm{H_2,Energy}}\left[\left(\frac{\delta\varkappa}{\varkappa}\right)^2 + \left(\frac{\delta y_{\mathrm{H_2}}}{y_{\mathrm{H_2}}}\right)^2\right]^{1/2} \tag{C.32}$$

Appendix D

FLUENT Model

The detailed numerical model uses the computational fluid dynamics (CFD) software FLUENT (Fluent Inc., 2006). At the time of writing, software licenses are available at the Mechanical Engineering Department's High Performance Computing (HPC) lab, which is a cluster of 11 workstations running Linux as the operating system. The workstations can be accessed remotely using a secure shell (SSH) or other suitable software.

Creating and running a FLUENT model involves two steps: first, the geometry has to be specified using the geometric modeling and grid generation tool GAMBIT. Second, the mesh is imported into FLUENT, where models, solvers, boundary- and initial conditions are specified and detailed simulations are run. In addition, FLUENT is capable of integrating user defined functions (UDF), which allow for the implementation of physical processes that are not included in the standard FLUENT code. The instructions below, while not being exhaustive, outline steps necessary for simulations similar to those performed for the numerical results discussed in Chapter 4. Further information on GAMBIT and FLUENT is available in the user manuals (Fluent Inc., 2007; Fluent Inc., 2006).

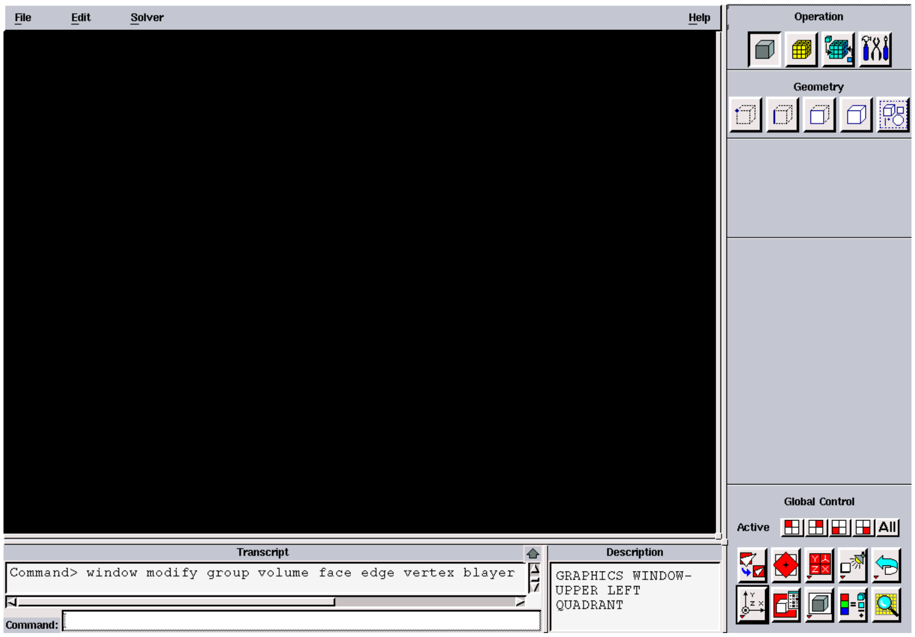

```
Command> window modify group volume face edge vertex blayer
```

GRAPHICS WINDOW-
UPPER LEFT
QUADRANT

Figure D.1: Graphical user interface of Gambit.

D.1 Model Geometry – Gambit

Among other possibilities, the model geometry can be specified using Gambit 2.4, which is the mesh generation software shipped with Fluent. Launching Gambit requires a connection to the HPC lab using a remote shell, e.g. from a local machine running the Linux operating system, a remote connection is established from a terminal using the command `ssh` *`username`*`@hpc`*`XX`*`.me.utexas.edu -Y`, where *`username`* is specific to the user, *`XX`* is the number of the HPC machine (running between *`01`* and *`11`*), and the option `-Y` enables forwarding of graphical user interfaces. Once connected to the HPC lab, a graphical user interface for Gambit is forwarded to the local machine by entering the command `gambit` at the command line (Fig. D.1).

D.1.1 General Procedure

Gambit has four different operation modes, which can be selected using command buttons on the top right of the interface:

- *`Geometry`*: create and modify model geometry
- *`Mesh`*: create and modify meshes
- *`Zones`*: specify boundary and continuum types
- *`Tools`*: create and modify coordinate systems and grids

Each of the command buttons opens a toolpad that allows for different actions in the respective operation mode. In the following paragraphs, the general procedure necessary for the creation of a 2-D model is outlined. More detailed information can be found in Gambit's user manual (Fluent Inc., 2007).

Operation - Geometry. Activate the geometry mode by selecting the *`geometry command button`*. Additional command buttons will appear that allow for the following operations:

- *`Vertex`*: create vertices (points) defining corners
- *`Edge`*: create edges (lines) connecting vertices
- *`Face`*: create faces (areas) defining different parts of the model

When creating vertices, edges and faces, requirements for mesh generation and the specification of boundary and continuum types need to be considered.

Operation - Mesh. Activate the mesh mode by selecting the *`mesh command button`*. Again, additional command buttons allow for the following operations:

- *`Edge`*: create mesh points along edges
- *`Face`*: create mesh across faces

In 2-D, two different approaches for mesh generation exist: non-uniform meshes with trilateral/triangular elements are well suited for complicated geometries, whereas quadrilateral/rectangular elements form a regular mesh, but require some foresight in the specification of vertices, edges and faces of the model.

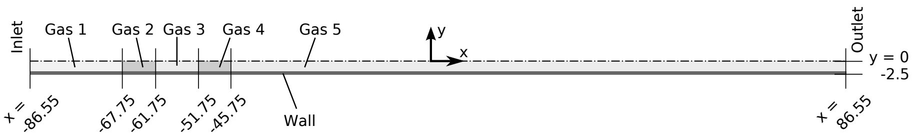

Figure D.2: Model created in GAMBIT.

Operation - Zones. Activate the zone mode by selecting the *zones command button*. Two additional command buttons appear:

- *Boundary Types*: specify boundary types, e.g. *WALL*, *SYMMETRY*, ...
- *Continuum Types*: specify continuum as either *SOLID* or *FLUID*.

Unless names are specified for each zone, GAMBIT/FLUENT will generate names automatically. As additional information has to be specified for each boundary or continuum zone after importing the model to FLUENT, a meaningful naming convention is strongly encouraged. Once the geometric model is defined, it needs to be exported by selecting *File->Export->Mesh* from the menu bar, which generates a mesh file with the extension **.msh*.

D.1.2 Heat Exchanger Geometry

Figure D.2 illustrates the reactor geometry used for detailed numerical simulations. As described in Chapter 4, an infinite array of reactor channels with alternating flow directions can be reduced to a half channel using symmetries inherent to the configuration: due to the symmetry of the flow, only one half of the channel needs to be modeled; and, due to symmetries around the *y*-axis between neighboring channels, the temperature along the centerline of the wall is symmetric.

In general, FLUENT distinguishes between *FLUID* and *SOLID* continuum zones. The half channel illustrated in Figure D.2 contains two porous flow straighteners, which, in FLUENT, are treated as a *FLUID* zone with a porous sub-model. In order to use a structured grid with quadrilateral elements, all edges parallel to *x*-axis and *y*-axis

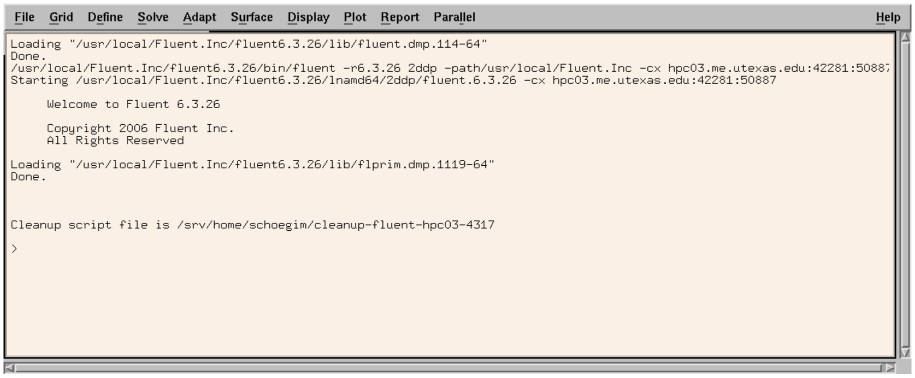

```
Loading "/usr/local/Fluent.Inc/fluent6.3.26/lib/fluent.dmp.114-64"
Done.
/usr/local/Fluent.Inc/fluent6.3.26/bin/fluent -r6.3.26 2ddp -path/usr/local/Fluent.Inc -cx hpc03.me.utexas.edu:42281:50887
Starting /usr/local/Fluent.Inc/fluent6.3.26/lnamd64/2ddp/fluent.6.3.26 -cx hpc03.me.utexas.edu:42281:50887

     Welcome to Fluent 6.3.26

     Copyright 2006 Fluent Inc.
     All Rights Reserved

Loading "/usr/local/Fluent.Inc/fluent6.3.26/lib/flprim.dmp.1119-64"
Done.


Cleanup script file is /srv/home/schoegim/cleanup-fluent-hpc03-4317

>
```

Figure D.3: Graphical user interface of FLUENT.

are partitioned in the same fashion. Using those edges, six faces are created according to five *`FLUID`* zones of the flow channel and a `SOLID` wall zone, where the latter is modeled as a single face.

Grid-points along edges in x-direction are spaced at regular distances within each of the five sections, where the number of elements, from left to right, was chosen as 38, 11, 20, 11 and 300 (Fig. D.2). In the y-direction, the *`SOLID`* wall zone is divided into 3 elements in the vertical direction. *`FLUID`* zones are divided into 12 elements, where the grid spacing is reduced close to y=2 and y=0, which is specified in GAMBIT by a *`“double sided” successive ratio`*, which is chosen as 1.1. Based on the grid-points specified along the edges, regular meshes with quadrilateral elements can be created for all six faces.

All edges around the *`SOLID`* wall zone are specified as `WALL` boundaries. Edges of *`FLUID`* zones at x=±86.55 are inlet and outlet of the channel, which are modeled as *`VELOCITY INLET`* and *`PRESSURE OUTLET`*, respectively. Edges in the x-direction at y=0 are specified as *`SYMMETRY`* boundaries, and remaining edges will default to *`INTERIOR`* boundaries when imported to FLUENT.

D.2 Numerical Simulations – FLUENT

Similar to GAMBIT, the computational fluids dynamic code FLUENT is started via a remote shell by entering `fluent 2ddp` at the command line, which launches the graphical user interface shown in Figure D.3; note that *2ddp* specifies a 2-D solver with double precision. FLUENT stores model information and simulation data in separate files, which use the file extensions *cas* and *dat*, respectively. Once all of the parameters necessary for simulations are specified, FLUENT can be started in batch-mode without the user interface, which is described in Section D.2.6.

D.2.1 General Procedure

Model Geometry. In order to load the model geometry, select *File->Open->Case* from the menu and load the mesh exported from GAMBIT (file extension `*.msh`). Once the mesh is created, select *Grid->Scale* from the menu, specify the units used for the model geometry, and press the *Scale* button to rescale the geometry information to meters, which is the default length unit used by FLUENT.

Energy Equation and Wall Material. In order to model heat transfer, the energy equation needs to be enabled by selecting *Define->Models->Energy*. Now, material properties of the solid can be specified using the materials panel, which is launched via *Define->Materials*. In order to define a new wall material, select *solid* from the *Material Type* drop-down menu, overwrite all fields including name and chemical formula, and press *Change/Create* to add the new material to the model.

Reaction Mechanism and Species Model. The standard FLUENT code supports reaction mechanisms with up to 50 chemical species, which have to be specified using the standard CHEMKIN format. In order to import a reaction mechanism, select *File->Import->CHEMKIN Mechanism*, which opens a panel where file locations for *Gas-Phase CHEMKIN Mechanism*, *Gas-Phase Thermodynamic Database*, and *Transport*

Property Database can be specified. FLUENT interprets the entirety of species used in the reaction mechanism as a mixture, which can be viewed via the materials panel once the mechanism is imported and the species model is initialized.

The species model for transport and chemical reactions is accessed via *Define->Models->Species->Transport&Reaction*. Here, check *Species Transport*, *Volumetric Reactions* and *Stiff Chemistry Solver*. Optionally, parameters for the reaction model can be changed via the submenu *Integration Parameters*.

Boundary Conditions. Boundary conditions are specified via *Define->Boundary Conditions*. Among the list entries, all boundary- and continuum zones that were defined in GAMBIT need to checked, and, if necessary, modified. Note that *symmetry* and *interior* boundaries do not have adjustable parameters, boundary zones ending in *-shadow* inherit properties from the zone with the corresponding name without *-shadow*, and boundaries that were created from multiple edges in GAMBIT are split and consecutively numbered when imported into FLUENT.

Solver, Model Initialization and Simulation. The solver used for numerical simulations is specified via a panel launched by *Define->Models->Solver*. For transient calculations, check *unsteady*. In addition, a *2nd-Order Implicit* formulation can be activated, which, while allowing for larger time-steps, increases the computational effort necessary for each iteration.

Additional solver parameters can be specified using the panel accessed by *Solve->Controls->Solution*, which allows for the adjustment of *Under-Relaxation Factors*, *Pressure-Velocity Coupling*, as well as *Discretization* type, which, while defaulting to *First Order Upwind*, can be changed to alternative spatial discretizations.

Initial values for the model are specified via a panel accessed via *Solve->Initialize->Initialize*, which are applied globally to individual model variables irrespective of the zone. Upon global initialization, zone-specific initial values can be assigned using the `Solve->Initialize->Patch` panel.

Simulations are started via the `Solve->Iterate` panel. For an unsteady simulation with fixed step size, `Time Step Size` and `Number of Time Steps` specify the simulated time interval, whereas `Max Iterations per Time Step` caps the maximum number of iterations of the iterative solution calculated for each time step.

D.2.2 Model-Specific User Defined Functions (UDF's)

User Defined Functions (UDF's) are designed to integrate non-standard processes into FLUENT simulations. UDF's are written in the programming language `C`, and are typically compiled and linked against the FLUENT model. In FLUENT, a series of macros addresses different types of user defined functions, e.g. `DEFINE_SOURCE` to define a source, `DEFINE_PROFILE` to define a profile, and others. Using those macros, model-specific UDF's were programmed to simulate external heat losses, contact resistance for heat transfer, and surface-to-surface radiation; another UDF forces symmetry of the wall center-line temperature around the y-axis. While the function of the individual models is described below, the procedure required for compilation and linking of the UDF's is detailed in Section D.2.7.

External Heat Losses. External heat losses are handled by the UDF function `cell_wall_extheatloss`, which is implemented as a `DEFINE_SOURCE` macro. The heat loss is calculated for each element by the difference between the local temperature and the temperature of the environment as

$$q = -h_\infty (T_s - T_\infty)$$

where values for h_∞ and T_∞ are hard-coded as 11200 W/m^{2}K and 300 K, respectively.

Contact Resistance. The UDF function `face_contactresistance` is defined as a `DEFINE_HEATFLUX` macro to model heat transfer between the wall and an adjacent porous zone. A contact resistance between two solids that are in poor contact determines the heat transfer as

$$q = h_c \Delta T$$

where ΔT is the local temperature difference between a wall element and an adjacent element of a porous zone, and h_c is hard-coded as 1000 W/m^{2}K (Mills, 1999). The `DEFINE_HEATFLUX` macro, however, applies globally to all `SOLID/FLUID` interfaces. Thus, the `face_contactresistance` UDF first determines whether the adjacent fluid zone is porous; if not, the UDF serves an alternative function, where it adds radiative heat fluxes obtained from the surface-to-surface radiation model discussed below.

Surface-to-Surface Radiation Model. While FLUENT has a built-in surface-to-surface radiation model, it does not allow for simulations of enclosures with symmetries. Thus, a surface-to-surface radiation model was implemented externally using UDF macros. In addition, radiation between walls and porous zones was implemented, where values pertaining to the porous zone are approximated by averaged values.

The complexity of the radiation model made the allocation of external memory necessary. Memory allocation, initialization of configuration factors and updates of the radiation model is handled by the `DEFINE_ADJUST` macro `update_radiation`, whereas memory is deallocated by a `DEFINE_EXECUTE_AT_EXIT` macro `clear_radiation`.

The general equations for radiative heat fluxes are given as the balance of incoming and outgoing heat fluxes at gray surfaces k as

$$\begin{aligned} q_k &= q_{o,k} - q_{i,k} \\ q_{o,k} &= \epsilon \sigma T_k^4 + (1-\epsilon) q_{i,k} \\ q_{i,k} &= \sum_j \int q_{o,j} F_{dk-dj} \end{aligned}$$

where ϵ is the emissivity and F_{dk-dj} is the configuration factor between surfaces k and

j (Siegel and Howell, 1992). Combining the above equations yields

$$\frac{q_k}{\epsilon_k} = \sigma T_k^4 - \sum_j \int \left[\sigma T_j^4 - \tfrac{1-\epsilon_j}{\epsilon_j} q_j\right] dF_{dk-dj} \tag{D.1}$$

which can be solved for the radiative heat fluxes q_k given the local surface temperatures T_k. The emissivity of the wall is hard-coded as 0.85.

Heat fluxes calculated for a wall elements are added by modifying the wall heat flux model through the `DEFINE_HEATFLUX` macro `face_contactresistance`. Heat fluxes to the porous zones are handled by the `DEFINE_SOURCE` macro `cell_pm_radflux`.

Symmetric Wall Temperature. In the heat-exchanger model, only the upper half of the wall is modeled (Figure D.2); the boundary at y=–2.5 represents the center-line of the wall. Symmetry of the center-line wall temperature around the y-axis is forced by the `DEFINE_PROFILE` macro `symmetricwalltemp_profile`. Here, the local temperature at the boundary face at position x is specified as the average temperature of `SOLID` wall elements adjacent to boundary faces at positions x and $-x$.

D.2.3 Model Parameters

While Section D.2.1 outlines the general procedure for the specification of model parameters, specific values used for the heat-exchanger model are listed below.

Wall Material. The wall material used for the calculations is Silicon Carbide (SiC). Property values are specified using the materials panel (`Define->Materials`), where heat capacity is set to 670 J/kg-K and the high-temperature conductivity is estimated based on manufacturer specifications as 50 W/m-K. In order to accelerate convergence times, the density is artificially reduced by a factor of 100 to 31 kg/m^3.

Table D.1: Boundary conditions for species concentrations at channel inlet.

	ϕ=1.9	ϕ=2.2	ϕ=2.5
O_2	0.21084	0.20648	0.20332
CH_4	0.09514	0.11387	0.12742
N_2	0.69402	0.67965	0.66926

Reaction Chemistry. The reaction mechanism used for the computations is GRI-Mech 2.11 with 277 elementary chemical reactions and 49 species was chosen (Bowman et al., 1995). In computations, FLUENT does not model the last species in the species list by a conservation equation, but instead calculates it from a balance of mass fractions. Thus, a 50th "virtual" species was added to the species list, which allows for a direct assessment of computational errors, instead of lumping this error into GRI-Mech 2.11's 49th species (Argon).

User-Defined Function Hooks. The radiation model as well as the contact resistance model requires *`User-defined function hooks`*, which can be specified using a panel accessed via *`Define->User-Defined->Function Hooks`*. Here, the *`Adjust`* and *`Execute at Exit`* macros are specified as the two main radiation model macros *`update_radiation`* and *`clear_radiation`*, respectively. Also, the *`Wall Heat Flux`* is set to *`face_contactresistance`*, which handles both contact resistance and radiative heat fluxes at the *`FLUID/SOLID`* boundaries.

D.2.4 Boundary Conditions

Velocity Inlet Boundary. The channel inlet is modeled as a *`velocity-inlet`* boundary zone, which allows for the specification of the flow velocity magnitude normal to the boundary. The velocities used for this work were chosen as either u_{in}=0.75/1.25/1.75 m/s, and the temperature was set at 300 K in all cases. In addition, the gas mixture was specified according to Table D.1 for equivalence ratios ϕ=1.9/2.2/2.5.

Pressure Outlet Boundary. The channel outlet is modeled as a `pressure-outlet` boundary, which, together with a `velocity-inlet`, allows for the adjustment of the total pressure drop along the channel for a specified flow condition. For this boundary type, reversed flows are possible, which are, however, usually only observed during the initial time-steps and disappear once the local pressures adjust according to regular flow conditions. Composition and temperature of back-flows are set equal to initial conditions discussed further below (Section D.2.5), i.e. pure N_2 and T=1442.83 K.

Fluid Continuum Zones. The heat-exchanger model uses five `FLUID` continuum zones, where four zones model the reactor head between x=–86.55 and –45.75, and one zone models the main reactor section between x=–45.75 and 86.55 (Fig. D.2). Two of the four `FLUID` zones in the reactor head are modeled as porous zones, where the porous resistance and inertial resistance are set, in both directions, as 3.846×10^7 and 20.414, respectively. Radiative heat transfer to the porous zones is included by a source term for energy, which is specified as the UDF `cell_pm_radflux`. Reactions are disabled in the reactor head to suppress auto-ignition during the initial transient. Tests for a converged solution at u_{in}=125cm/s and ϕ=2.2 with reactions enabled in all `FLUID` zones did not reveal reactions in the reactor head, which legitimates this assumption.

Wall Continuum Zone. The material of the wall continuum zones is set to silicon carbide. Furthermore, source terms for energy are specified as `cell_wall_extheatloss` in order to include external heat losses.

Wall Boundary. Wall boundary zones depend on the location of the wall. The interior wall at the `SOLID/FLUID` boundary is already handled by the `User-Defined function hook` for `Wall Heat Flux`, and does not require further specification. The `Thermal Condition` of walls at inlet and outlet ($x = \pm86.55$ mm) are specified as `Radiation`, where the external emissivity is set to 0.85 and the external radiation temperature

Table D.2: Thresholds used for grid adaptations.

Grid	method	variable	refine thresh.	coarsen thresh.
Adaptation 1	normalized gradient	C_2H_6	.005	N/A
Adaptation 2	normalized iso-value	CH_2O	0.2	.05
	normalized iso-value	H	0.4	N/A
Adaptation 3	normalized iso-value	CH_2CO	0.2	N/A
	normalized iso-value	OH	0.4	N/A

is 300 K. The *`Thermal Condition`* of the exterior wall at y=–2.5 is specified as *`Temperature`*, which is determined using the UDF *`symmetricwalltemp_profile`*.

D.2.5 Initialization, Simulations and Grid Refinement

Initialization. In all cases, the first part of the model initialization (*`Solve->Initialize->Initialize`*) uses pure nitrogen as the gas and the adiabatic temperature of combustion of methane/air at ϕ=2.2, which is 1442.83 K. The second part of the initialization overwrites some values in order to obtain a more realistic initial condition: *`FLUID`* temperatures are decreased in the reactor head to 600 K in zones 1 and 2, and 900 K in zones 3 and 4 (Fig. D.2). Furthermore, the x-velocities in the *`FLUID`* zones are scaled by the local temperature to match the inlet condition. Similarly, the gas mixture in the reactor head is set to the composition at the inlet, reducing the time between initialization and auto-ignition of the mixture downstream of the reactor head. Note that reactions need to be disabled in the reactor head in order to prevent "homogeneous" auto-ignition.

Time-Stepping. In all cases, a fixed *`time step size`* of 10^{-5} s is used for iterations (*`Solve->Iterate`*). Additionally, the maximum number of iterations per time step is increased to 30. In addition, auto-save is enabled (*`File->Write->Autosave`*) to automatically save intermediate simulation results.

Grid Adaptations. FLUENT allows for a grid adaptations based on thresholds of solution variables (`Adapt->Gradient`). Table D.2 shows the criteria for grid adaptations used in the numerical study, where in `Controls`, only the main `FLUID` zone was enabled for refinement/coarsening, and the maximum refinement level was set to 2.

D.2.6 Running FLUENT Simulations in Batch-Mode

In general, simulations are run from FLUENT's graphical user interface. This, however, requires a connection to the HPC lab, which is impractical for longer computations. FLUENT's text mode, however, allows to run computations without the graphical user interface. In addition, FLUENT can be run in batch mode, where a file containing FLUENT commands is used to control FLUENT simulations.

An example for a batch file (`batch.txt`) is included with the source files. Remote simulations are started from the command line as `nohup nice -n14 fluent 2ddp -g -i batch_file_name > log_file_name &`, where `nohup` is a command preventing the abortion of a job when the remote session is closed, `nice -n14` changes the job priority, and the ampersand `&` returns usability of the command line to the user. Furthermore, the option `-g` starts fluent in text mode, the `-i batch_file_name` forces FLUENT to read commands from a file and `> log_file_name` redirects the output to a log-file.

D.2.7 Installation of Model-Specific UDF's

The UDF's used for the numeric model are defined in the following files, all of which are contained in the zipped directory `udf_sources.tar.gz`:

- `README`: contains installation instructions.
- `udf.c`: main file containing UDF's that can be used in FLUENT (written in C).
- `radiation.h`: header file defining C++ objects that implement the radiation model.

- *`crad.cc/crad.h`*: source code and header file defining wrapper functions for `C++` objects.
- *`xRad.cc`*: test function for radiation model.
- *`Cabinet.h`*: `C++` template class defining persistent storage for arbitrary objects.
- *`DenseMatrix.h`*: `C++` class simplifying the solution of equation systems via LAPACK.
- *`lapack.h`*: header file necessary to link `Fortran` library LAPACK to the radiation model.
- *`xLapack.cc`*: test function for solving equation systems.
- *`Makefile`*: needed for compilation of object file *`crad.o`*, and test functions *`xRad`* and *`xLapack`*.
- *`example.cas.gz`*: example for a FLUENT case file containing model data.
- *`example.dat.gz`*: example for a FLUENT data file containing simulation data.
- *`batch.txt`*: example for a file used for running FLUENT simulations in batch-mode.

The installation instructions are detailed in the file *`README`*.

Bibliography

Ahn, J., C. Eastwood, L. Sitzki, and P. D. Ronney (2005). Gas-phase and catalytic combustion in heat-recirculating burners. *Proc. Combust. Inst.* 30:2463–2472.

Aldushin, A. (1993). New results in the theory of filtration combustion. *Combust. Flame* 94:308–320.

Babkin, V. S. (1993). Filtrational combustion of gases. present state of affairs and prospects. *Pure & Appl. Chem.* 65(2):335–344.

Babkin, V. S., I. Vierzba, and G. A. Karim (2002). Energy-concentration phenomenon in combustion waves. *Combust. Explos. Shock Waves* 38(1):1–8.

Barra, A. J., and J. L. Ellzey (2004). Heat recirculation and heat transfer in porous burners. *Combust. Flame* 137:230–241.

Boomsma, K., D. Poulikakos, and F. Zwick (2003). Metal foams as compact high performance heat exchangers. *Mechanics of Materials* 35:1161–1176.

Bowman, C. T., R. K. Hanson, D. F. Davidson, J. W. C. Gardiner, V. Lissianski, G. P. Smith, D. M. Golden, M. Frenklach, and M. Goldenberg (1995). GRI-Mech 2.11. `http://www.me.berkeley.edu/gri_mech/`.

Bubnovich, V., L. Henriquez, and N. Gnesdilov (2007). Numerical study of the effect of the diameter of alumina balls on flame stabilization in a porous-medium burner. *Numerical Heat Transfer, Part A* 52(3/4):275–295.

Buckmaster, J. (1976). The quenching of deflagration waves. *Combust. Flame* 26:151–162.

Buckmaster, J., P. Clavin, A. Linan, M. Matalon, N. Peters, G. Sivashinsky, and F. A.

Williams (2005). Combustion theory and modelling. *Proc. Combust. Inst.* 30:1–19.

Buckmaster, J., and T. Takeno (1981). Blow-off and flashback of an excess enthalpy flame. *Combust. Sci. Tech.* 25:153.

Bush, W. B., and F. E. Fendell (1970). Asymptotic analysis of laminar flame propagation for general lewis numbers. *Combust. Sci. Tech.* 1:421–428.

Caretto, L. S., A. D. Gosman, S. V. Patankar, and D. Spalding (1972). Two calculation procedures for steady, three-dimensional flows with recirculation. In *Proc. Third. Int. Conf. Num. Mechods Fluid Mech.*, volume 19 of *Lect. Notes Phys.*, pages 60–68. Springer, New York.

Carrette, L., K. A. Friedrich, and U. Stimming (2001). Fuel cells - fundamentals and applications. *Fuel Cells* 1(1):5–39.

Chakraborty, S., A. Mukhopadhyay, and S. Sen (2008). Interaction of lewis number and heat loss effects for a laminar premixed flame propagating in a channel. *Int. J. Thermal Sciences* 47:84–92.

Deshaies, B., and G. Joulin (1980). Asymptotic study of and excess-enthalpy flame. *Combust. Sci. Tech.* 22:281–285.

Dhamrat, R., and J. L. Ellzey (2006). Numerical and experimental study of the conversion of methane to hydrogen in a porous media reactor. *Combust. Flame* 144:698–709.

Dixon, M. J., I. Schoegl, C. B. Hull, and J. L. Ellzey (2008). Experimental and numerical conversion of liquid heptane to syngas through combustion in porous media. *Combust. Flame* 154:217–231.

Drayton, M. K., A. V. Saveliev, L. A. Kennedy, A. A. Fridman, and Y. Li (1998). Syngas production using superadiabatic combustion of ultra-rich methane-air mixtures. *Proc. Combust. Inst.* 27:1361–1367.

Dunn-Rankin, D., P. K. Barr, and R. F. Sawyer (1986). Numerical and experimental study of 'tulip' flame formation in a closed duct. *Proc. Combust. Inst.* 21:1291.

Dunn-Rankin, D., E. M. Leal, and D. C. Walther (2005). Personal power systems.

Prog. Energy Combust. Sci. 31:422–465.

Egerton, A., K. Gugan, and F. J. Weinberg (1963). The mechanism of smouldering in cigarettes. *Combust. Flame* 7:63–78.

Fay, M., R. Dhamrat, and J. L. Ellzey (2005). Effect of porous reactor design on conversion of methane to hydrogen. *Combust. Sci. Tech.* 177(11):2171–2189.

Fernandez-Pello, A. C. (2002). Micro-power generation using combustion: Issues and approaches. *Proc. Combust. Inst.* 29:883–899.

Fluent Inc. (2006). *FLUENT 6.3 User's Guide*. Lebanon NH 03766; USA.

Fluent Inc. (2007). *GAMBIT 2.4 User's Guide*. Lebanon NH 03766; USA.

Fu, X., R. Viskanta, and J. P. Gore (1998). Prediction of effective thermal conductivity of cellular ceramics. *Int. Comm. Heat Mass Transfer* 25(2):151–160.

Fursenko, R. V., and S. S. Minaev (2005). Stability in a system with counterflow heat exchange. *Combust. Explos. Shock Waves* 41:133–139.

Fursenko, R. V., S. S. Minaev, and and V. S. Babkin (2001). Thermal interaction of two flame fronts propagating in channels with opposing gas flows. *Combust. Explos. Shock Waves* 37(5):493–500.

Gavrilyuk, V. V., Y. M. Dmitrienko, S. A. Zhdanok, V. G. Minkina, S. I. Shabunya, N. L. Yadrevskaya, and A. D. Yakimovich (2001). Conversion of methane to hydrogen under superadiabatic filtration combustion. *Theoretical Foundations of Chemical Engineering* 35(6):589–596.

Glassman, I. (1996). *Combustion*. Academic Press, San Diego.

Golombok, M., A. Prothero, L. C. Shirvill, and L. M. Small (1991). Surface combustion in metal fibre burners. *Combust. Sci. Tech.* 77:203–223.

Goodwin, D. G. (2003). An open-source, extensible software suite for cvd process simulation. In *Proc. of CVD XVI and EuroCVD Fourteen*, pages 155–162. Electrochem. Soc.

Gort, R., and J. Brouwers (2001). Theoretical analysis of the propagation of a reaction front in a packed bed. *Combust. Flame* 124:1–13.

Hackert, C. L., J. L. Ellzey, and O. A. Ezekoye (1998). Effects of thermal boundary conditions on flame shape and quenching in ducts. *Combust. Flame* 112:73–84.

Hardesty, D. R., and F. J. Weinberg (1974). Burners producing large excess enthalpies. *Combust. Sci. Tech.* 8:201–214.

Henneke, M. R., and J. L. Ellzey (1999). Modeling of filtration combustion in a packed bed. *Combust. Flame* 117:832–840.

Howell, J. R., M. J. Hall, and J. L. Ellzey (1996). Combustion of hydrocarbon fuels within porous inert media. *Prog. Energy Combust. Sci.* 22:121–145.

Hoyermann, K., F. Mauss, and T. Zeuch (2004). A detailed chemical reaction mechanism for the oxidation of hydrocarbons and its application to the analysis of benzene form in fuel-rich premixed laminar acetylene and propene flames. *Phys. Chem. Chem. Phys* 6:3824–3835.

Hsu, P.-F., W. D. Evans, and J. R. Howell (1993). Experimental and numerical study of premixed combustion within nonhomogeneous porous ceramics. *Combust. Sci. Tech.* 90:149–172.

Iyoha, O., R. Enick, R. Killmeyer, B. Howard, B. Morreale, and M. Ciocco (2007). Wall-catalyzed water-gas shift reaction in multi-tubular Pd and 80wt%Pd-20wt%Cu membrane reactors at 1173 K. *J. Membrane Sci.* 298:14–23.

Jones, A. R., S. A. Lloyd, and F. J. Weinberg (1978). Combustion in heat exchangers. *Proc. R. Soc. Lond. A* 360:97–115.

Joulin, G. (1987). Temperature-lags and radiative transfer in particle-laden gaseous flames - part i: Steady planar fronts. *Combust. Sci. Tech.* 52:377–395.

Joulin, G., and P. Clavin (1979). Linear stability analysis of nonadiabatic flames: Difffusional-thermal model. *Combust. Flame* 35:139–153.

Ju, Y., and C. W. Choi (2003). An analysis of sub-limit flame dynamics using opposite propagating flames in mesoscale channels. *Combust. Flame* 133:483–493.

Ju, Y., and S. Minaev (2002). Dynamics and flammability limit of stretched premixed flames stabilized by a hot wall. *Proc. Combust. Inst.* 29:949–956.

Ju, Y., and B. Xu (2005). Theoretical and experimental studies on mesoscale flame propagation and extinction. *Proc. Combust. Inst.* 30:2445–2453.

Kamphus, M., M. Braun-Unkhoff, and K. Kohse-Höinghaus (2008). Formation of small PAHs in laminar premixed low-pressure propene and cyclopentene flames: Experiment and modeling. *Combust. Flame* 152:28–59.

Karlovitz, B., D. W. Denniston, D. H. Knapschaefer, and F. E. Wellis (1953). Studies on turbulent flames a. flames propagating across velocity gradients; b: Turbulence measurement in flames. *Proc. Combust. Inst.* 4:613–620.

Kee, R. J., J. F. Grcar, M. D. Smooke, and J. A. Miller (1985). A fortran program for modelling steady one-dimensional premixed flames. *Technical Report SAND 85-8240*, Sandia National Laboratories.

Kee, R. J., H. Zhu, and D. G. Goodwin (2005). Solid-oxide fuel cells with hydrocarbon fuels. *Proc. Combust. Inst.* 30:2379–2404.

Kennedy, L. A., J. P. Bingue, A. V. Saveliev, A. A. Fridman, and S. I. Foutko (2000). Chemical structures of methane-air filtration combustion waves for fuel-lean and fuel-rich conditions. *Proc. Combust. Inst.* 28:1431–1438.

Kennedy, L. A., A. V. Saveliev, and A. A. Fridman (1999). Transient filtration combustion. In *Proceedings of the Mediterranean Combustion Symposium*. Instituto di Ricerche sulla Combustione-CNR.

Khanna, V., R. Goel, and J. L. Ellzey (1994). Measurements of emissions and radiation for methane combustion within a porous medium. *Combust. Sci. Tech.* 99:133–142.

Kim, N. I., S. Kato, T. Kataoka, T. Yokomori, S. Maruyama, T. Fujimori, and K. Maruta (2005). Flame stabilization and emission of small swiss-roll combustors as heaters. *Combust. Flame* 141:229–240.

Kim, N. I., and K. Maruta (2006). A numerical study on propagation of premixed flames in small tubes. *Combust. Flame* 146:283–301.

Kotani, Y., and T. Takeno (1982). An experimental study on stability and combustion characteristics of an excess enthalpy flame. *Proc. Combust. Inst.* 19:1503–1509.

Krebs, J. (2003). Hydrogen generation via fuel reforming. In G. R. Myneni, and S. Chattopadhyay (Eds.), *Hydrogen in Materials and Vacuum Systems*. American Institute of Physics.

Laevskii, Y. M., V. S. Babkin, V. I. Drobyshevich, and S. I. Potytnyakov (1984). Theory of filtration combustion of gases. *Fizika Goreniya i Vzryva* 20(6):3–13.

Law, C. K. (2006). *Combustion Physics*. Cambridge University Press, 1st edition.

Lee, S. T., and J. S. T'ien (1982). A numerical analysis of flame flashback in a premixed laminar system. *CombFlame* 48:273–285.

Lee, S. T., and C. H. Tsai (1994). Numerical investigation of steady laminar flame propagation in a circular tube. *Combust. Flame* 99:484–490.

Lin, H., E. V. Wagner, B. D. Freeman, L. G. Toy, and R. P. Gupta (2006). Plasticization-enhanced hydrogen purification using polymeric membranes. *Science* 311:639–642.

Lloyd, S. A., and F. J. Weinberg (1974). A burner for mixtures of very low heat content. *Nature* 251:47–49.

Lloyd, S. A., and F. J. Weinberg (1975). Limits to energy release and utilisation from chemical fuels. *Nature* 257:367–370.

Marbach, T. L., and A. K. Agrawal (2006). Heat-recirculating combustor using porous inert media for mesoscale applications. *Journal of Propulsion and Power* 22(1):145–150.

Maruta, K., T. Kataoka, N. I. Kim, S. Minaev, and R. Fursenko (2005). Characteristics of combustion in a narrow channel with a temperature gradient. *Proc. Combust. Inst.* 30:2429–2436.

Maruta, K., J. K. Parc, K. C. Oh, T. Fujimori, S. S. Minaev, and R. V. Fursenko (2004). Characteristics of microscale combustion in a narrow heated channel. *Combust. Explos. Shock Waves* 40(5):516–523.

Mathis, W. M., and J. L. Ellzey (2003). Flame stabilization, operating range, and emissions for a methane/air porous burner. *Combust. Sci. Tech.* 175(5):825–239.

Matkowsky, B. J., and G. I. Sivashinsky (1979). An asymptotic derivation of two models in flame theory associated with the constant density approximation. *SIAM J. Appl. Math.* 37(3):686–699.

McIntosh, A. C., and A. Prothero (1991). A model of large heat transfer surface combustion with radiant heat emission. *Combust. Flame* 93:111–126.

Michaelis, B., and B. Rogg (2004). FEM-simulation of laminar flame propagation. I: Two-dimensional flames. *J. Comp. Phys* 196:417–447.

Mills, A. F. (1999). *Heat Transfer*. Prentice Hall, 2nd edition.

Min, D. K., and H. D. Shin (1991). Laminar premixed flame stabilized inside a honeycomb ceramic. *Int. J. Heat Mass Transfer* 34(2):341–356.

Minjolle, L. (1981). Method of manufacturing a ceramic unit for indirect heat exchange and a heat exchanger unit obtained thereby.

Mital, R., J. P. Gore, and R. Viskanta (1997). A study of the structure of submerged reaction zone in porous cermic radiant burners. *Combust. Flame* 111:175–184.

Moon, D. J., J. W. Ryu, S. D. Lee, B. G. Lee, and B. S. Ahn (2004). Ni-based catalyst for partial oxidation reforming of iso-octane. *Applied Catalysis A: General* 272:53–60.

Naidja, A., C. Krishna, T. Butcher, and D. Mahajan (2003). Cool flame partial oxidation and its role in combustion and reforming of fuels for fuel cell systems. *Prog. Energy Combust. Sci.* 29:155–191.

Newcomb, S. R. (2009). *SLS Rapid Manufacture and Exhaust Product Characterization of a Novel Superadiabatic Counterflow Heat Exchange Burner*. Master's thesis, The University of Texas at Austin.

Pedersen-Mjaanes, H., L. Chan, and E. Mastorakos (2005). Hydrogen production from rich combustion in porous media. *Int. J. Hydrogen Energy* 30:579–592.

Pizza, G., C. E. Frouzakis, J Mantzaras, A. G. Tomboulides, and K. Boulouchos (2008). Dynamics of premixed hydrogen/air flames in microchannels. *Combust. Flame* 152:433–450.

Richter, H., and J. B. Howard (2002). Formation and consumption of single-ring aromatic hydrocarbons and their precursors in premixed acetylene, ethylene and benzene flames. *Phys. Chem. Chem. Phys* 4:2038–2055.

Ronney, P. D. (2003). Analysis of non-adiabatic heat-recirculating combustors. *Combust. Flame* 135:421–439.

Rotman, D. A., and A. K. Oppenheim (1986). Aerothermodynamic properties of stretched flames in enclosures. *Proc. Combust. Inst.* 21:1303–1312.

Schoegl, I., and J. L. Ellzey (2007a). Superadiabatic combustion in conducting tubes and heat exchangers of finite length. *Combust. Flame* 151:142–159.

Schoegl, I., and J. L. Ellzey (2007b). Ultra-rich combustion in parallel channels to produce syngas from methane. In *Fall Meeting of the Western States Section of The Combustion Institute*.

Schoegl, I., and J. L. Ellzey (2009). A mesoscale fuel reformer to produce syngas in portable power systems. *Proc. Combust. Inst.* 32:3223–3230.

Schoegl, I., S. R. Newcomb, and J. L. Ellzey (2009). Ultra-rich combustion in parallel channels to produce hydrogen-rich syngas from propane. *Int. J. Hydrogen Energy* In press.

Schoegl, I. M., D. Zhou, and J. L. Ellzey (2004). Stabilization of the combustion process in porous burners. In *17th ONR Propulsion Meeting*.

Seshadri, K., X. S. Bai, and H. Pitsch (2001). Asymptotic structure of rich methane-air flames. *Combust. Flame* 127:2265–2277.

Siegel, R., and J. R. Howell (1992). *Thermal Radiation Heat Transfer*. Hemisphere.

Smith, G. P., D. M. Golden, M. Frenklach, N. W. Moriarty, B. Eiteneer, M. Goldenberg, C. T. Bowman, R. K. Hanson, S. Song, J. W. C. Gardiner, V. V. Lissianski, and Z. Qin (1999). GRI-Mech 3.0. http://www.me.berkeley.edu/gri_mech/version30/.

Spalding, D. B. (1957). A theory of inflammability limits and flame-quenching. *Proc. R. Soc. Lond. A* 240(1220):83–100.

Takeno, T., and K. Sato (1979). An excess enthalpy flame theory. *Combust. Sci. Tech.*

20:73–84.

Targett, M. J., W. B. Retallick, and S. W. Churchill (1992). Solutions in closed form for a double-spiral heat exchanger. *Ind. Eng. Chem. Res.* 31:658–669.

Toledo, M., V. Bubnovich, A. Saveliev, and L. Kennedy (2009). Hydrogen production in ultrarich combustion of hydrocarbon fuels in porous media. *Int. J. Hydrogen Energy* 34:1818–1827.

Trimis, D., F. Durst, O. Pickenäcker, and K. Pickenäcker (1997). Porous medium combustor versus combustion systems with free flames. In *Advances in Heat Transfer Enhancement and Energy Conservation*, pages 339–345. South China University of Technology Press.

Vican, J., B. F. Gajdeczko, F. L. Dryer, D. L. Milius, I. A. Aksay, and R. A. Yetter (2002). Development of a microreactor as a thermal source for MEMS power generation. *Proc. Combust. Inst.* 29:909–916.

Viskanta, R., and J. P. Gore (2000). Overview of cellular ceramics based porous radiant burners for supporting combustion. *Environ. Combust. Tech.* 1:167–203.

Vogel, B. J., and J. L. Ellzey (2005). Subadiabatic and superadiabatic performance of a two-section porous burner. *Combust. Sci. Tech.* 177:1323–1338.

Warnatz, J. (1981). The structure of laminar alkane-, alkene-, and acetylene flames. *Proc. Combust. Inst.* 18:369–384.

Weinberg, F. J. (1971). Combustion temperatures: The future? *Nature* 233:239.

Weinberg, F. J., T. G. Bartleet, F. B. Carleton, P. Rimbotti, J. H. Brophy, and R. P. Manning (1988). Partial oxidation of fuel-rich mixtures in a spouted bed combustor. *Combust. Flame* 72:235–239.

Wheeler, A. J., and A. R. Ganji (2004). *Engineering Experimentation*. Pearson Education, New Jersey, 2nd edition.

Wheeler, C., A. Jhalani, E. J. Klein, S. Tummala, and L. D. Schmidt (2004). The water-gas-shift reaction at short contact times. *Journal of Catalysis* 223:191–199.

Wicke, E., and D. Vortmeyer (1959). Zündzonen heterogener Reaktionen in gasdurchströmten Körnerschichten. *Berichte der Bunsengesellschaft für Physikalische Chemie* 63(1):145–152.

Williams, F. A. (1985). *Combustion Theory*. Benjamin/Cummings Pub. Co., 2nd edition.

Yajima, S., T. Satow, and T. Hirai (1965). Mechanism of the pyrolytic graphite formation. *J. Nuclear Mat.* 17:116–126.

Zamashchikov, V. V., and S. S. Minaev (2001). Limits of flame propagation in a narrow channel with gas filtration. *Combust. Explos. Shock Waves* 37(1):21–26.

Zamashchikov, V. V., I. G. Namyatov, V. A. Bunev, and V. S. Babkin (2004). On the nature of superadiabatic temperatures in premixed rich hydrocarbon flames. *Combust. Explos. Shock Waves* 40(1):32–35.

Zhdanok, S., L. Kennedy, and G. Koester (1995). Superadiabatic combustion of methane air mixtures under filtration in a packed bed. *Combust. Flame* 100:221–231.

Vita

Ingmar Schoegl was born in Wels, Austria, where he attended highschool at Bundesrealgymnasium Wels, Dr.-Schauer-Straße. He received a Diplom-Ingenieur in mechatronics from the Johannes-Kepler Universität in Linz, Austria in 2000. Upon graduation, he worked as a development engineer for engine electronics and engine management systems at AVL GmbH in Graz, Austria, focusing on real-time models for control applications. In 2003, he moved to Austin, Texas to pursue a PhD in Mechanical Engineering.

Permanent Address: 4641 Steinhaus 58; AUSTRIA.

This dissertation was typeset with LaTeX 2_{ε}[1] by the author.

---

[1] LaTeX 2_{ε} is an extension of LaTeX. LaTeX is a collection of macros for TeX. TeX is a trademark of the American Mathematical Society. The macros used in formatting this dissertation were written by Dinesh Das, Department of Computer Sciences, The University of Texas at Austin, and extended by Bert Kay, James A. Bednar, and Ayman El-Khashab.